

Karoline Vottestad

Experimental Study of Hydrodynamic Loads on Ventilated Plates Near the Free Surface

Master's thesis in Marine Technology

Supervisor: Trygve Kristiansen

June 2020

Karoline Vottestad

Experimental Study of Hydrodynamic Loads on Ventilated Plates Near the Free Surface

Master's thesis in Marine Technology
Supervisor: Trygve Kristiansen
June 2020

Norwegian University of Science and Technology
Faculty of Engineering
Department of Marine Technology



Abstract

The hydrodynamic loads on simplified structures are studied to investigate how forces vary with porosity and submergence, as well as to provide a comparison of the forces in harmonic oscillations and waves. Forced oscillation and regular wave tests are performed for two ventilated plates (C19 and C28) with porosities 0.189 and 0.280. Experiments are relevant for the stages of offshore installation operations when subsea modules are near the free surface, but fully submerged.

Forced oscillation tests are first considered separately. Added mass coefficients show a decreasing trend towards zero and negative values with decreasing submergence. Damping coefficients follow a steadily increasing trend, with larger values observed for the smallest submergence. Added mass coefficients can be 2-8 times larger for the model with the smallest porosity (C19), while damping is approximately twice as large compared to C28. Larger period dependence is noted for C19 at all submergences. Damping dominance is observed for both models, where this damping dominance increases with porosity.

Separate wave tests show a significant damping dominance for both models. This damping dominance increases with perforation ratio, but the hydrodynamic coefficients are once again largest for C19. Large scatter is observed for the added mass coefficients, where the values become increasingly negative for the smallest submergences. Largest damping is observed for the smallest submergence, and damping values for C19 are approximately 2 times larger than most corresponding values for C28. Once again, larger period dependence is noted for C19 at all submergences. All coefficients also show a strong dependence on the amplitude of motion in both waves and oscillations.

For the separate cases of oscillations and waves, differences in the hydrodynamic loads with perforation are assumed to be caused by larger blockage effects for the model with lowest perforation (C19) and a larger presence of global vortices at the plate ends. The latter is based on findings by Mentzoni [13]. Differences observed with submergence are most likely due to differing interactions with the surrounding fluid and free surface.

Larger forces are observed for forced oscillations compared to waves, where a 25-100% difference is observed for mid to high KC values for both models. At low values of KC, the hydrodynamic loads in waves and oscillations converge towards the same values as $KC \rightarrow 0$. Some deviations are observed for C28, most likely due to unidentified experimental errors. Comparisons with flow visualizations in oscillating and orbital flow conditions by Mentzoni [11] suggest that differences are due to an increased presence of global plate end vortices as the KC number increases. His results show symmetrical patterns of vortices at the plate ends for oscillating flow, but only a single one-sided vortex in orbital conditions for high KC numbers. These plate end vortices are not observed for the lowest KC range, which could explain similar forces for waves and oscillations at low KC numbers.

Sammendrag

De hydrodynamiske kreftene på forenklede strukturer blir studert for å undersøke hvordan krefter varierer med porøsitet og nedsenking, samt gi en sammenligning mellom harmoniske oscillasjoner og bølger. Tvungne oscillasjoner og bølgeforsøk utføres for to ventilerte plater (C19 og C28) med porøsitet 0.189 og 0.280. Eksperimenter er relevante for stadiene i offshore installasjonsoperasjoner der undervannsmoduler er nær overflaten, men fullt nedsenket.

Tvungne oscillasjoner vurderes først separat. Tilleggsmassekoeffisienter viser en avtagende trend mot null og negative verdier for minskende nedsenking. Dempingskoeffisienter følger en økende trend, der største verdier observeres for laveste dypgang. Tilleggsmassekoeffisienter kan være 2-8 ganger større for modellen med minst porøsitet (C19), mens dempingen er omtrent dobbelt så stor sammenlignet med C28. Større periodeavhengighet observeres for C19 ved alle dypganger. Dempingsdominans observeres for begge modeller og øker med porøsitet.

Separate bølgetester viser en betydelig dempingsdominans for begge modeller. Dempingsdominansen øker med perforering, men de hydrodynamiske koeffisientene er nok en gang størst for C19. Det blir observert stor spredning i tilleggsmassekoeffisientene, der verdiene blir mer negativ for de minste dypgangene. Størst demping observeres for lavest dypgang og dempingsverdiene for C19 er omtrent 2 ganger større enn tilsvarende verdier for C28. Nok en gang er periodeavhengigheten størst for C19 ved alle dypganger. Alle de hydrodynamiske koeffisientene viser en sterk amplitudeavhengighet i både bølger og tvungne oscillasjoner.

Det antas at forskjeller i de hydrodynamiske kreftene med perforering for de separate tilfellene av bølger og tvungne oscillasjoner skyldes større blokkeringseffekter for modellen med lavest porøsitet (C19), samt en større tilstedeværelse av globale virvler ved plateendene. Det siste er basert på funn av Mentzoni [13]. Forskjeller med dypgang skyldes sannsynligvis forskjellige interaksjoner med omkringliggende væske og den frie overflaten.

Kreftene er større for tvungne oscillasjoner sammenlignet med bølger, der en 25-100% forskjell blir observert for middels til høye KC-verdier for begge modeller. Ved lave KC-tall konvergerer kreftene i bølger og oscillasjoner mot de samme verdiene når $KC \rightarrow 0$. Noen avvik observeres for C28, mest sannsynlig på grunn av uidentifiserte eksperimentelle feil. Sammenligninger med strømningsvisualiseringer i oscillerende og orbitale strømningsforhold av Mentzoni [11] antyder at forskjeller skyldes en økt tilstedeværelse av globale endevirvler når KC-tallet øker. Mentzoni sine resultater viser symmetriske mønstre av virvler i plateendene for oscillerende strømning, men bare en ensidig endevirvel under orbitale forhold for høye KC-tall. Disse plateendevorteksene er ikke observert for lave KC-tall, noe som kan forklare lignende krefter for bølger og oscillasjoner ved lave KC-verdier.

Acknowledgments

The result of this thesis is the sum of many parts, and I would like to express my gratitude towards the many people who have made this possible.

First and foremost, I would like to thank my talented supervisor Prof. Trygve Kristiansen for the opportunity to work on this exciting topic. Your enthusiasm for the field of Hydrodynamics has been a substantial motivation for further learning, and your continuous guidance has paved the way for the completion of this thesis. Thank you for always meeting me with understanding and kindness, and for taking time to help me expand my knowledge on this topic. I would also like to thank Fredrik Mentzoni for taking time out of his busy schedule to share his own knowledge and results on the topic, and Prateek Gupta for his good advice on laboratory work and post-processing of experimental results. I also express my gratitude to Frøydis Solaas and Mia Abrahamsen-Prsic for help with evaluating and validating my experimental results, and for their interest in this thesis.

I would also like to thank the wonderful lab technicians at NTNU, in particular Torgeir Wahl, for their help in the laboratory. They have been essential for the completion and success of my experiments in Ladertanken, and their guidance and expertise has been much appreciated. I must extend this thank you to my fellow students and new-found friends Jon Kristian Voster and Marius Robsahm who have always been available to help with model installations and guidance in Matlab, and who have made this process so collaborative and enjoyable.

Now that five years in Trondheim have come to an end, I would like to express my sincerest gratitude towards my family, friends, and classmates for their help and guidance along the way. Although our time at Tyholt came to an abrupt end and the world we live in now seems somewhat chaotic, I am thankful for the wonderful years we have had together and look forward to new adventures in the future. I wish you all the best!

Karoline Vottestad

Contents

Abstract	i
Sammendrag	ii
Acknowledgments	iii
Nomenclature	vii
1 Introduction	1
1.1 Motivation	1
1.2 Objective & Thesis Structure	2
1.3 Flow Separation and Vortex Shedding on Solid Plates in Oscillatory Flow	3
1.4 Hydrodynamic Forces on Ventilated Structures	4
1.4.1 Previous Studies	4
1.4.2 Recent Studies	6
1.5 DNV-GL's Recommended Practice	7
2 Theory	9
2.1 Linear Wave Theory	9
2.2 Hydrodynamic Force	11
2.3 Linear and Quadratic Damping	12
2.4 Morison's Equation and Hydrodynamic Coefficients	13
2.5 Wave Excitation Forces	14
2.6 Parameter Dependence	15
2.6.1 Oscillating Flow	15
2.6.2 Ventilated Structures	17
2.6.3 Free Surface Oscillations	17
3 Experimental Set Up & Procedure	18
3.1 Test Environment and Rig	18
3.2 Test Models	19
3.3 Test Matrices	20
3.3.1 Model Configurations	20
3.3.2 Forced Oscillation Matrix	21
3.3.3 Wave Matrix	21
3.4 Instrumentation	22
3.4.1 Measurement System	22
3.4.2 Sampling Frequencies	22
3.4.3 Sensors	23

3.4.4	Calibration of Sensors	24
3.4.5	Calibration of Wave Generator	25
4	Procedure for Post-Processing of Experimental Data	26
4.1	Forced Oscillations	26
4.2	Tests in Waves	29
5	Results & Discussion	33
5.1	Forced Oscillations	33
5.1.1	Force Times Series	33
5.1.2	Deep Water Oscillations vs. Semi-Analytical Method by Fredrik Mentzoni	36
5.1.3	Effect of Submergence on Hydrodynamic Coefficients	38
5.1.4	Effect of Porosity on Hydrodynamic Coefficients	43
5.2	Wave Tests	47
5.2.1	Force Time Series	47
5.2.2	Effect of Submergence and Porosity on Hydrodynamic Coefficients	49
5.2.3	Normalized Force and Comparison with Wave Tests by Fredrik Mentzoni	55
5.3	Comparison of Forced Oscillations and Waves	57
5.3.1	Added Mass and Damping Coefficients	57
5.3.2	Normalized Force and the Importance of Flow Separation	60
5.3.3	Comparison of Drag Coefficients	65
5.4	Discussion on Experimental Errors	67
6	Conclusion	69
	References	72
	Appendices	73
A	Comparison of Forced Oscillations and Waves	73
A.1	Added Mass Coefficients for C19	73
A.2	Added Mass Coefficients for C28	75
A.3	Damping Coefficients for C19	77
A.4	Damping Coefficients for C28	79
A.5	Drag Coefficients for C19	81
A.6	Drag Coefficients for C28	82
A.7	Normalized Force for C19	83
A.8	Normalized Force for C28	84
B	Forced Oscillation Tests	86
B.1	Force Time Series for C19	86
B.2	Force Time Series for C28	94
C	Wave Tests	102
C.1	Force Time Series for C19	102
C.2	Force Time Series for C28	106

Nomenclature

α	Coefficient for drag term by Graham
β	Reynolds number divided by the KC number
$\ddot{\eta}_3$	Vertical acceleration
$\dot{\eta}_3$	Vertical velocity
ϵ	Wave phase
η_3	Vertical motion
$\frac{A}{A_0}$	Non-dimensional added mass coefficient
$\frac{B}{\omega A_0}$	Non-dimensional damping coefficient
λ	Wavelength
μ	Discharge coefficient
ν	Kinematic viscosity
ω	Oscillation/wave frequency
ϕ	Velocity potential
ρ	Fluid density
ζ	Wave elevation
ζ_a	Wave amplitude
A, A_{33}	Dimensional added mass coefficient
A_0	Added mass of solid plate
a_x, a_z	Horizontal and vertical acceleration
B, B_{33}	Dimensional damping coefficient
C_D	Drag coefficient
C_M	Inertia coefficient
C_{33}	Restoring coefficient
D	Diameter
F	Force
g	Gravitational constant ($9.81ms^{-2}$)

h	Water depth
k	Wave number
KC	Keulegan-Carpenter number
KC_{por}	Porous Keulegan-Carpenter number
L	Length
p	Pressure
r	Perforation ratio
Re	Reynolds number
T	Oscillation/wave period
t	Time
u,w	Horizontal and vertical velocity components
V	Volume
x,y,z	Cartesian coordinates
BEM	Boundary Element Method
CFD	Computational Fluid Dynamics
FFT	Fast Fourier Transformation
MOVE	Marine Operations in Virtual Environments
WP	Wave Probe

Chapter 1

Introduction

1.1 Motivation

Extensive subsea fields are present in shallow and deep waters along the Norwegian coast, efficiently delivering oil and gas to onshore facilities, FPSO's and offshore platforms. These fields consist of large and complex structures like manifolds and christmas trees, which relay product towards the surface through pipelines and risers. The development of subsea fields involve the installation of new modules and the expansion of existing fields, as well as continuous maintenance of structures and equipment.

Porous and ventilated plates are commonly used in marine and subsea applications. Examples of these include heave plates, mudmats and hatch covers, which serve as protection for equipment on the seabed from overtrawling and falling objects. These ventilated structures can be installed separately, but are often part of complex subsea modules consisting of various pipes, valves and control systems. Experiments by Mentzoni, 2018 [12] show that the hydrodynamic forces on ventilated plates are likely to dominate the total loads on subsea modules. These are structures with a large vertical projected area, giving rise to significant vertical forces in the wave zone and a low limiting sea state for installation. Due to the uncertainties in predicting these hydrodynamic loads, subsea structures are often over-designed, resulting in higher costs and a waste of resources.

Marine operations for lifting and lowering structures towards the seabed are central for the development of subsea fields. The installation of these structures is dependent on the capacity of the vessel crane. For large and complex fields, protection templates and the equipment inside it are typically installed separately. For smaller fields, these subsea modules can be lowered towards the seabed in a single lift. Moonpool operations are also common, though mostly used for the installation of pipes and umbilicals. The central hydrodynamic loads that are important during installation are dependent on the complexity of the environment, which is defined by the different stages of the subsea lift operation. These stages are summarized below [11]:

- The structure is lifted off deck and lowered towards the sea surface.
- Initial water entry occurs, where the structure moves in and out of water.
- The structure is lowered to a point where it is fully submerged, but still in close proximity to the free surface.
- The structure is lowered in infinite fluid, i.e. far from the free surface and seabed.

- The structure is positioned on to the seabed.

The hydrodynamic loads and data associated with the last four stages of subsea installations are slamming and water entry forces, the splash zone wave forces, and added mass and damping (drag) coefficients in infinite fluid or near the free surface and seabed [1]. Increased knowledge is needed regarding these hydrodynamic loads, especially for complex porous and ventilated structures where interaction and shielding effects between different members are present. According to DNV-GL [5], these interaction effects must not be neglected for structures with a porosity of less than 50%, as they can lead to a significant increase or decrease in forces on the structure.

Offshore lifting operations are restricted based on environmental conditions, and the offshore industry is experiencing an increased demand for operability on an all-year basis without risk of lengthy delays to the overall operation. Operational limits are typically defined by the significant wave height, where current practice requires extremely calm sea states for installation to commence. Wind speed and current are also closely monitored prior to installation. In recent years there has been a collective wish to challenge conservative operational limits, with industrial giants like Equinor aiming to perform operations in sea states with a significant wave height of $4.5m$ and higher. This need for all-year-round operations in harsher weather conditions makes it increasingly important for accurate estimates of the hydrodynamic loads acting on structures during deployment. The consequences of not understanding these loads are larger crane and vessel capabilities than necessary, costly delays due to waiting on weather, and unsafe operations that put equipment and personnel at risk.

1.2 Objective & Thesis Structure

Based on the above motivations, the main goal of this thesis is to provide an increased understanding of the hydrodynamic loads on simplified ventilated plates in waves. Main focus will be on the third stage of a subsea lift operation, where structures are fully submerged and in close proximity to the free surface. Experimental trials involving forced harmonic oscillations and regular wave tests are conducted to observe how the hydrodynamic loads and coefficients are influenced by porosity and submergence. The latter is especially relevant for the offshore installation of subsea modules, where approximate estimates from deep water oscillation tests are often used to determine the hydrodynamic loads on the structures. Experiments also aim at describing how these hydrodynamic loads vary in forced oscillations and waves. A handful of projects at NTNU have studied various configurations of simplified structures in both infinite fluid and the wave zone. The recent Doctoral Thesis by Fredrik Mentzoni [11] investigates hydrodynamic loads on perforated plates through experimental and numerical studies. Researchers Frøydis Solaas and Mia Abrahamsen-Prsic have also performed forced oscillation trials and wave tests on a number of models with varying porosity and geometry, and their work is currently ongoing. Based on previous studies and current guidelines, this thesis fills a gap when it comes to how the hydrodynamic loads behave when varying the submergence close to the free surface.

This thesis aims to contribute to one of the projects of MOVE (Marine Operations in Virtual Environments), which focuses on the loads of subsea structures during lifting operations. Fellow students Marius Robsahm and Jon Kristian Voster are also contributing to the MOVE project by studying the loads on ventilated plates through experimental trials and CFD. While Jon Kristian has studied regular and irregular forced oscillatory motion in infinite fluid, Marius has investigated hydrodynamic interactions between porous plates

and cylinders directly in the splash zone. The differences between these three projects are simply illustrated in Figure 1.1.

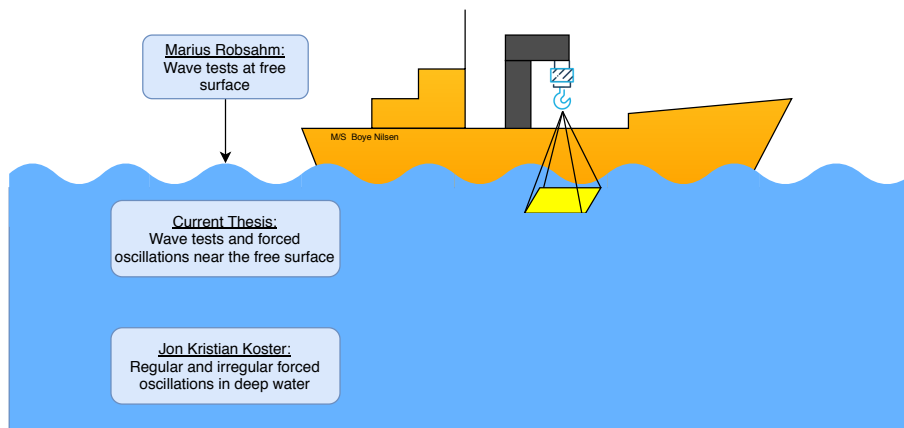


Figure 1.1: Simplified thesis objective and comparison of current projects.

This thesis is divided into six main chapters. The first covers the motivation behind this master thesis. It also gives insight into previous and recent studies regarding the importance of flow separation on solid and porous plates in oscillating flow, and findings on the behavior of hydrodynamic forces and coefficients in oscillating flow and waves. Chapter 2 presents the required theory for post-processing of experimental results. Chapters 3 and 4 give in-detail descriptions of the experimental set up and post-processing procedure. Results are presented and discussed in Chapter 5, and the final chapter presents the main conclusions and suggestions for further work.

1.3 Flow Separation and Vortex Shedding on Solid Plates in Oscillatory Flow

For the study of wave induced forces on static or moving structures, as well as the behavior of bodies vibrating in an otherwise still fluid, it is important to understand how the flow past a body in an oscillatory flow field influences the total hydrodynamic loads. Two-dimensional oscillatory flows have been widely studied through experimental work, showing how the flow regimes vary for different ranges of the Keulegan-Carpenter number (presented in Section 2.6). For the case of flat plates in an oscillatory flow field, it is especially important to understand how the plate-end vortices contribute to the overall forces on the body.

Graham, 1980 [7] studied the forces induced by flow separation and vortex shedding on sharp-edged cylinders in oscillatory flow at low Keulegan-Carpenter numbers. In his study, he argued that the equation suggested by Morison, Johnson & Schaaf, 1950 [17] (also known as Morison's equation, which will later be presented in Section 2.4) with suitable values of added mass (C_M) and drag (C_D) coefficients gives fairly accurate predictions of the forces in the high KC -regime. Predictions for flat plates and other sharp-edged bodies are, however, less accurate for low values of KC .

Through his analysis, Graham concluded that the additional force induced on the body due to the presence of plate-end vortices is proportional to $KC^{\frac{2}{3}}$ for a flat plate, and

that the drag term (C_D) in Morison's equation should vary as $KC^{-\frac{1}{3}}$. As a result, Graham derived the following analytical expressions for the added mass, damping, and drag coefficients for a solid plate:

$$C_A = a_0 + a_1 KC^{\frac{2}{3}} \quad (1.1)$$

$$C_B = \frac{b_1}{\pi^2} KC^{\frac{2}{3}} \quad (1.2)$$

$$C_D = \alpha \cdot KC^{-\frac{1}{3}} \quad (1.3)$$

where a_0 , a_1 , and b_1 are non-dimensional coefficients that can be found through curve-fitting of experimental or numerical results. The coefficient α was given a theoretical value of 8.0 as a result of calculations by Graham. He also suggested a value of 11.2 based on experimental results for bodies in oscillatory flow by Singh, 1979 [20].

1.4 Hydrodynamic Forces on Ventilated Structures

1.4.1 Previous Studies

Molin, 2001 [15] worked several years towards developing a theoretical hydrodynamic model of perforated and slotted structures. He started with a hydrodynamic analysis of the stabilizer of the Roseau compliant tower, as well as a ventilated protection cover for subsea modules. Forced motion tests of both models showed a high amplitude dependence for the added mass, as well as an accompanied strong damping. Molin, 2011 [16] then suggested a semi-analytical method for calculating the added mass and damping of periodic arrays of porous disks. This method was based on potential flow theory, and included the effect a pressure drop across the disk that is quadratic with respect to the normal velocity.

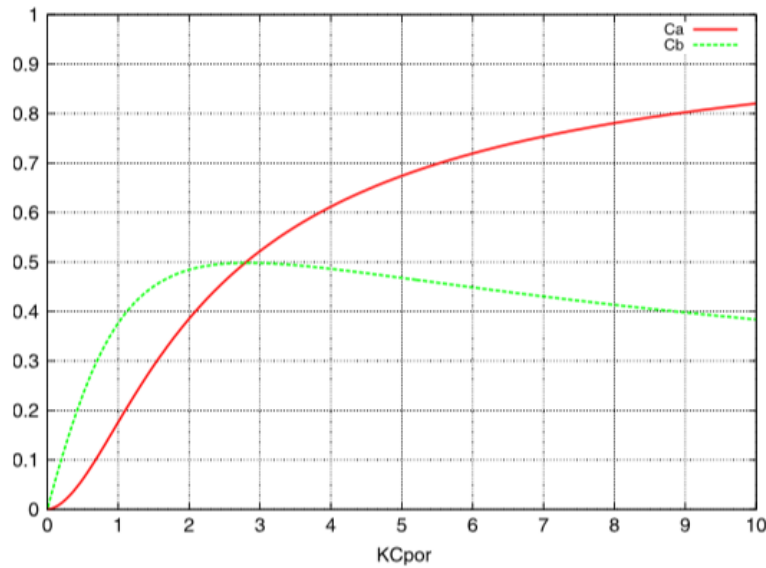


Figure 1.2: Added mass and damping coefficients for a two-dimensional porous plate in infinite fluid. Source: [16].

Results from Molin’s numerical method for a porous plate in infinite fluid are depicted in Figure 1.2. It must be noted that this method does not include the effects of flow separation at the plate edges. Molin found that the method which neglected plate end vortices gave an increase in added mass (C_A) for all values of KC . As the figure shows, the added mass component shows a steadily increasing trend for increased amplitudes of motion. The damping force component (C_B) showed a steady increase for small KC numbers, with a maximum value of 0.5 at $KC \approx 2.5$. Below this value, the damping force was dominant to the added mass force. A steady decrease was observed for increasing KC numbers.

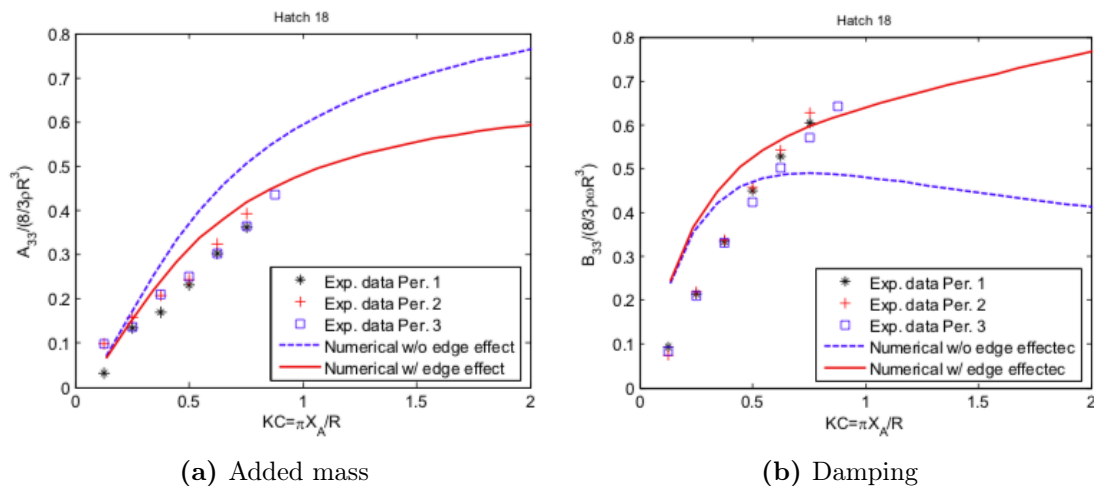


Figure 1.3: Experimental and numerical added mass and damping vs. KC for a hatch cover. Source: [18].

Sandvik, Solaas & Nielsen, 2006 [18] compared experimentally determined added mass and damping coefficients for a simplified hatch cover to numerical results from the method suggested by Molin, 2011 [16]. In addition, numerical results including effects due to vortex shedding along the plate edges were considered. The force due to edge effects was estimated using the drag coefficient suggested by Graham, 1980 [7] in Equation 1.3. A reduced value equal to $1/4^{th}$ of the suggested value ($C_D = 2KC^{-1/3}$) was implemented to account for the rounding of the edges. As is shown in Figure 1.3, including the edge effects in the numerical method reduced the added mass and increased the damping. Similar results were presented by Song An, 2014 [1]. Numerical results with and without the additional drag term to account for flow separation at the plate ends showed that the contribution to the damping from the outer edges was almost three times higher for the largest KC value.

The experiments by Sandvik et al. [18] involved force oscillation tests for three different roof designs for protection structures and two simplified hatch cover models. The perforation ratio (r), defined as the area of ventilation opening divided by the total area, varied from 0.15 to 0.47 for the different models. Results showed a strong amplitude dependence for the hydrodynamic coefficients, and a damping dominance for most KC values. An [1] also compared forced oscillation tests at 10cm and 70cm submergence for plates with porosities of 7.945% and 15.89%. Results showed larger damping at smaller submergence for a given value of KC due to free-surface wave generation, and smaller added mass for 10cm submergence.

1.4.2 Recent Studies

Mentzoni, 2018 [12] performed forced oscillation tests using a porous plate and five-cylinder grill model with perforation ratios $r = 0.278$ and $r = 0.286$. He observed a clear damping dominance, where the damping force could be responsible for 93% of the total hydrodynamic force. By comparing results with previous studies by Song An and Faltinsen, 2013 [2], he was also able to show that this damping dominance increased with increasing porosity. Forced oscillation and wave tests by Gupta, 2018 [8] for two porous plates and a grill model with porosities of $r = 0.19$ and $r = 0.28$ also showed a significant damping dominance, where the damping contribution could be as high as 1.5 to 3.0 times the added mass for a porous structure in the case of forced oscillations, and 10 to 100 times larger when subjected to incident waves.

Mentzoni, 2019 [13] also performed a 2D numerical analysis on the hydrodynamic forces on perforated plates with ten different perforation ratios ($\tau = 0.05 - 0.5$) in oscillating flow. He observed that the hydrodynamic coefficients in general decrease with increasing perforation ratio, and increase with increasing KC numbers for a given value of r . This in turn means that the coefficients are dependent on the amplitude of motion for all perforation values. These observations are also reflected in the earlier studies by Sandvik et al. [18] and An & Faltinsen [2]. In this study, Mentzoni also proposed a semi-analytical model for estimating the non-dimensional added mass and damping coefficients for perforated plates based on the solid plate model by Graham, 1980 [7]. This model is based on Equations 1.1 and 1.2, with parameters found through the curve-fitting of CFD results for *sharp-edged* plates. Some relevant coefficients are presented in Table 1.1.

Table 1.1: Coefficients for semi-analytical method by Mentzoni, 2019 [13].

Perforation Ratio (r)	a_0	a_1	b_1
0.20	0.132	0.261	7.67
0.30	0.017	0.181	5.48
0.50	0.000	0.057	2.04

To compare the hydrodynamic forces on ventilated plates in varying flow conditions, Mentzoni, 2020 [14, 11] compared CFD results for a sharp-edged cylindrical grill model with porosity $r = 0.28$ in oscillating and orbital flows. The latter is similar to the conditions of oscillating flow, but with non-zero horizontal velocities and accelerations. Mentzoni observed significant differences in the hydrodynamic forces between oscillating and orbital flow conditions, which became more prominent for high values of KC. At low KC numbers, the hydrodynamic forces were quite similar for both conditions. The results are shown in Figure 1.4, where the normalized force amplitude is plotted against the KC number. Using streamline plots to study the flow in detail, he concluded that these force variations were a consequence of differences in vortex generation at the plate ends. Mentzoni's findings on plate end separation will be discussed in greater detail in Section 5.3, which focuses on the differences between the experimentally determined hydrodynamic loads in forced oscillations and waves. Gupta, 2018 [8] also showed that hydrodynamic coefficients for wave tests were much smaller than the corresponding values from forced deep water installations. Added mass was approximately $1/10^{th}$ of the corresponding value, while damping (drag) was about half the value.

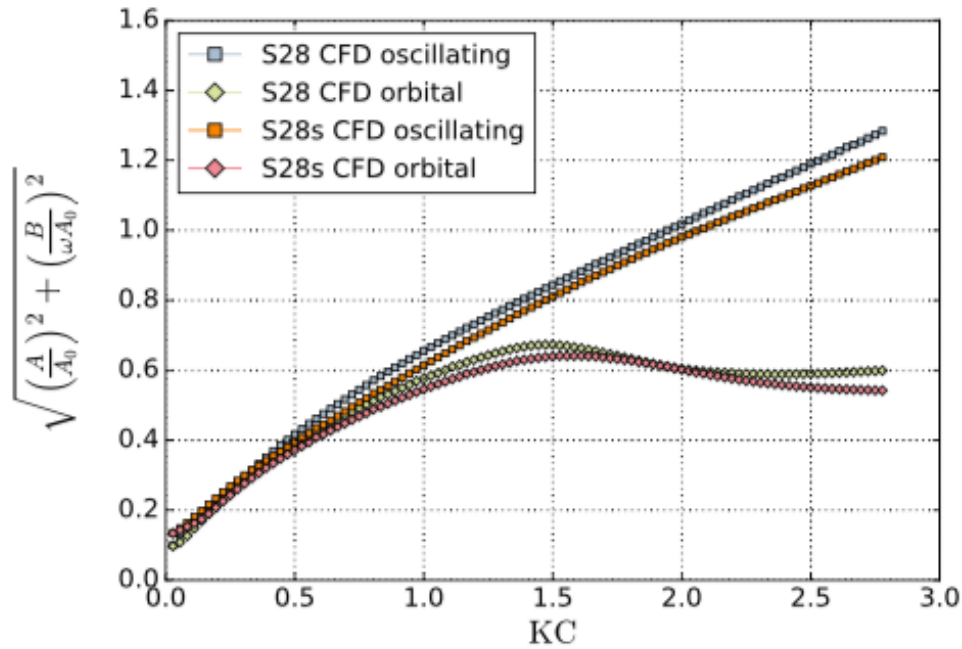


Figure 1.4: Normalized force amplitude vs. KC for numerical simulations of oscillating flow conditions and orbital flow conditions. Source: [14].

1.5 DNV-GL's Recommended Practice

Different methods are used to estimate the hydrodynamic coefficients for a structure. Typical practice involves discretizing complex structures into simple geometries, and calculating the coefficients using analytical, numerical or experimental methods. Blevins, 1984 [3] calculated, for example, the drag forces on screens, grillages and perforated plates in terms of the total static pressure drop across the plate. Many of these coefficients, as well as added mass coefficients for simplified bodies, are listed by DNV-GL, 2017 [5] in their recommended practice.

In the case of added mass for porous structures, DNV-GL refers to results by Sandvik et al., 2006 [18]. A method for calculating the asymptotic value of zero amplitude ($KC = 0$) added mass is also presented, which can be found from potential theory and calculated by a sink-source panel program. The following approximated formula is given:

$$\frac{A}{A_0} = e^{-r/0.28} \quad (1.4)$$

where A is the zero amplitude limit added mass, A_0 is the added mass for an equivalent solid plate, and r is the perforation ratio. This equation is dependent on the perforation ratio only, and suggests that ventilated structures have considerable added mass for low values of KC . The recommended practice states that this asymptotic value may give inaccurate values for structures in oscillatory fluid flow.

DNV-GL also presents a similar relation for the added mass of a ventilated structure at any KC number, which is based on limited model test data and therefore includes a safety margin:

$$\frac{A}{A_0} = \begin{cases} 1 & \text{if } r \leq 0.05 \\ 0.7 + 0.3 \cos\left(\pi\left(\frac{r-0.05}{0.34}\right)\right) & \text{if } 0.05 < r < 0.34 \\ \exp\left(\frac{0.1-r}{0.28}\right) & \text{if } 0.34 \leq r \leq 0.50 \end{cases} \quad (1.5)$$

The expressions in Equation 1.5 are yet again only functions of the perforation ratio, and are meant to be conservative estimates. The actual value for the added mass may vary depending on geometry and amplitude, as previous studies in Section 1.4 have shown that the hydrodynamic coefficients for ventilated plates are highly amplitude dependent. For better accuracy, DNV-GL recommends CFD studies or model tests. Previous studies have also shown that damping contributions generally dominate the total hydrodynamic force on ventilated structures, yet DNV-GL presents no method for estimating damping coefficients based on the perforation ratio.

The recommended practice by DNV-GL also emphasizes the fact that scaling effects may be important for perforated structures. Test models used for estimating force coefficients for full scale modules are scaled by use of the Froude number. When viscous forces are prominent, the Reynolds number is also relevant due to vortex shedding. Corrections to the Froude scaling may therefore be necessary.

Chapter 2

Theory

This chapter presents the relevant theory needed for post-processing of experimental data, and in combination with relevant literature presented in the previous chapter builds a basis for the results presented in Chapter 4. The aim is to give an understanding of the hydrodynamic loads on structures in an oscillating flow field, as well as the parameters that influence the resulting hydrodynamic coefficients. Wave excitation forces and Morison's equation are discussed, and a brief introduction to linear wave theory is also presented.

2.1 Linear Wave Theory

Potential flow theory is derived from the assumption that the fluid is inviscid and incompressible, and that the flow itself is irrotational. This allows for the introduction of a so-called velocity potential (ϕ), which can be found through linearization of the boundary value problem. The velocity potential for a regular wave propagating in the positive x-direction can be expressed as [6]:

$$\phi(x, z, t) = \frac{g\zeta_a}{\omega} \frac{\cosh k(z+h)}{\cosh kh} \cos(\omega t - kx) \quad (2.1)$$

where g is the gravitational constant, ζ_a is the linear wave amplitude, $\omega = \frac{2\pi}{T}$ is the wave frequency, $k = \frac{2\pi}{\lambda}$ is the wave number, (x, z, t) are time and position coordinates, and h is the water depth. The equation for the velocity potential, as well as the following relations, are valid for finite water depth. If infinite water depth is assumed, the limit $h \rightarrow \infty$ must be applied.

The dispersion relation provides the relationship between the wavelength (λ) and the wave period (T), which are related to the wave frequency and wave number. For finite water depth, the dispersion relationship can be expressed as:

$$\omega^2 = gk \tanh kh \quad (2.2)$$

The surface elevation for a sinusoidal wave propagating in the positive x-direction is defined by the following relation:

$$\zeta(x, t) = \zeta_a \sin(\omega t - kx + \epsilon) \quad (2.3)$$

where ϵ is the phase of the wave. For future analysis, this wave phase plays a crucial role in the validity of the results and must be incorporated in the calculation of wave particle velocity and acceleration.

The velocity of the wave particles in the x- and z-directions are calculated by differentiating the velocity potential in Equation 2.1 with respect to x and z respectively. They are defined as:

$$u(x, z, t) = \omega \zeta_a \frac{\cosh k(z+h)}{\sinh kh} \sin(\omega t - kx) \quad (2.4)$$

$$w(x, z, t) = \omega \zeta_a \frac{\sinh k(z+h)}{\sinh kh} \cos(\omega t - kx) \quad (2.5)$$

The corresponding horizontal and vertical accelerations are found by differentiating the velocities u and w with respect to time:

$$a_x(x, z, t) = \omega^2 \zeta_a \frac{\cosh k(z+h)}{\sinh kh} \sin(\omega t - kx) \quad (2.6)$$

$$a_z(x, z, t) = -\omega^2 \zeta_a \frac{\sinh k(z+h)}{\sinh kh} \cos(\omega t - kx) \quad (2.7)$$

According to linear theory, the velocity potential and fluid velocity are assumed constant from the mean free surface to the free surface level [6]. This also affects the wave particle acceleration distribution in a wave crest. Figure 2.1 shows the horizontal velocity distribution for the flow under a wave crest, which is consistent with linear theory. In realistic conditions, this distribution will not be valid. Figure 2.2 illustrates how fluid particle velocities and accelerations in the x- and z-directions vary throughout the crest and trough of a sinusoidal wave propagating positively along x . Under a wave crest, the fluid velocity is in the wave propagation direction. The opposite is true for a wave trough. The x-component and z-component of the fluid particle acceleration are 90° and 180° out of phase with the surface elevation respectively. As a result; the maximum value of the horizontal component of the acceleration is beneath a wave node, while the maximum value of the vertical acceleration component is beneath a wave crest or trough.

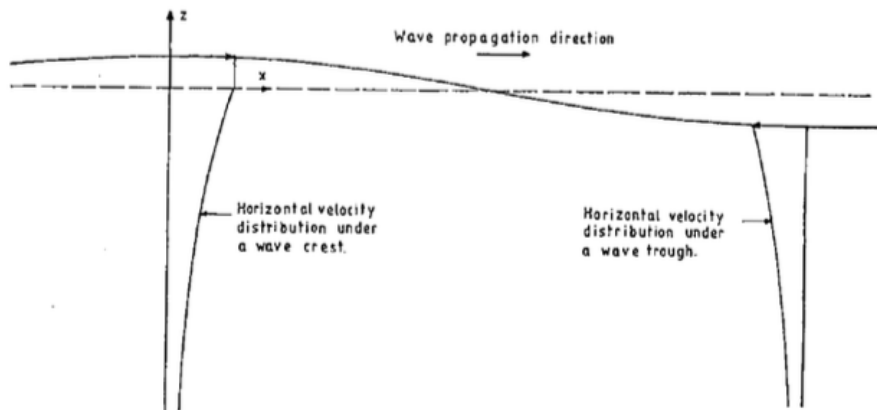


Figure 2.1: Horizontal velocity distribution under a wave crest and wave trough according to linear wave theory. Source: [6]

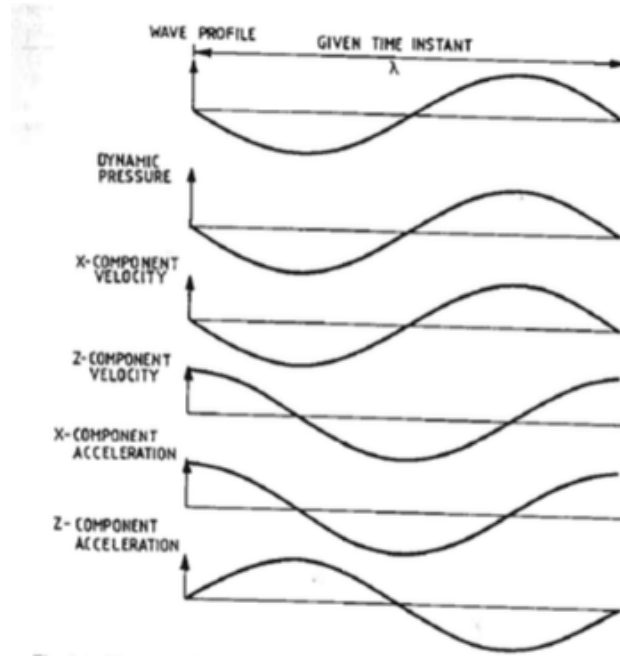


Figure 2.2: Surface elevation, pressure, velocity and acceleration in sinusoidal waves propagating in the positive x-direction. Source: [6]

2.2 Hydrodynamic Force

Hydrodynamic loads originate from the so-called radiation problem, where a fixed body is forced to oscillate with a frequency (ω) without the presence of incident waves. A body that is subjected to forced harmonic rigid body motions in the vertical direction will experience a steady-state hydrodynamic force, which can be expressed as [6]:

$$F_{3,hyd} = -A_{33}\ddot{\eta}_3 - B_{33}\dot{\eta}_3 - C_{33}\eta_3 \quad (2.8)$$

where A_{33} and B_{33} are the added mass and damping coefficients in heave, and C_{33} is the restoring force coefficient. The displacement, velocity and acceleration in the vertical direction are expressed as η_3 , $\dot{\eta}_3$ and $\ddot{\eta}_3$ respectively. In the vicinity of the free surface, the water will react differently depending on the oscillation frequency of the body. In turn, the added mass and damping coefficients are frequency dependent [9]. In infinite fluid, they will be independent of the oscillation frequency.

The total force in the vertical direction will also include an inertia contribution due to the mass (M) of the body. Newton's second law of motion expresses the inertia force as the sum of forces acting in the vertical direction:

$$M\ddot{\eta}_3 = \sum F_3 \quad (2.9)$$

Combining Equations 2.8 and 2.9, the total hydrodynamic force can be expressed as:

$$F_3 = -(M + A_{33})\ddot{\eta}_3 - B_{33}\dot{\eta}_3 - C_{33}\eta_3 \quad (2.10)$$

Harmonic sinusoidal motion is assumed, i.e. $\eta_3 = \eta_{3a} \sin \omega t$. Here η_{3a} is the amplitude of motion and ω is the oscillation frequency. Since the acceleration of the body is the time derivative of the velocity, they will be 90° out of phase with each other. In other words, they are orthogonal to one another. As a result of this orthogonality, the added mass and damping coefficients from Equation 2.10 can be separated and calculated by means of Fourier averaging. This involves integrating the measured vertical force multiplied with the acceleration or velocity over a number of periods (nT), as follows [12]:

$$A_{33} = -\frac{\int_{nT} F_3 \ddot{\eta}_3 dt + \int_{nT} C_{33} \eta_3 \ddot{\eta}_3 dt}{\int_t^{t+nT} \dot{\eta}_3 \ddot{\eta}_3 dt} - M \quad (2.11)$$

$$B_{33} = -\frac{\int_{nT} F_3 \dot{\eta}_3 dt}{\int_{nT} \dot{\eta}_3 \dot{\eta}_3 dt} \quad (2.12)$$

2.3 Linear and Quadratic Damping

The damping force that a body experiences is in reality non-linear. To account for this, the damping force component in Equation 2.10 can instead be expressed as the sum of a linear and quadratic term [5]:

$$B_{33} \dot{\eta}_3 = B_{33}^{(1)} \dot{\eta}_3 + B_{33}^{(2)} \dot{\eta}_3 |\dot{\eta}_3| \quad (2.13)$$

Linear damping is mainly due to wave generation, whilst quadratic damping includes effects due to friction and flow separation around the body. The non-linear term can be linearized, giving the following relation [5]:

$$B_{33} = B_{33}^{(1)} + \frac{8\dot{\eta}_{3a}}{3\pi} B_{33}^{(2)} \quad (2.14)$$

where $\dot{\eta}_{3a}$ is the amplitude of the velocity in heave. This is known as the linearized damping model. B_{33} can be calculated through the use of experimentally determined forces and motions (as shown in Equation 2.12) and plotted against $\dot{\eta}_{3a}$ or the KC number. According to DNV-GL's recommended practice [5], the linear damping coefficient, $B_{33}^{(1)}$, can then be found as the y-intercept of the resulting curve. The quadratic damping coefficient, $B_{33}^{(2)}$, can be found as the slope or by use of Equation 2.14.

It can also be assumed that the damping is completely quadratic in nature [5], i.e. $B_{33} = B_{33}^{(2)} \dot{\eta}_3 |\dot{\eta}_3|$. This is known as Morison's load model, which neglects the linear damping component completely. The non-linear damping component can therefore be expressed as:

$$B_{33}^{(2)} = \frac{3\pi}{8\dot{\eta}_{3a}} B_{33} \quad (2.15)$$

The linear damping coefficient is directly related to the amplitude of far-field waves generated by the oscillating body [6]. Alternatively, it can therefore be expressed as:

$$B_{33}^{(1)} = \rho L \left(\frac{\zeta_a}{\eta_{3a}} \right)^2 \frac{g^2}{\omega^3} \quad (2.16)$$

where ζ_a is the amplitude of the generated wave, η_{3a} is the amplitude of the body motion in heave, ω is the frequency of the generated wave, g is the gravitational acceleration, ρ is the fluid density, and L is the length of the body normal to the direction of wave propagation. This is known as wave radiation damping.

2.4 Morison's Equation and Hydrodynamic Coefficients

Morison's equation is a tool for modeling hydrodynamic forces in oscillatory flow, and can also be used to describe the forces on a heave plate. If the water is assumed stationary, the relative motion between the body and the water is only due to the vertical oscillation of the body through the water column [4]. Morison gives an estimate of the force acting on the body due to the surrounding water, which can be expressed as [6]:

$$F_{Morison} = F_M + F_D = \frac{\pi D^2}{4} \rho L C_M \ddot{\eta}_3 + \frac{1}{2} \rho D L C_D \dot{\eta}_3 |\dot{\eta}_3| \quad (2.17)$$

F_M is the inertia force due to the acceleration of the surrounding fluid, and consists of the Froude Kriloff force and diffraction force. The mass coefficient C_M is related to the added mass coefficient as $C_M = 1 + C_A$. F_D is the drag force due to viscous effects like flow separation. For a fixed structure in the presence of waves, Morison's equation can be used to calculate wave forces on the structure. Vertical water particle accelerations and velocities are then implemented.

The mass and drag coefficients in Equation 2.17 are non-dimensional. As a result, it is typical to express the added mass, damping, and drag force coefficients as non-dimensionalized hydrodynamic coefficients. These will be presented below.

Added Mass Coefficient:

The added mass can be non-dimensionalized using the equivalent infinite fluid added mass of a solid plate with width D and length L . This is expressed as [5]:

$$A_0 = \rho \frac{\pi}{4} D^2 L \quad (2.18)$$

The added mass coefficient can therefore be calculated using Equation 2.18 and the experimentally determined added mass found through Fourier averaging, as:

$$C_A = \frac{A_{33}}{A_0} = \frac{A_{33}}{\rho \frac{\pi}{4} D^2 L} \quad (2.19)$$

Damping Coefficient:

The damping force component can be non-dimensionalized in a similar manner as for the added mass, using the oscillation frequency ω and the experimentally determined damping found through Fourier averaging:

$$C_B = \frac{B_{33}}{\omega A_0} = \frac{B_{33}}{\omega \rho \frac{\pi}{4} D^2 L} \quad (2.20)$$

Drag Coefficient:

As was mentioned in Section 2.3, Morison assumes that the drag term is quadratic in nature. This can be seen in Equation 2.17, where the drag force is proportional to the squared velocity of the body in heave. The linear damping term, $B_{33}^{(1)}$, is therefore neglected.

The drag term is in phase with the velocity of the body, and will hence contribute to damping [9]. The non-dimensionalized drag coefficient can therefore be found by comparing the damping term in Equation 2.10 with Equation 2.17, and assuming that the damping is purely quadratic:

$$C_D = \frac{B_{33}^{(2)}}{\frac{1}{2}\rho DL} = \frac{3\pi}{8\eta_{3a}} \frac{B_{33}}{\frac{1}{2}\rho DL} \quad (2.21)$$

Normalized Force:

Another method of expressing the measured force in forced oscillations and waves is by use of the normalized hydrodynamic force, which is found through the non-dimensionalized added mass and damping coefficients. For the case of a harmonically oscillating plate with horizontal velocity $w = W \sin \omega t$, the normalized force amplitude can be expressed as [11]:

$$\frac{F}{\omega W A_0} = \sqrt{\left(\frac{A}{A_0}\right)^2 + \left(\frac{B}{\omega A_0}\right)^2} \quad (2.22)$$

In the case of a fixed plate in oscillating water (i.e. in the presence of incident waves), the normalized force includes a Froude Kriloff contribution and is expressed as:

$$\frac{F}{\omega W A_0} = \sqrt{\left(\frac{A + \rho V}{A_0}\right)^2 + \left(\frac{B}{\omega A_0}\right)^2} \quad (2.23)$$

2.5 Wave Excitation Forces

A body that is fixed and subjected to incident regular waves will experience wave excitation loads. The excitation loads are defined as the sum of Froude Kriloff and diffraction forces [6]:

$$F_{exc} = F_{FK} + F_{Diff} \quad (2.24)$$

The diffraction force is a consequence of the fact that a body present in waves disturbs the flow. There are two main categories of diffraction - wave diffraction and local diffraction. Wave diffraction occurs when the body disturbs the free surface, i.e. creates a diffracted wave field [9]. Local diffraction is when the body only disturbs the water locally. It can be assumed that the body dimension along the wave propagation direction (D) is small relative to the wave length (λ). With this assumption of long wave approximation, i.e. $\frac{\lambda}{D} \geq 5$, the diffraction force can be expressed as the sum of added mass and damping force components that are proportional to the accelerations and velocities at the geometrical center of the body. Long wave approximation in turn implies that the variation of velocity and acceleration over the body volume can be neglected [6].

The Froude Kriloff force is the force acting on the body due to the incident wave or motion of the fluid. It is calculated through the integration of the pressure in the incident wave over the body surface. If the body is fully submerged and small relative to the wave length, the Froude Kriloff force in heave can be approximated as $F_{FK,3} = \bar{a}_{0,3}\rho V$ [6], where V is the body volume and $\bar{a}_{0,3}$ is the mean vertical acceleration of the fluid particles at the body center.

The total excitation force in the vertical direction can therefore be defined as the sum of Froude Kriloff, added mass, and damping force components:

$$F_{exc,3} = \rho V \bar{a}_{0,3} + A_{33} \bar{a}_{0,3} + B_{33} \bar{v}_{0,3} \quad (2.25)$$

where $\bar{v}_{0,3}$ is the mean vertical velocity of the fluid particles at the geometrical center of the body. The added mass and damping force coefficients are found through Fourier averaging under the assumption of long waves. This equation also assumes symmetry about the vertical center plane, meaning that cross-terms for added mass and damping (A_{31} and B_{31}) are zero.

2.6 Parameter Dependence

2.6.1 Oscillating Flow

In an oscillating flow field, there are several non-dimensional parameters that influence the hydrodynamic force on a body. Sarpkaya, 1981 [19] studied the nature of the forces in Morison's equation (presented in Section 2.4) using data from sinusoidally-oscillating planar flow about smooth and rough circular cylinders. He suggested several non-dimensional parameters that influence the inertia and drag force coefficients. The three main non-dimensional parameters include:

1. Keulegan-Carpenter Number (KC):

The Keulegan-Carpenter number is defined as:

$$KC = \frac{U_m T}{D} = \frac{2\pi A}{D} \quad (2.26)$$

where U_m is the velocity amplitude, T is the oscillation period, D is the characteristic length scale of the body, and A is the amplitude of motion of the oscillating body.

For the case of a fixed body in waves at varying submergence, assuming infinite water depth, the Keulegan-Carpenter number is defined as:

$$KC = \frac{2\pi \zeta_a}{D} e^{(kz)} \quad (2.27)$$

where ζ_a is the wave amplitude, k is the wave number, and z is the submergence of the model relative to the mean water level (where z is defined positively upwards).

The added mass and drag coefficients in Morison's equation are dependent on flow separation, which in turn is dependent on the nature of the flow. In an oscillating flow, a body moves back and forth into its own wake. The behavior of the wake

will depend on the amplitude of the flow, i.e. how far the body oscillates. In simple terms, the KC number essentially defines the time available for vortices to form and shed. For large KC numbers, the flow regime is drag dominated due to the quadratic nature of the drag force term in Morison's equation [9]. The inertia term dominates for smaller KC numbers.

2. Reynolds Number (Re):

The Reynolds number is defined as:

$$Re = \frac{U_m D}{\nu} \quad (2.28)$$

where ν is the kinematic viscosity of the fluid.

Added mass and drag coefficients are dependent on the Reynolds number due to the point of separation, which is dependent on the behavior of the flow within the boundary layer. This Re dependence is most important for blunt shaped cylinders. When the flow separates, vortical structures are shed from the body. Vortices are characterized by high velocities, resulting in regions of low pressure in the wake between the points of separation. The pressure lacks symmetry at the fore and aft of the body, resulting in a drag force.

In addition, the separation points also depend on the KC number. This means that for different pairs of KC and Re , the added mass and drag coefficients will differ. It should be noted that since the added mass and drag coefficients are influenced by flow separation, they are also dependent on the geometry of the body.

3. Relative Roughness:

The coefficients are also dependent on relative roughness, which is defined as the ratio of the surface roughness (k) to the length scale of the body (D), i.e. k/D . This surface roughness is important due to the fact that it reduces the Re number dependency [9]. There is limited knowledge regarding the effect of roughness in oscillatory flow, but it is assumed that even small values of k/D may have a significant effect.

If it is therefore assumed that Morison's equation is valid, the added mass and drag coefficients for a body in an oscillating flow field will depend on the following three parameters:

$$C_A = f(KC, Re, \frac{k}{D}) \quad (2.29)$$

$$C_D = f(KC, Re, \frac{k}{D}) \quad (2.30)$$

Sarpkaya, 1981 [19] also assumed C_A and C_D to be functions of the time history, defined as the ratio of the time instant (t) to the oscillation period (T), i.e. t/T . He stated that there was, however, no simple way of dealing with the resulting expressions for the added

mass and drag coefficients, even for the most manageable time-dependent flows. The only option is to eliminate time as a parameter, considering only time-invariant averages instead. In the study by Sarpkaya [19], time-invariant C_A and C_D are calculated using Fourier averaging.

In addition, Sarpkaya [19] implied that the Reynolds number may not necessarily be the most suitable parameter for periodically oscillating flows. This is due to the fact that the term U_m appears in the expressions for both KC and Re . Instead, he introduced the frequency parameter $\beta = Re/KC = D^2/\nu T$ to replace the Reynolds number.

2.6.2 Ventilated Structures

Molin, 2011 [16] showed that the added mass of porous plates is significantly dependent on the amplitude of motion and accompanied by a strong damping. This is due to viscous effects, i.e. flow separation at the openings. Assuming that the openings are infinitely small and numerous, ventilated structures can be characterized by the following two additional parameters [15]:

1. The perforation ratio (r), which is defined as the open area of the plate divided by the total area.
2. The discharge coefficient (μ), which is dependent on the Reynolds number and the shape of the openings. Typical values for μ range between 0.3-0.4 for a perforated structure with porosity less than 50% [16].

Molin, 2001 [15] therefore introduced a new non-dimensional parameter based on the above two parameters called the porous KC number. This parameter is mostly valid for low amplitudes of motion, and reduces the spread in the data. It is defined as:

$$KC_{por} = \frac{A(1-r)}{D} \frac{1}{2\mu r^2} \quad (2.31)$$

2.6.3 Free Surface Oscillations

If a structure is forced to oscillate at or near the free surface, the added mass and drag force will be influenced by free surface phenomenon. As a result, the forces can vary greatly than those for corresponding amplitudes of motion when the model is oscillating in an infinite fluid. At increasing submergence, these free surface effects will decrease. At a certain depth limit, they disappear completely. C_A and C_D will therefore depend on the submergence below the free surface (z) until this depth limit is reached.

For a ventilated structure oscillating at or near the free surface, the added mass and drag coefficients are therefore dependent on the following parameters:

$$C_A = f(KC, Re, \frac{k}{D}, \frac{z}{D}) \quad (2.32)$$

$$C_D = f(KC, Re, \frac{k}{D}, \frac{z}{D}) \quad (2.33)$$

Chapter 3

Experimental Set Up & Procedure

This chapter outlines the experimental work done as part of this thesis to obtain the results which are to be presented in the upcoming chapters. Two main experiments are conducted:

- *Forced oscillation tests*
- *Wave tests*

Harmonically forced oscillation tests are performed to understand how added mass, damping, and drag coefficients vary with oscillation period, KC number, porosity, and submergence. Wave tests are conducted to determine the hydrodynamic loads on stationary plates in waves, both fully submerged and in close vicinity to the free surface, with varying wave period and steepness. As described in the introduction to this thesis, the main goal is to understand how the hydrodynamic loads and coefficients differ for these two test cases.

A description of the experimental test environment, including an outline of all relevant instrumentation and sensors, is given. The two perforated test models are presented, along with the test matrices for forced oscillations and waves.

3.1 Test Environment and Rig

Experiments are conducted in Ladertanken, which is a small-scale laboratory at NTNU's Tyholt facility. The laboratory is equipped with a two-dimensional wave flume tank, as well as various data measurement devices and sensors. The dimensions of the tank are 13m x 0.6m x 1.0m. The tank consists of a single flap wave generator at one end, and a parabolic wave damping beach at the other. An additional damping beach can be installed in front of the wavemaker for forced oscillation trials.

Figure 3.1 shows the main components of the experimental set up. The tank has rails and a carriage arrangement on the top, to which the test rig is installed. The carriage is clamped down to the tank walls to prevent horizontal and vertical motions during experiments. The carriage and rig configuration is placed at the middle of the tank, approximately 6.5m from each side. As shown in Figure 3.1b, the carriage is equipped with a vertical oscillator that generates the vertical motion of the test rig.

The top part of the rig consists of a triangular steel frame which is connected to a yellow wooden box, as shown Figure 3.1a. This box is attached to two plexi-glass plates with a thickness of 6mm. The distance between the plates and the tank walls is approximately

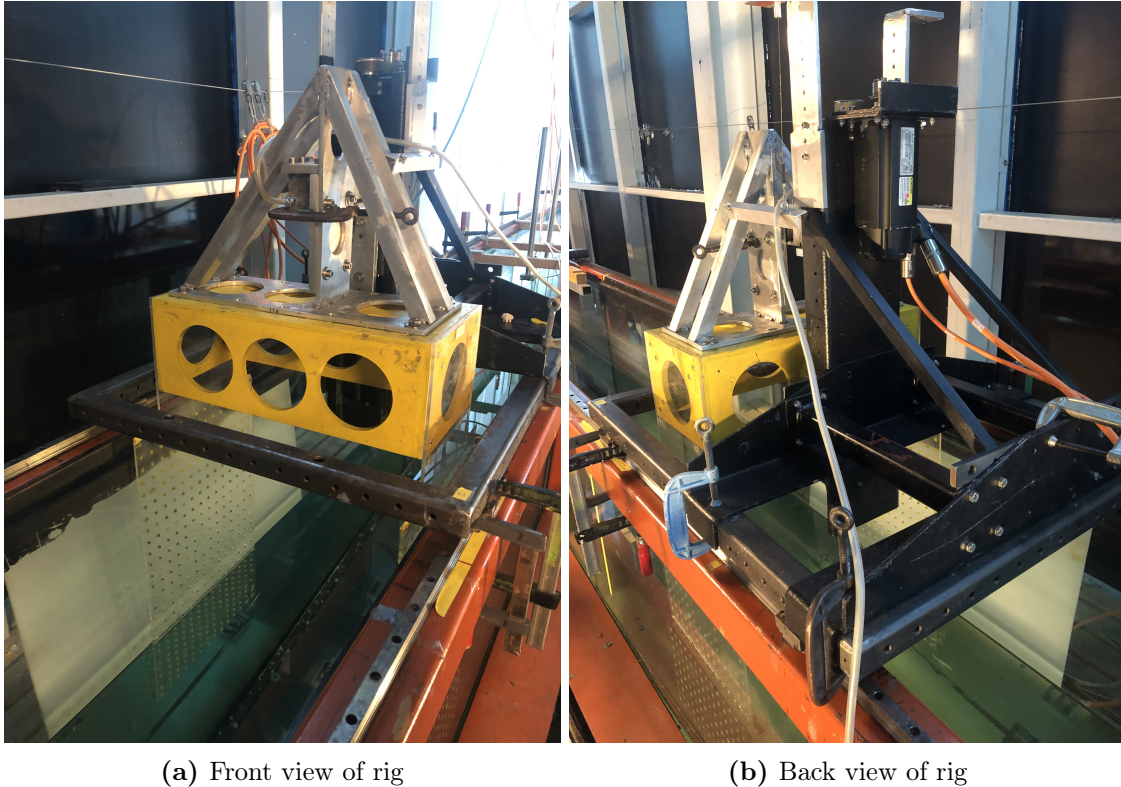


Figure 3.1: Set up of test rig in Ladertanken.

9mm on either side. The plexi-glass plates are fitted with a grid of holes which allow the models to be easily installed at different positions and submergence. Unused holes are plugged with yellow putty to prevent unwanted interaction effects at the openings during experiments.

Other parameters that define the experimental test environment are summarized below:

- The mean water level in the tank is measured daily, and found to vary slightly around 1 meter.
- The temperature of the water in the tank is also measured daily. The temperature readings vary between 21°C to 23°C.
- The parabolic beaches are installed approximately 0.5cm below the mean water level. For the case of forced oscillations trials, beaches are installed at both ends of the tank.

3.2 Test Models

Two ventilated plates are used in the experiments, both depicted in Figure 3.2. The models are referred to as C19 and C28 throughout the remainder of this thesis. Both models are aluminum rod screen (grill) models made up of a number of equally spaced circular cylinders. The overall dimensions of the models are the same. C19 (Figure 3.2a) consists of 24 circular cylinders and C28 (Figure 3.2b) consists of 21 circular cylinders. The dimensions and properties of these models are presented in Table 3.1.

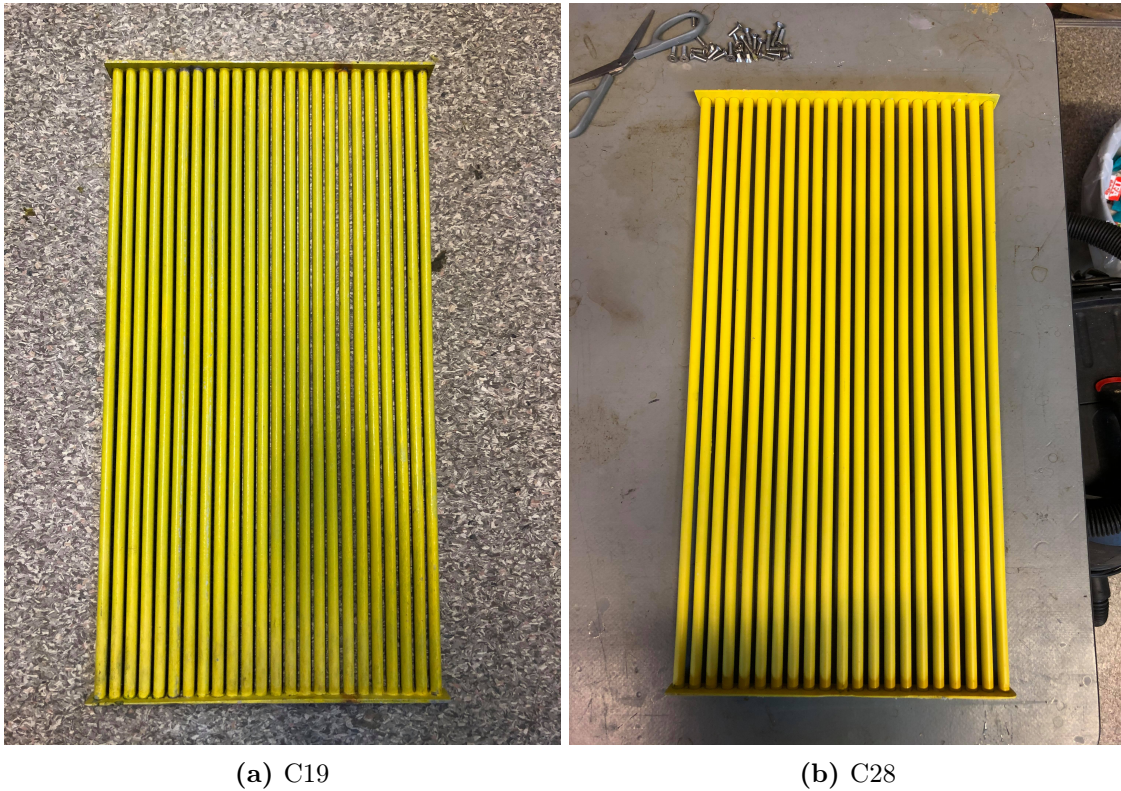


Figure 3.2: Test models.

Table 3.1: Characteristics of test models.

Model	Dimensions (DxLxt) [mm]	Rod Diameter [mm]	Mass [kg]	Perforation Ratio (r)
C19	297x570x10	10	3.01	0.189
C28	297x570x10	10	2.86	0.280

The cylinders that make up each model are welded to plates on both sides, allowing for easy installation of the models to the lower part of the rig. These end plates can be screwed to the grid holes in the plexi-glass plates. The first model (C19) is a pre-existing model with 10mm cylinders and a perforation ratio of 0.189. The second model (C28) has been constructed for the purpose of these experiments. It is made up of 10mm cylinders spaced wider apart, giving a perforation ratio of 0.280.

3.3 Test Matrices

3.3.1 Model Configurations

The forced oscillation and wave tests to be described in the following subsections are performed at four main submergences for C19 and C28. The descriptive names and values of each submergence are summarized below:

- **B25:** 25mm below the mean free surface

- **B50:** 50mm below the mean free surface
- **B75:** 75mm below the mean free surface
- **B100:** 100mm below the mean free surface

In addition, deep water forced oscillations are also conducted. For these tests, both models are installed at a submergence of 500mm below the mean water level. This submergence is for future reference referred to as **Deep**.

3.3.2 Forced Oscillation Matrix

The first part of these experiments involve harmonic forced oscillations, where the two models are fixed to the rig and forced to oscillate regularly in still water. The test matrix for the forced oscillation trials is presented in Table 3.2. Two oscillation periods of $T = 1.5s$ and $T = 2.0s$ are tested. A KC range of 0.1 - 2.0 (corresponding to oscillation amplitudes of 4.7mm and 94.5mm respectively) is used for the largest submergences. A smaller KC range is defined for the smallest depths to ensure that the models are fully submerged throughout all runs, resulting in fewer data points.

Each combination of oscillation period and KC number corresponds to a run that consists of a total of 40 oscillation cycles. A single cycle is defined by the body moving up and down over its mean position. This total number includes 5 ramp-up and 5 ramp-down cycles for each run. Each run therefore consists of a total of 30 full-amplitude oscillations. Deep water tests are conducted separately for both models, but all other submergences are conducted within a single run with a total duration of approximately 3 hours.

Table 3.2: Text matrix for all forced oscillation tests at $T = 1.5s$ and $2.0s$.

Submergence [mm]	Minimum KC [-]	Maximum KC [-]	KC Increment [-]	Total Runs
500	0.1	2.0	0.1	20
100	0.1	2.0	0.1	20
75	0.1	1.5	0.1	15
50	0.1	1.0	0.1	10
25	0.1	0.5	0.1	5

3.3.3 Wave Matrix

The second part of these experiments involves wave tests, where the models are fixed to the rig and subjected to incoming regular waves. The test matrix for wave tests is presented in Table 3.3. Wave tests are conducted at four main submergences: $z = -25, -50, -75,$ and $-100mm$. A total of five wave periods are tested, varying from $T = 0.9s$ to $T = 1.3s$ with steps of $0.1s$. The steepness (λ/H) is varied from 60 to 20 for each period, corresponding to a minimum and maximum wave amplitude of 10.5mm and 66mm for the defined period range. Each combination of wave period and steepness consist of 10 full-amplitude waves, as well as 5 ramp-up and 5 ramp-down cycles. Each submergence for both models is tested separately, where each test has a total duration of approximately 2 hours.

It should be noted that for depths of 75mm and 100mm, the models are fully submerged for all waves. For smaller submergences, however, the models are partly in and out of

water for the largest waves. This needs to be taken into account during post-processing, because the possibility of slamming makes it incorrect to calculate added mass and damping components using previously discussed methods. Instead, the results from these runs are to be presented as force time series showing measured force, Froude-Kriloff force, and diffraction force for $z = -25mm$. For $z = -50mm$, the data points corresponding to runs where the models are out of water will be removed.

Table 3.3: Test matrix for all wave tests.

Wave Period [s]	Minimum Steepness (λ/H)	Maximum Steepness (λ/H)	Steepness Increment (λ/H)	Total Runs
1.30	60	20	4	11
1.20	60	20	4	11
1.10	60	20	4	11
1.00	60	20	4	11
0.90	60	20	4	11

3.4 Instrumentation

3.4.1 Measurement System

To record data, HBM's Data Acquisition System (DAQ) is utilized. This system allows for data visualization, analysis and storage during measurements. The total measurement system is made up of sensors that send analog signals (in the form of an output voltage) to an amplifier and hardware filter. This signal is then relayed to an analog-to-digital converter. This digital signal is conveyed to a computer where it is interpreted, converted into physical quantities based on calibration data, and recorded. This process is illustrated in Figure 3.3.

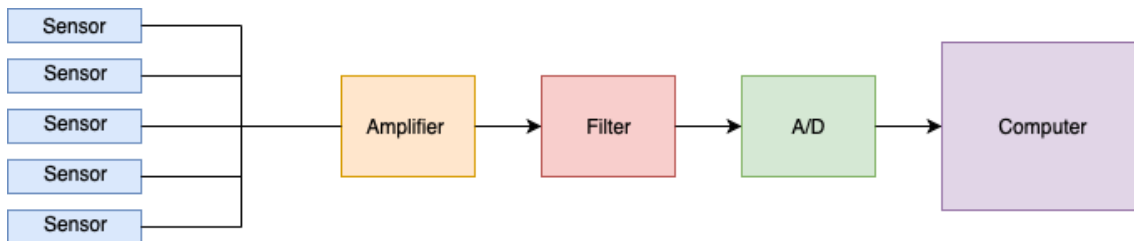


Figure 3.3: Data collection system.

Analog signals from numerous sensors can be recorded on different channels, and the resulting converted measurements are saved as binary files using the HBM Catman Easy software. Zero readings are taken for all relevant sensors in Catman Easy between each test to obtain a proper reference level for the data.

3.4.2 Sampling Frequencies

The sampling frequencies for experimental data vary for each test case, but are the same for each model. Table 3.4 summarizes the chosen sampling frequencies for forced oscillation tests and tests in waves.

Table 3.4: Sampling frequencies for each submergence.

Test Description	B25	B50	B75	B100	Deep
Forced Oscillations	200Hz	200Hz	200Hz	200Hz	200Hz
Tests in Waves	1200Hz	1200Hz	200Hz	200Hz	-

A low sampling frequency of 200Hz is used for all submergences for forced oscillation tests. This is done to make the resulting output file manageable, as most tests are conducted within a single run. Higher sampling frequencies are used for wave tests closer to the free surface due to the possibility of slamming occurrence. Slamming is a phenomenon with very short duration, thus a higher sampling rate is needed to correctly observe any resulting slamming peaks if present. The downside to this is large output files which are difficult to manage and time-consuming to analyze.

3.4.3 Sensors

The main types of sensors used during experiments are listed and described below:

- **One Force Transducer:**

A Wheatstone bridge force transducer is located at the upper part of the rig (on the steel triangular frame), connected to an actuator at the top. This force transducer measures forces in the vertical direction, and has a total capacity of approximately 6kN. This type of transducer measures the elongation of strain gauge wires in the form of an output voltage when a force is applied.

- **Two Potentiometers:**

A single potentiometer is used in all test cases. The potentiometer is a mechanical string type sensor, which by elongation measures changes in position. For forced oscillation tests, the potentiometer is fixed to the stationary part of the rig to measure changes in vertical position. For tests in waves it is installed at the uppermost point of the wave generator flap, where it records the horizontal position (amplitude) of the flap.

- **Three Accelerometers:**

Three accelerometers are used in these experiments. These are inertia based sensors which measure accelerations, and can be used to observe the vibrations of the rig. One accelerometer is installed at the top of the rig to measure accelerations in the vertical direction. The two remaining sensors are installed at the top of the rig and on one of the plexi-glass plates to measure accelerations in the x- and y-directions. Here y is defined along the width of the tank, and x is defined along the length. Their main objective is to observe the horizontal vibrations of the rig.

- **Six Wave Elevation Probes:**

A total of six wave probes are used in all test cases. Their configurations differ for forced oscillation tests and tests in waves, as illustrated in Figures 3.4 and 3.5. These figures also show the numbering of all probes, which are referred to as WP1 to WP6. The wave elevation probes consist of two electrical rods which measure the electricity of the water, where electrical measurements change with the submergence of the rods.

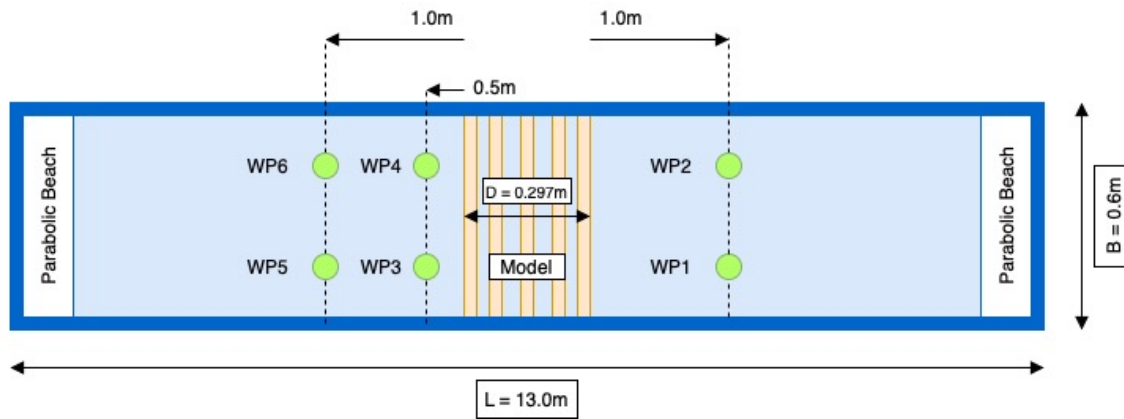


Figure 3.4: Set up of wave probes for forced oscillation tests.

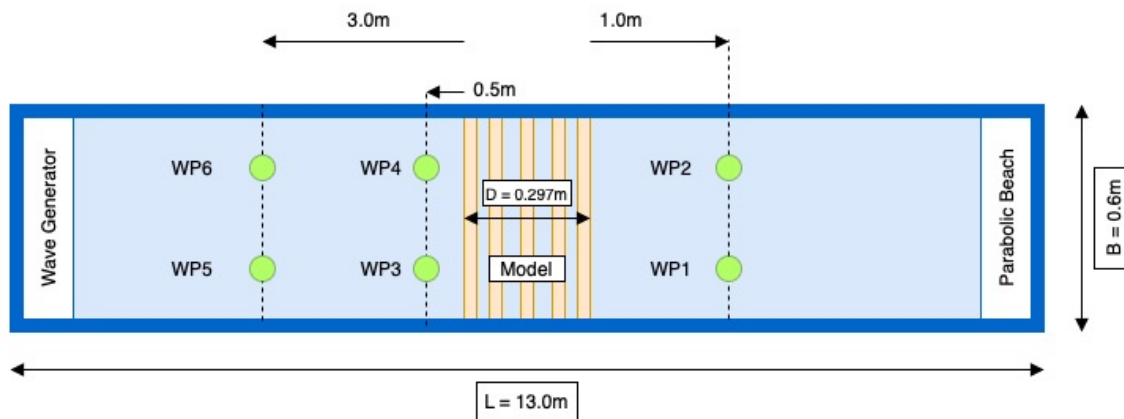


Figure 3.5: Set up of wave probes for tests in waves.

3.4.4 Calibration of Sensors

As previously stated, each sensor relays data in the form of an output voltage. Calibration is necessary to convert this output voltage into a physical quantity like force, position, or acceleration. This is achieved through the use of a calculated calibration factor, where the method of calibration varies for each sensor. The deterioration of this calibration factor over time depends on the sensitivity of each sensor to the external environment. This means that certain sensors must be re-calibrated more or less frequently than others.

The force transducer used in these experiments was quite robust, thus it was only calibrated at the start of the trials. However, daily checks were performed to validate the force measurements. This was done by placing a known weight on the top of the rig and measuring the resulting force in Catman Easy. The accelerometers and potentiometer were also less affected by the external environment, and did not need to be re-calibrated. Checks were performed every 3-4 days to ensure that the readings were correct within a certain tolerance limit. The wave probes were far more sensitive to the environment, and it became evident that the calibration factor varied greatly with the temperature of the water and water level in the tank. As a result, they were re-calibrated daily and their calibration factors were checked between each run. Due to contaminants in the water, these sensors were also cleaned weekly to avoid any build-up of dirt on the electrodes.

3.4.5 Calibration of Wave Generator

As already mentioned, a single flap wave generator is used in these experiments. This type of generator consists of a large flap that is hinged near the bottom of the tank, with a certain clearance to the tank bottom. The wave generator is dependent on two main parameters:

- Flap amplitude (A)
- Oscillation period (T)

While the oscillation frequency of the flap determines the period of the outgoing waves, the steepness of the wave (H/λ) is controlled by the flap amplitude. To create a wave with specific characteristics, the wave generator has to be calibrated for the given water depth in the tank. This results in a transfer function, which was then used to calculate the correct flap amplitude to be used as input to the wave generator. This transfer function was then validated by running an entire series of waves without the model present, and the resulting measured waves were checked against the desired wave heights. This was a time-consuming process, but the method of finding this transfer function will not be discussed in any more detail in this thesis.

Chapter 4

Procedure for Post-Processing of Experimental Data

This chapter presents the overall procedure for post-processing the raw experimental data recorded from each sensor described in Section 3.4 in Catman Easy. Data is saved by the data collection system in the form of binary files, which are then converted to readable files in Matlab. Various scripts and functions are created in Matlab to process the data and visualize the final results.

4.1 Forced Oscillations

With the exception of deep water oscillations, runs for all four submergences for each model (C19 and C28) are conducted at once. The duration of each test is approximately three hours, where all data is recorded in a single output file. Deep water oscillation tests for both models are conducted separately. To be able to determine the forces acting on the rig and plexi-glass plates, these tests are repeated with no model installed. These are referred to as empty rig tests, where only the rig itself is forced to oscillate. The procedure for post-processing data from these forced oscillation tests is outlined below:

I. Splitting Data:

Signals from all relevant sensors are split in two steps. First, the output file containing all runs is roughly split into individual submergence and runs based on the number of periods and number of runs per period (as defined in Table 3.2). As illustrated in Figure 4.1, all signals are also adjusted to oscillate around zero by subtracting the zero mean value from each time series.

The position signal is then split again to only include data from when the rig is oscillating with full amplitude, removing any parts of the signal defined as the waiting time between each run and all ramp-ups and ramp-downs. A total of 10 full amplitude oscillations are extracted from where the position signal is oscillating at a steady state. Force, acceleration and wave probe data corresponding to this position signal are also extracted. To check that the data is correctly extracted, the position signals for the empty rig test and test with model are plotted on top of each other for each period, KC number, and submergence. This is done to ensure that the signals are in phase with each other, proving that the corresponding forces also have the correct phase.

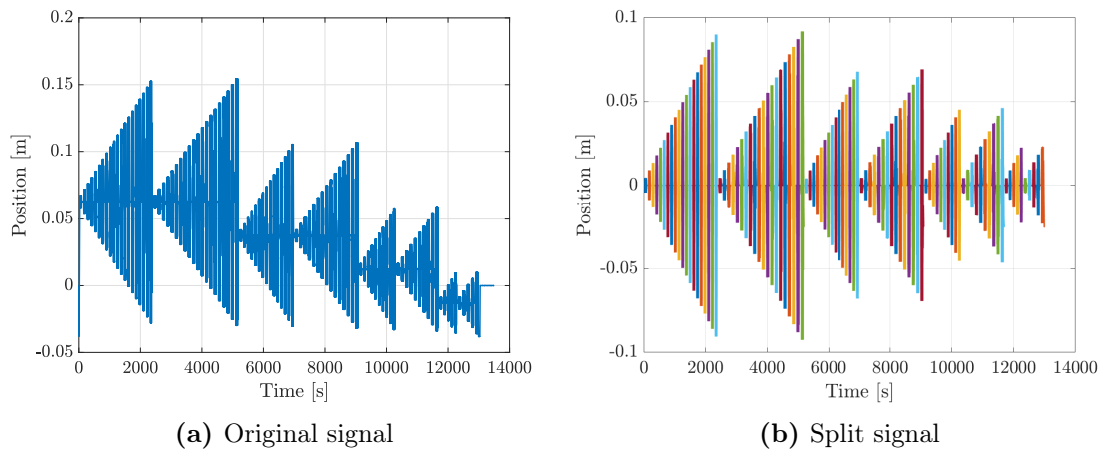


Figure 4.1: Splitting the recorded position signal for forced oscillation tests.

II. Data Filtering:

The extracted data is then filtered using a band-pass filtering technique. The data is converted from the time domain to frequency domain using Fast Fourier Transformation (FFT), making it possible to remove any frequencies from the signal that are associated with noise from the rig components and experimental environment. As part of the 2019 Project Thesis, pluck tests were conducted to determine the natural frequencies of the experimental components. Results showed natural frequencies of $17Hz$ and higher, where $50Hz$ was associated with electrical noise. Due to the low frequency of the data, it is possible to successfully filter this noise from the resulting time series.

The lower cut-off frequency is defined as $0.1Hz$ for all data. Wave probe, acceleration, and position readings are filtered slightly above the harmonic frequency, defined as the oscillation frequency (ω). Force readings are filtered to include higher order harmonics due to the assumed presence of higher order loads. The force signal is therefore filtered up to the 5^{th} order harmonic (5ω). The force is also filtered up to the first harmonic for comparison, and results show that the frequency band has very little effect on the resulting hydrodynamic coefficients. Figure 4.2 shows parts of the resulting filtered force and vertical acceleration signals.

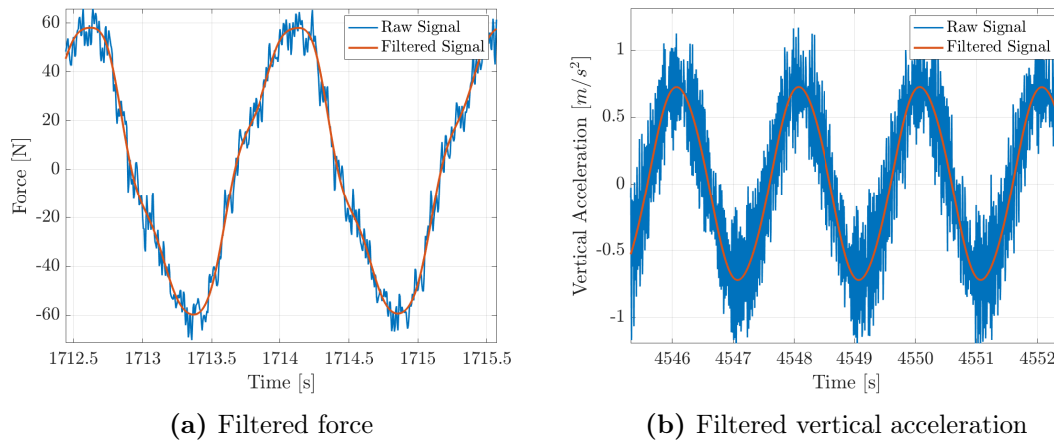


Figure 4.2: Data filtering for forced oscillation tests.

III. Velocity and Run Parameter Calculations:

The oscillation velocity is calculated two ways - by frequency domain integration of the vertical acceleration signal and differentiation of the position signal. This is done to compare the accuracy of both sensors. The potentiometer is a mechanical sensor that can overshoot and give incorrect position readings, and previous difficulties with the accelerometers are also taken into account. In addition, position and acceleration are calculated by further integration/differentiation of the acceleration and position signals respectively.

The calculated velocity from both methods is nearly identical for all periods and KC values, as shown in Figure 4.3a. The measured position signal and position calculated from the acceleration signal are also very similar, but the calculated position shows some deviations for the smallest oscillations. The same is observed for the measured acceleration signal and acceleration calculated from the position signal (see Figure 4.3b). As a result, the original position and acceleration readings are used for further calculations. The velocity found through frequency domain integration is chosen.

Run parameters like the oscillation amplitude, oscillation period, velocity amplitude, KC number, and porous KC number are then calculated using the velocity and position time series.

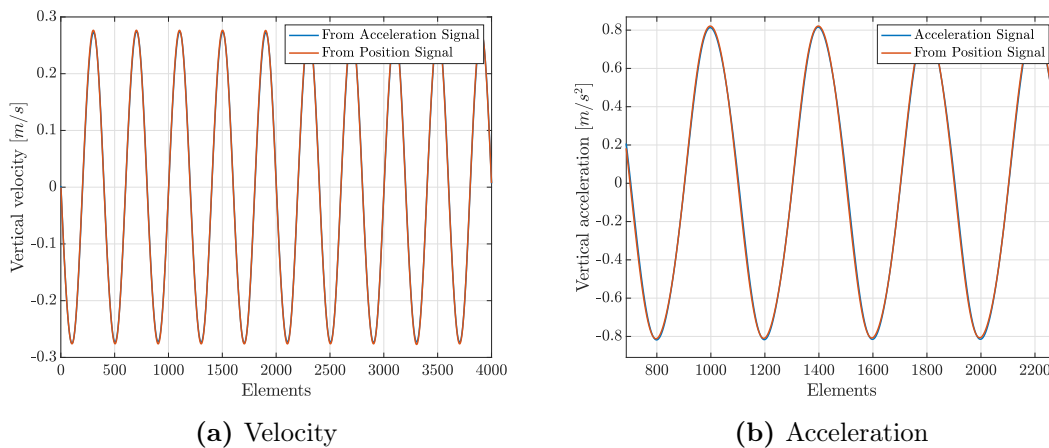


Figure 4.3: Calculated velocity and acceleration for forced oscillation tests.

IV. Hydrodynamic Force:

The total hydrodynamic force acting on the model is found by subtracting the empty rig force time series from the model force time series (as shown in Figure 4.4). In doing so, the restoring force and rig mass inertia are automatically eliminated. As described in Section 2.2, the hydrodynamic force can be split into inertia and damping force components. By subtracting the model mass inertia from the total inertia contribution, the added mass force component can also be found.

The added mass and damping coefficients are calculated using the Fourier averaging technique presented in Equations 2.11 and 2.12. The integration is carried out at once over the ten full-amplitude oscillations that were previously extracted from the total force signal.

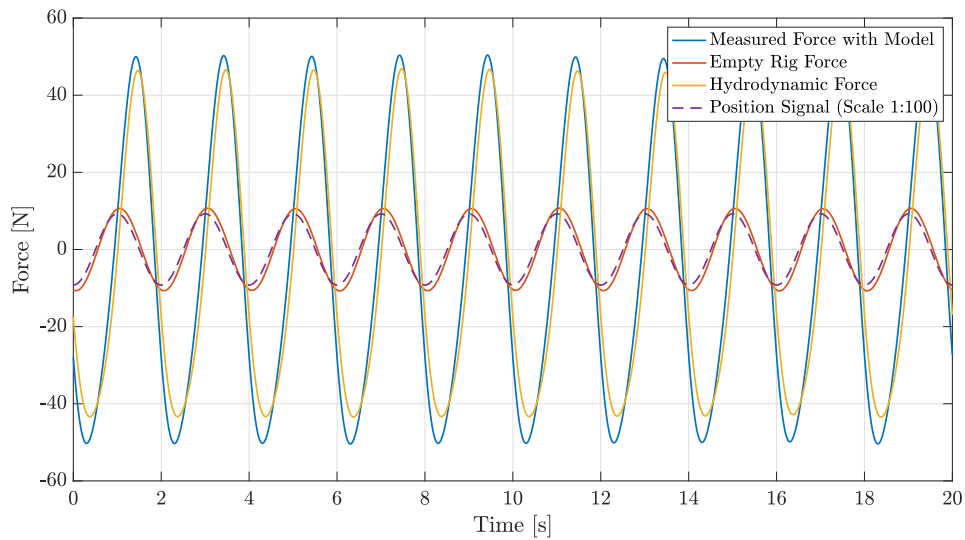


Figure 4.4: Calculated hydrodynamic force on model plotted against the filtered measured force, empty rig force, and vertical position signal.

V. Hydrodynamic Coefficients:

Non-dimensional added mass and damping coefficients are then calculated from the added mass and damping force coefficients using the equations in Section 2.4. This is done using the equivalent added mass of a solid plate. Drag coefficients are also calculated assuming Morison's load model, which as described in Section 2.3 assumes that the damping is completely quadratic in nature. Dimensional and non-dimensional coefficients for each plate and submergence are presented in the following chapter.

VI. Wave Radiation Damping:

Lastly, the wave radiation damping is calculated using Equation 2.16. This is carried out to determine how much of the total damping is due to wave generation. Readings from WP3, which is installed $0.5m$ from the edge of the model (as shown in Figure 3.4), are used to determine the average height and frequency of the radiated waves.

4.2 Tests in Waves

Unlike forced oscillations, runs in waves for all four submergences for each model (C19 and C28) are conducted separately. The duration of each run is approximately two hours. A single test without the model in place is also conducted to record an undisturbed wave signal at the center of the model. For this run, wave probes 3 and 4 are moved to the location of the rig. The same waves as described in Table 3.3 are used for this empty rig test case. The procedure for post-processing data from tests in waves is outlined below:

I. Splitting Data:

The first post-processing step is to split the raw data file for each model and submergence. The wavemaker signal is used to split data from all relevant sensors into individual runs corresponding to a specific wave steepness and period.

II. Finding Wave Phase at Model Center:

Since it is impossible to measure the wave elevation directly at the model center, finding the correct wave phase is an important step for further calculations. As previously mentioned, an empty run is conducted without the model in place, with WP3 and WP4 installed exactly at the location of the model. This run is then used to translate the incident wave for the run with the model to the plate center. This is achieved in four main steps:

- (1.) The *findpeaks* function in Matlab is used to extract full-amplitude wave cycles from WP6, WP3, and WP1 for runs both with and without the model in place. A total of five cycles are extracted for each period and steepness. To verify that the readings are consistent and in phase with each other, all full-amplitude cycles at WP6 (with and without the model installed) are plotted against each other and checked.
- (2.) The phase of the incident wave at WP6 for all runs with the model in place is calculated using a curve fitting technique in Matlab. By use of Equation 2.3, a sinusoidal wave is constructed using this calculated phase and wave amplitude readings from the undisturbed signal at WP3 for the empty run. To verify that the calculated phase is correct, this constructed wave is plotted against extracted signals at WP6, WP3, and WP1 from runs with the model in place. This is illustrated in Figure 4.5.

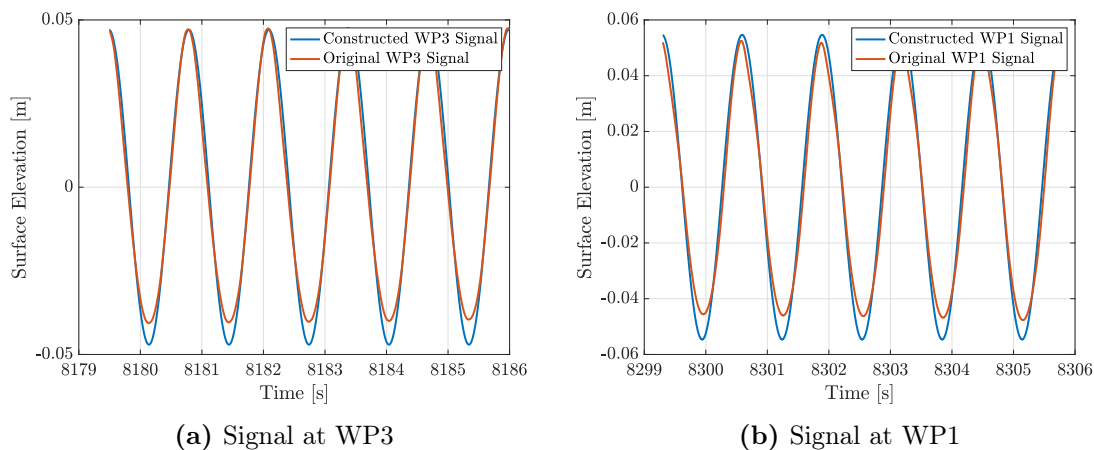


Figure 4.5: Comparison of constructed wave signal (ζ) and wave probe readings at WP3 and WP1.

- (3.) The next step is to find the wave propagation time from WP6 to the center of the model. This is done using the undisturbed wave probe signals from the runs without the model installed. Start times for the extracted signals from (1.) are multiplied with the sampling frequency to determine the number of elements between wave probe readings from WP6 to the center of the model, as well as from WP6 to WP1.
- (4.) WP1 readings are then used as a last step to verify that the correct wave probe signal can be extracted using the propagation times found in the previous step. Going back to runs with the model in place, the start time for WP6 and time between WP6 and WP1 are used to extract a WP1 signal from the run with the model in place. This is then plotted against the signal from WP1 without the model to check that these coincide.

III. Extracting Force and Filtering:

Using the start index from extracted readings for WP6 (with the model in place) and the number of elements the wave takes to propagate from WP6 to the center of the model, the correct force signal at the model center can also be extracted. This is illustrated in Figure 4.6a, where the split raw force signal is plotted against the wave at the model center. A total of 7 full-amplitude cycles are extracted for all runs.

The split raw force and wave probe signals are then filtered in a similar manner as for forced oscillations using a band pass filtering technique. The force is filtered up to the 5th order harmonic, while wave probe readings are filtered up to the first order harmonic, i.e. the wave frequency. The filtered force signal is illustrated in Figure 4.6b.

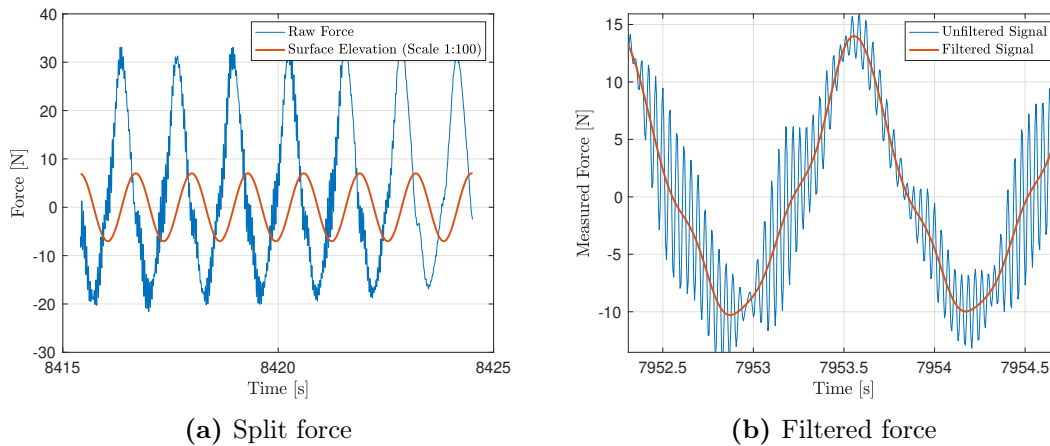


Figure 4.6: Split and filtered force signal for tests in waves.

IV. Calculating Run Parameters:

Run parameters like wave amplitude, wave period, KC number, and porous KC number are then calculated using wave probe signals. Undisturbed signals from WP6 (located 3m in front of the model and closest to the wave generator) for runs with the model in place are used to find the incident wave characteristics. This is done because disturbances in the water due to the presence of the model make it difficult to interpret readings from the wave probes closest to the rig.

V. Hydrodynamic Force:

The total Froude Kriloff force acting on the model is calculated as described in Section 2.5, using the wave particle acceleration at each rod center on C19 and C28. An example of this Froude Kriloff force is depicted in Figure 4.7. Vertical water particle velocity and acceleration are also calculated using Equations 2.5 and 2.7. Froude Kriloff force, velocity and acceleration are all found using the previously calculated wave phase, amplitude and frequency. The Froude Kriloff force is then subtracted from the filtered force time series to find the diffraction force. As shown in Equation 2.24, this diffraction force consists of added mass and damping components.

Fourier averaged damping and added mass coefficients are then calculated under the assumption of long wave approximation. This means that the wave particle velocity and acceleration are assumed constant over the model, and equal to that calculated at the model

center. In reality, wave particle velocity and acceleration will differ across the model. As a consequence, it is impossible to accurately separate force components which are proportional to velocity and acceleration, i.e. damping and added mass. Fourier averaging can thus only be used under this long wave assumption. As a result, the results for the shortest waves will be more prone to errors than the longest waves in these experiments.

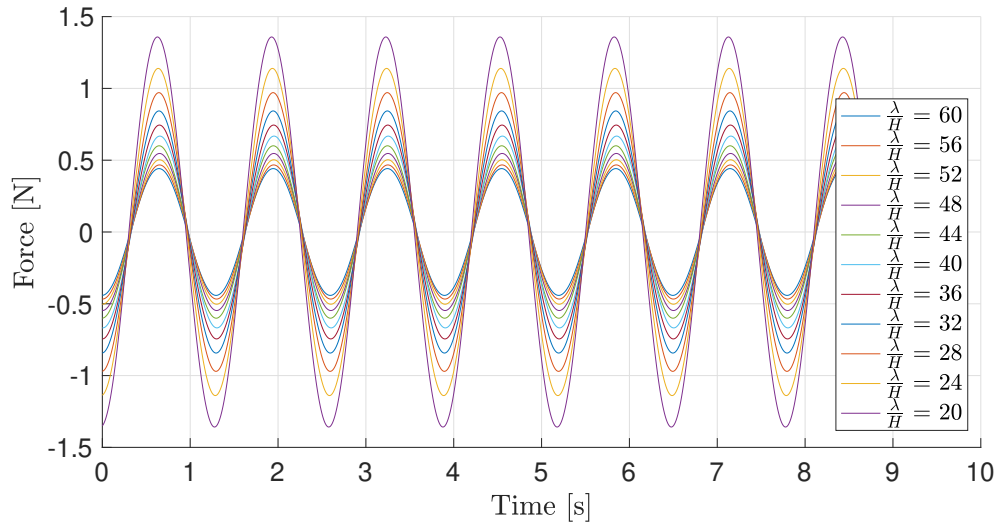


Figure 4.7: Total Froude Kriloff force acting on C19 for $T = 1.3s$ ($\lambda/D = 8.89$).

VI. Hydrodynamic Coefficients:

Similar to forced oscillation tests, the dimensionless hydrodynamic coefficients for added mass, damping, and drag are calculated using the equations presented in Section 2.4. The results are presented in the following chapter.

Chapter 5

Results & Discussion

This chapter presents the experimental results of this thesis. Results for forced oscillations and wave tests are first presented separately to properly identify the main trends observed with varying submergence and porosity, followed by a comparison of the hydrodynamic loads on structures oscillating in water and subjected to incoming waves. A discussion on experimental errors is also included.

5.1 Forced Oscillations

The results presented in this section serve three main purposes - to validate the experimental and post-processed data against existing theory on perforated models in oscillating flow, to understand how the hydrodynamic coefficients (added mass and damping) differ for varying submergence, and to observe how the perforation ratio affects the total hydrodynamic loads.

5.1.1 Force Times Series

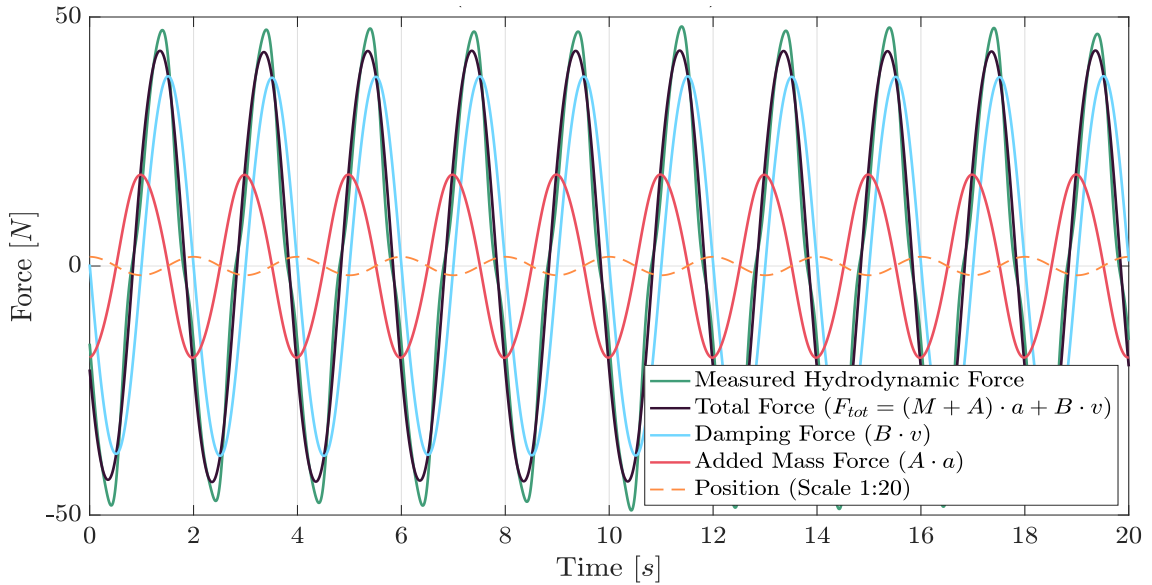


Figure 5.1: Force time series for C19 ($r = 0.189$) with ten full-amplitude oscillation cycles. Results are for deep water oscillations ($z/D = -1.68$) at $T = 2.0s$ and $KC = 2$.

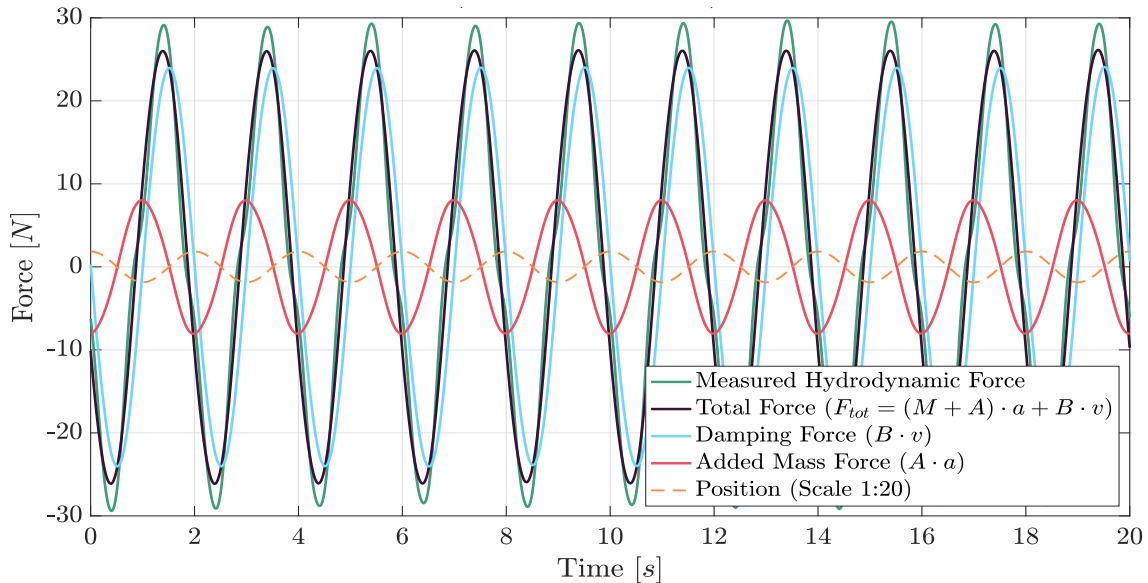


Figure 5.2: Force time series for C28 ($r = 0.280$) with ten full-amplitude oscillation cycles. Results are for deep water oscillations ($z/D = -1.68$) at $T = 2.0s$ and $KC = 2$.

To start off, an example of force time series in deep water ($z = -50cm$) for the models (C19 and C28) are presented in Figures 5.1 and 5.2. These time series, as well as the additional plots to be presented throughout this chapter, are the resulting product of the post-processing procedures described in Sections 4.1 and 4.2. For the case of forced oscillations, the force time series include 10 full-amplitude oscillations extracted at a point in time when the model is oscillating at a steady state. They are presented to show some important features of the measured hydrodynamic force and the resulting force components. Additional force time series for C19 and C28 at varying submergence, oscillation period, and oscillation amplitude are included in Appendices B.1 and B.2.

The time series in Figures 5.1 and 5.2 include five main sources of data - the measured hydrodynamic force, the total re-calculated hydrodynamic force, the damping and added mass force components, and the position signal (which is scaled up by a factor of 20). The total hydrodynamic force is re-calculated using the Fourier averaged added mass (A) and damping (B) coefficients defined in Section 2.2. This is a first-order force, as the Fourier averaging technique does not take into account the effects of higher order harmonics. The measured force is filtered to include higher order harmonics (3ω and 5ω). As described in Section 4.1, the empty rig force has been subtracted from the total measured force to obtain the hydrodynamic force acting on the model only. The results show good agreement between the re-calculated force and the measured force. If plotted against the measured force filtered around the oscillation frequency only, the two are nearly identical. This shows that Fourier averaged added mass and damping components can be used to accurately predict the first order hydrodynamic loads on models in oscillatory flow. The measured force in Figures 5.1 and 5.2 has slightly higher peaks and troughs than the first order force, indicating that there are higher order loads present in the total hydrodynamic force acting on the models.

The added mass force component in Figures 5.1 and 5.2 is proportional to the acceleration, thus it is 180 degrees out of phase with the motion of the model. The damping force component is proportional to the model velocity, and thus 90 degrees out of phase with

the position signal. The phase of the total force depends on the magnitude of the added mass force. When the added mass component is sufficiently small, the total hydrodynamic force is nearly in phase with the damping force. This entails a clear damping dominance, which is the case for all experimental runs.

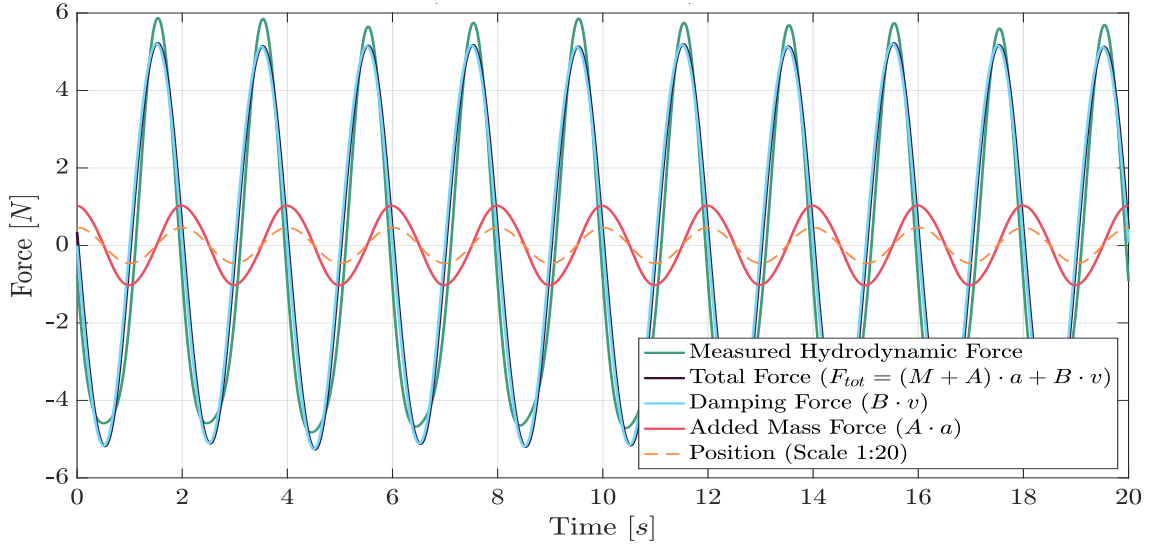


Figure 5.3: Force time series for C19 ($r = 0.189$) with ten full-amplitude oscillation cycles. Results are for oscillations at $z = -2.5\text{cm}$ ($z/D = -0.08$) at $T = 2.0\text{s}$ and $KC = 0.5$.

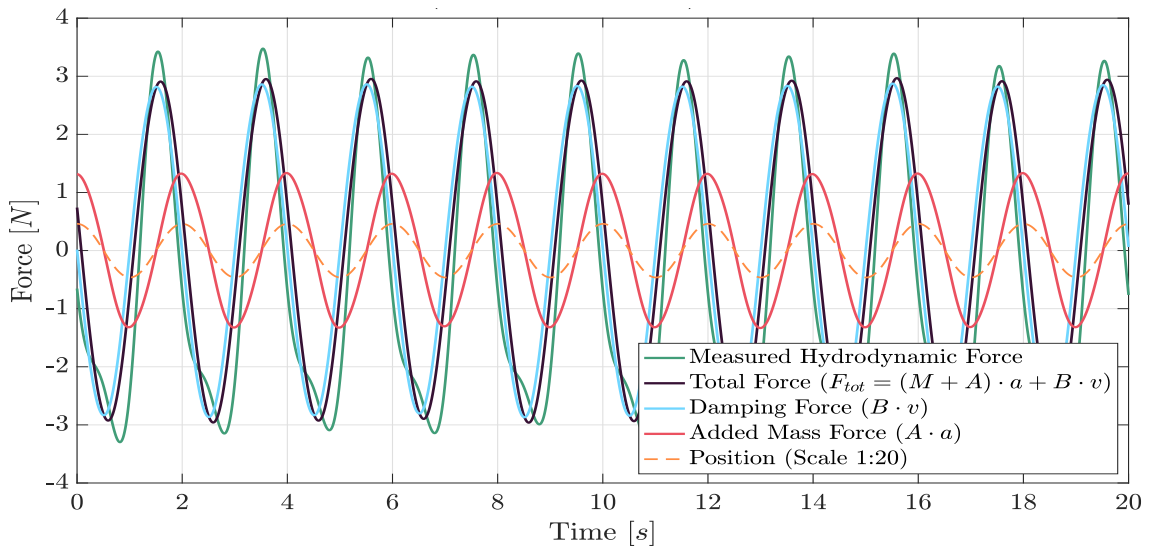


Figure 5.4: Force time series for C28 ($r = 0.280$) with ten full-amplitude oscillation cycles. Results are for oscillations at $z = -2.5\text{cm}$ ($z/D = -0.08$) at $T = 2.0\text{s}$ and $KC = 0.5$.

Figures 5.3 and 5.4 show examples of force time series for C19 and C28 when the damping force is highly dominant to the added mass force. These are for forced oscillations at $z = -2.5\text{cm}$ (i.e. directly beneath the free surface). Lower amplitudes were conducted for these tests to ensure that the models were fully submerged for all values of KC , thus the tested KC range is limited to $KC = 0.5$. In contrast to deep water oscillations, the added mass force is in phase with the position signal. This implies that it is negative for

this given oscillation period and KC number. The damping force is nearly identical to the re-calculated hydrodynamic force, which implies that its contribution to the overall hydrodynamic loads on the models increases with increased proximity to the free surface. This damping dominance, as well as the behavior of the added mass coefficients close to the free surface, will be the subject of discussion later in this section.

5.1.2 Deep Water Oscillations vs. Semi-Analytical Method by Fredrik Mentzoni

Fredrik Mentzoni, 2019 [13] has proposed a semi-analytical method for estimating non-dimensional added mass and damping coefficients for perforated plates in an infinite fluid. This semi-analytical method is based on Graham's analytical method (as presented in Section 1.3), where the resulting parameters have been curve fitted to CFD results for perforated models in oscillating flow conditions. Equations 1.1 and 1.2 are used in combination with the coefficients presented in Table 1.1 to produce three curves for perforation ratios $r = 0.20, 0.30,$ and 0.50 . These are plotted against the experimentally determined added mass and damping coefficients for C19 and C28 in deep water ($z = -50\text{cm}$) in Figures 5.5 and 5.6.

The purpose of this comparison is to obtain a visual representation of how the cylindrical shape affects the resulting hydrodynamic coefficients, but most importantly to provide a validation of the experimental results and the presented method suggested by Mentzoni. The semi-analytical method is based on CFD simulations with sharp-edged cylindrical models. It was therefore assumed that experimental results would lie on the lower side of the corresponding curves suggested by Mentzoni. The added mass and damping curves follow the same trend as the semi-analytical results. They converge towards zero for small KC values, and follow a steadily increasing curve with increasing oscillation amplitude. This shows that the coefficients are clearly dependent on the oscillation amplitude. It can be assumed based on the overall agreement in the trends that the experimental results are within reason.

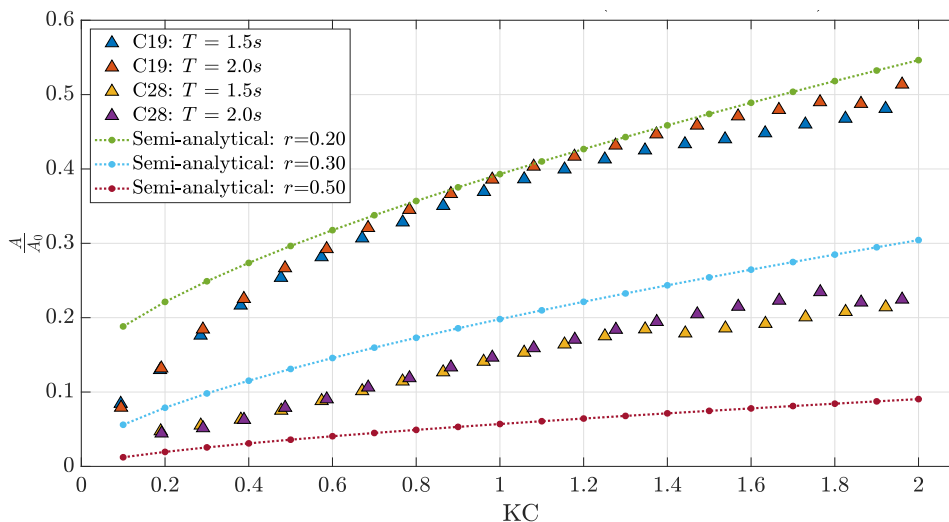


Figure 5.5: Non-dimensional added mass coefficients for C19 ($r = 0.189$) and C28 ($r = 0.280$) for forced oscillations in infinite fluid ($z = -50\text{cm}$). The results are plotted against values from the semi-analytical method suggested by Mentzoni, 2019 [13] for three different perforation ratios.

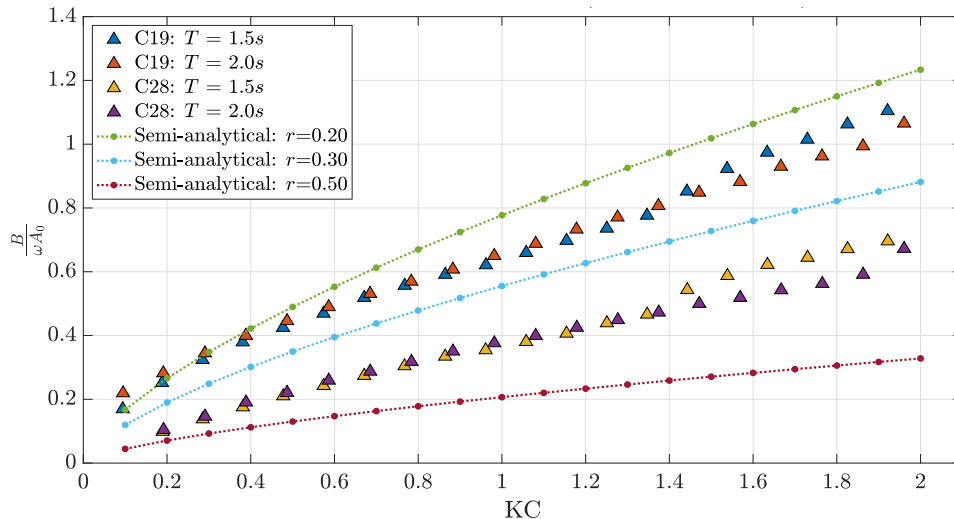


Figure 5.6: Non-dimensional damping coefficients for C19 ($r = 0.189$) and C28 ($r = 0.280$) for forced oscillations in infinite fluid ($z = -50\text{cm}$). The results are plotted against values from the semi-analytical method suggested by Mentzoni, 2019 [13] for three different perforation ratios.

For C28, both the added mass and damping coefficients are lower than the semi-analytical results for $r = 0.30$ at all values of KC. This could suggest that local Reynolds number effects, i.e. differences in flow separation at the plate openings due to differing cylindrical shapes, is of importance for larger perforation ratios. For C19, there is good agreement between the damping coefficients at low KC numbers. At higher values of KC, the damping coefficients for C19 are lower than those suggested by the semi-analytical method. Added mass coefficients show large differences at small oscillation amplitudes, but surprising similarities are observed for increasing KC numbers.

In his more recent study, Mentzoni [14] discussed the importance of cylinder shape by comparing experimental results for C19 to numerical results of a model denoted S19 with the same perforation ratio and overall dimensions, but with square cylinders. He showed that damping and added mass coefficients were larger for S19 than for C19, most likely as a result of different cylinder shapes. He also discussed this in terms of the numerical method suggested by Molin, 2011 [16] based on potential flow theory and neglecting the effects of plate end separation. Molin suggested that the hydrodynamic coefficients only depend on the porous KC number (presented in Equation 2.31 in Section 2.6), which is dependent on the perforation ratio and discharge coefficient μ . This method is, however, mostly valid for small values of KC. The experimentally determined added mass coefficients for C19 at low KC values support the analysis of discharge coefficients. They are significantly lower than the added mass predicted by the semi-analytical method, i.e. showing clear dependence on the shape of the openings. The values at larger KC numbers contradict Molin's analysis - they are quite similar to the semi-analytical coefficients, i.e. not dependent on the discharge coefficient. This could indicate that plate-end flow separation is more important than the shape of the cylinders as the oscillation amplitude increases, which is a phenomenon that is neglected in Molin's method.

5.1.3 Effect of Submergence on Hydrodynamic Coefficients

Experiments are performed with z/D values ranging from -0.08 to -1.68 for the smallest and largest submergences respectively. The aim is to understand how the added mass and damping coefficients vary as the distance to the free surface is decreased. This is of particular importance for offshore installations of subsea modules, where the wave zone forces are the most difficult to accurately estimate.

Added Mass Coefficients:

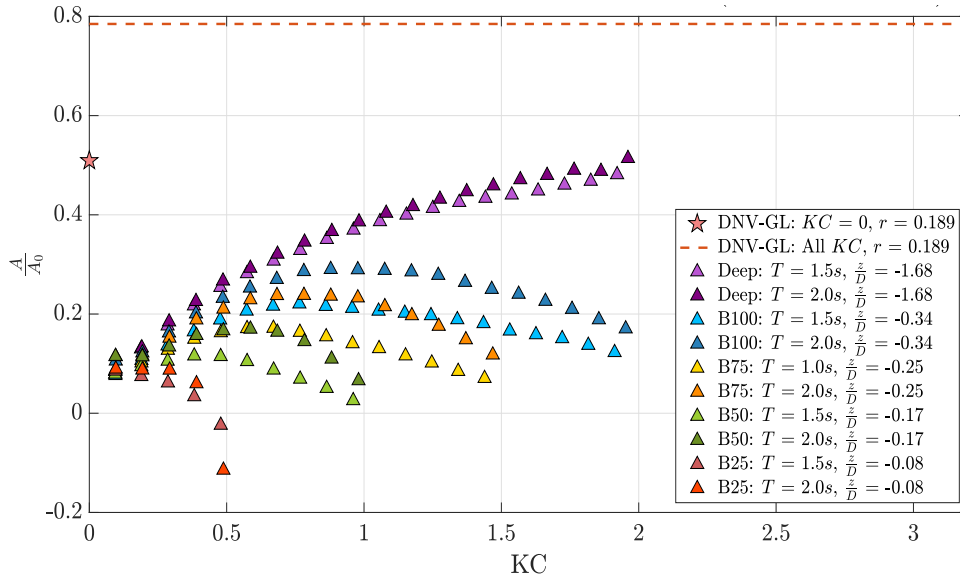


Figure 5.7: Non-dimensional added mass coefficients vs. KC for C19 ($r = 0.189$) plotted against DNV-GL's [5] suggested values.

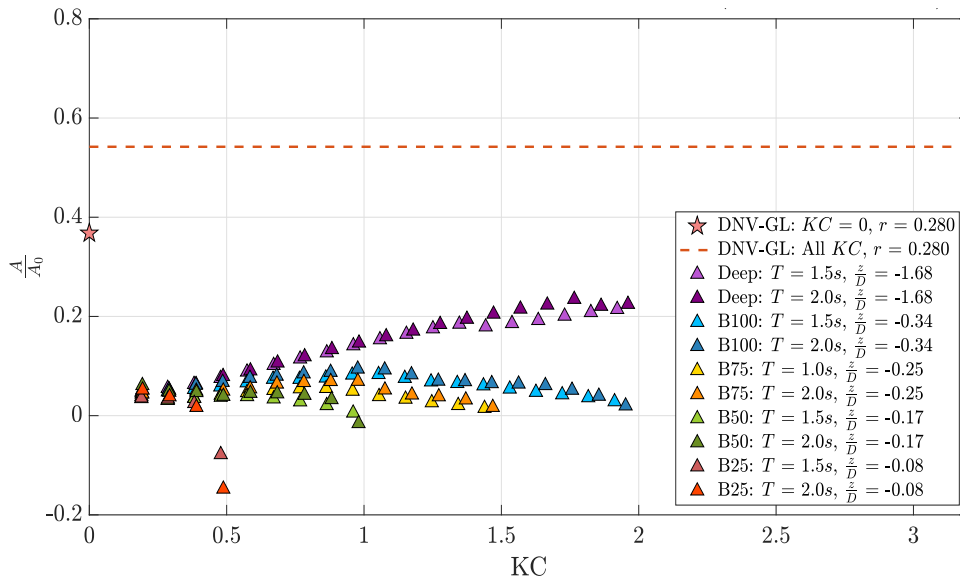


Figure 5.8: Non-dimensional added mass coefficients vs. KC for C28 ($r = 0.280$) plotted against DNV-GL's [5] suggested values.

The non-dimensional added mass coefficients for C19 and C28 are presented in Figures 5.7 and 5.8. A steady increase in added mass is observed for both models for deep water oscillations ($z/D = -1.68$), as was presented in the previous subsection. The trend in added mass for smaller submergences is interesting - there is a clear convergence towards zero and negative values as the KC number increases. Added mass coefficients increase towards a maximum value, followed by a steady decrease for larger amplitudes of motion. This maximum KC value seems to be similar for both models at each value of z . This initial increase is smaller for the lowest submergences, and for $z/D = -0.08$ there is a sudden drop towards negative values for both models. An, 2014 [1] observed the same trends for experiments at a submergence of 10cm for a plate with porosity $r = 0.159$. While damping coefficients increased with the KC number, the added mass had a maximum at $KC = 0.9$ (which is also observed for C19 and C28 at the same submergence) and then decreased for larger amplitudes. It is assumed that these trends are the result of free surface interactions and changes in the flow field around the body. Results also show that the added mass is amplitude dependent for both models, but more so for C19 than C28. As is to be expected, there is very little to no dependence on the oscillation frequency in deep water. For C19, this frequency dependency increases near the free surface. For C28, however, there seems to be significantly less dependence on the oscillation frequency for the same submergences. It can be assumed that differences in the flow field around each model, as well as how the models interact with the surrounding fluid, are the primary causes.

The experimentally determined added mass coefficients are also compared to values calculated using the approximated formulas suggested by DNV-GL [5] in Equations 1.4 and 1.5. For C19, the zero amplitude ($KC = 0$) value by DNV-GL seems valid up to $KC = 2$, but for higher ranges a correction would need to be applied. For most KC values, the zero amplitude estimates are conservative for both C19 and C28. The suggested values for all KC numbers are even more conservative for each perforation ratio, but as stated in their recommended practice, this value also includes a considerable safety margin. As previously mentioned, DNV-GL only includes approximated formulas that are dependent on the perforation ratio. Other factors like submergence and model geometry are not taken into account. It is also evident that the added mass coefficients are highly amplitude dependent, thus these estimates do not provide accurate information for most ranges of KC. This emphasizes the importance of model tests or numerical studies when estimating the hydrodynamic loads in oscillating fluids.

Damping Coefficients:

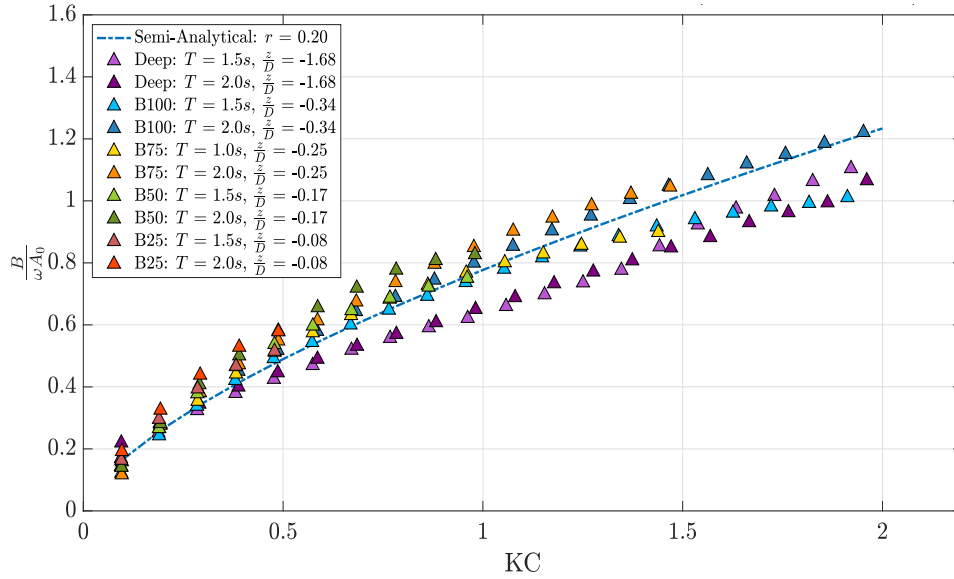


Figure 5.9: Non-dimensional damping coefficients vs. KC for C19 ($r = 0.189$) plotted against semi-analytical damping coefficients by Mentzoni, 2019 [13].

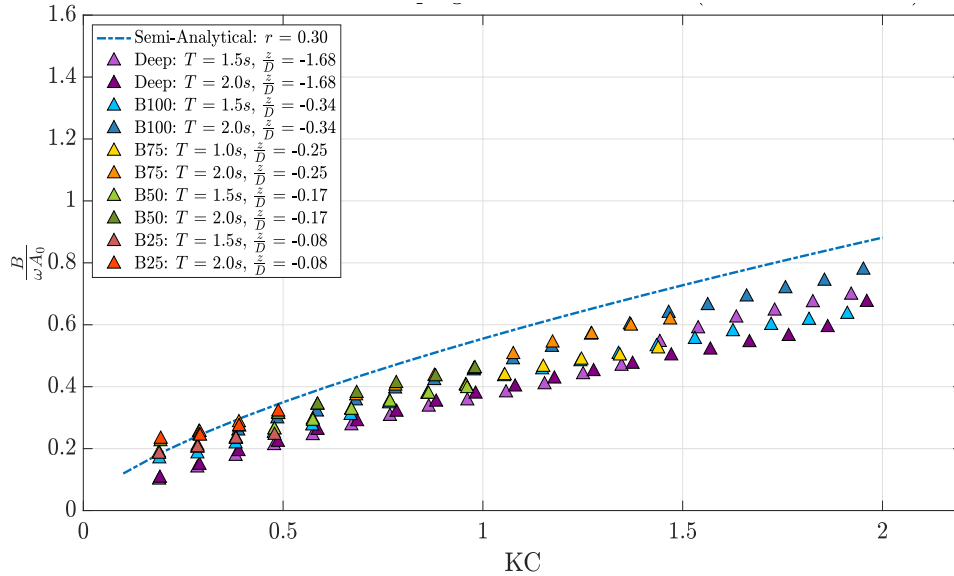


Figure 5.10: Non-dimensional damping coefficients vs. KC for C28 ($r = 0.280$) plotted against semi-analytical damping coefficients by Mentzoni, 2019 [13].

Figures 5.9 and 5.10 present the non-dimensional damping coefficients for C19 and C28. These have been non-dimensionalized using the oscillation frequency and the equivalent added mass of a solid plate. By comparing these damping coefficients to the previously depicted added mass coefficients, it becomes evident that the damping force component is dominant for all submergences. As discussed in Section 1.4, this damping dominance is to be expected. For deep water oscillations ($z/D = -1.68$), the damping force for C19 is approximately 2 times the added mass contribution for both periods. For C28, the damping

force is almost 3 times larger for most values of KC at both periods. By looking back at the curves for added mass, it can be noted that the damping dominance increases significantly with decreasing submergence. Unlike the added mass, there is a steady increase in the damping coefficients for all KC numbers. They are also dependent on the oscillation amplitude, but less dependent on the oscillation frequency at all submergences. It is evident that the damping force increases with decreasing proximity to the free surface, which coincides with the corresponding decrease in added mass for the same submergences. The differences with submergence are, however, smaller than those observed for the added mass coefficients.

The damping coefficients are also plotted against the semi-analytical values suggested by Mentzoni, 2019 [13] for perforation ratios $r = 0.20$ and $r = 0.30$. Data points for C28 lie below this curve, but similarities for the smallest submergences are observed for low values of KC. As previously discussed, differences for C28 are most likely due to differences in the shapes of the cylinders and thus the local flow field around the body. Experimental results for C19, however, lie both above and below the curve for $r = 0.20$. Mentzoni's results are based on CFD simulations in deep water, and it is assumed that the global flow field is dominant for the overall hydrodynamic forces with decreasing porosity (i.e. the differing cylindrical shapes are less important). As a result, these trends seem within reason.

Wave Radiation Damping:

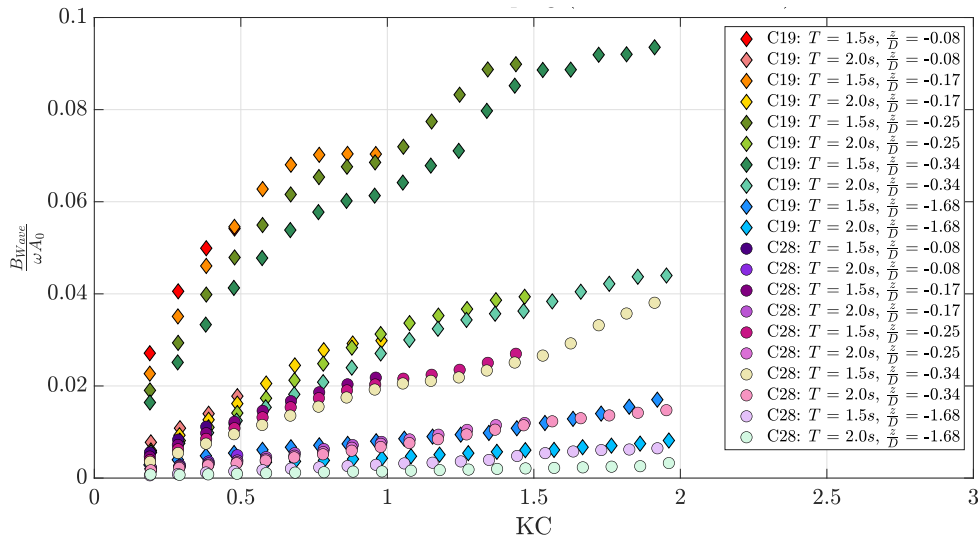


Figure 5.11: Non-dimensional wave radiation damping for C19 ($r = 0.189$) and C28 ($r = 0.280$) at all submergences for $T = 1.5s$ and $T = 2.0s$.

The wave radiation damping is calculated using the radiated wave signals at wave probes positioned near the model. The resulting non-dimensionalized wave radiation damping for both models at all periods and submergences is presented in Figure 5.11. The wave radiation damping is small compared to the total damping force. There is a significant difference between oscillations in deep water ($z/D = -1.68$) and all other submergences, as is to be expected. Oscillations at smaller depths cause disturbances in the free surface, increasing the overall damping contribution. This could partly explain why the damping coefficients increase for decreasing submergence, and why the added mass coefficients show a significant decrease for higher values of KC.

As discussed in Section 2.3, the total damping force can be decomposed into linear and nonlinear components. Linear damping is a result of linear phenomena, like wave radiation and skin friction due to laminar boundary layers. Nonlinear damping is mainly associated with local and global vortex shedding and flow separation. The low wave radiation damping coefficients emphasize the fact that the damping is mainly nonlinear, i.e. quadratic in nature. This would imply that Morison's load model is valid, meaning that the linear damping term can be neglected. This can in turn imply that the damping force that the models experience in harmonic oscillations is highly influenced by the resulting flow field around the body.

Drag Coefficients:

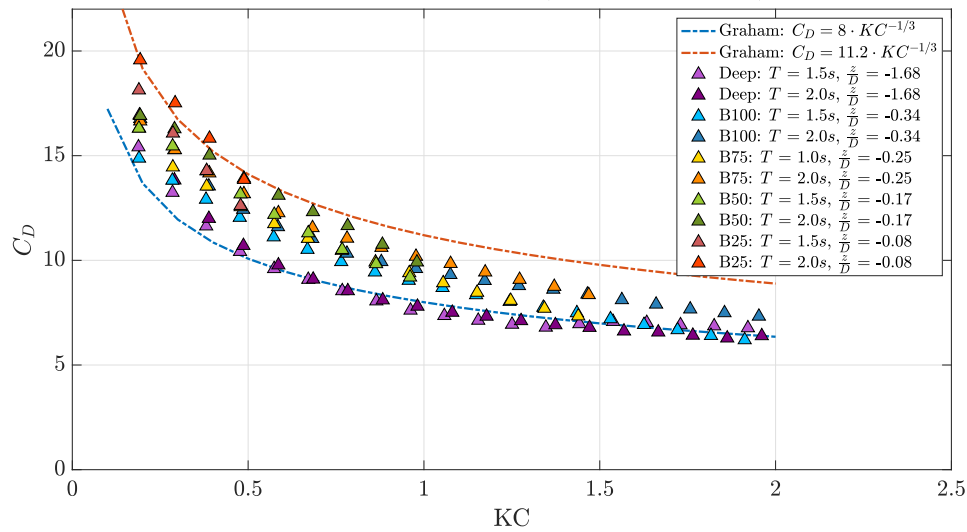


Figure 5.12: Drag coefficients vs. KC for C19 ($r = 0.189$) for all submergences and periods. Results are plotted against the suggested curves by Graham, 1980 [7].

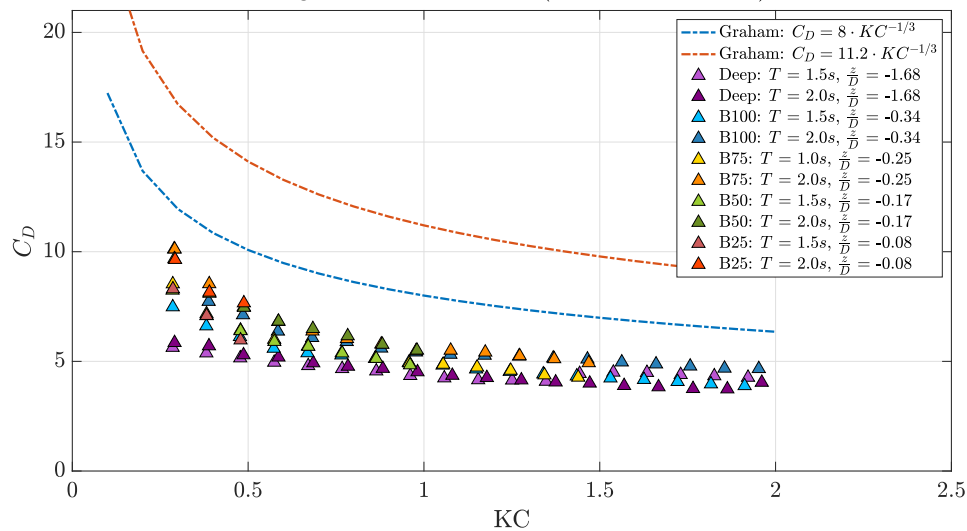


Figure 5.13: Drag coefficients vs. KC for C28 ($r = 0.280$) for all submergences and periods. Results are plotted against the suggested curves by Graham, 1980 [7].

The drag coefficients for both models are briefly presented in Figures 5.12 and 5.13. As discussed in Section 2.4, these drag coefficients are calculated under the assumption that the damping force is purely quadratic in nature. This means neglecting the linear damping component, i.e. $B_{33}^{(1)} = 0$. The drag coefficients follow a typical curve with larger values at low KC numbers and a converging trend as the amplitude of motion increases. Similar to the damping coefficients, the drag coefficients increase with decreased submergence and are dependent on the oscillation amplitude. Drag coefficients at low KC numbers can be roughly two times larger or more for C19, but the data for both models seem to converge towards similar values as the KC number increases.

The experimental drag coefficients are also plotted against the suggested values by Graham, 1980 [7]. As discussed in Section 1.3, Graham studied the forces induced on plates by flow separation and vortex shedding at low KC numbers. Through his study, he concluded that the drag coefficients for a flat plate in oscillatory flow are proportional to $KC^{-1/3}$. Graham suggested a theoretical value for α (introduced in Equation 1.3) of 11.2, as well as an experimental value of 8.0 based on experiments by Singh, 1979 [20]. Comparing the experimental results to the values by Graham, it is seen that results for C28 lie on the lower side of both curves. This is reasonable, as the suggestions by Graham are for a solid plate. For deep water oscillations, results for C28 are approximately half the value of $C_D = 8KC^{-1/3}$, but the differences decrease for larger KC numbers. The results for C19 are more interesting, where the experimental drag coefficients lie between the curves suggested by Graham. The coefficients for deep water are, in fact, nearly identical to the curve for $\alpha = 8$. The correspondence between these results suggests that approximated formulas for solid plates can, in certain cases, give accurate estimates of the hydrodynamic loads on perforated models. The similarities also suggest that as the perforation ratio decreases, the effects of the perforations are less important to the overall loads on the structures. Mentzoni [13] and Sandvik et al. [18] illustrated the importance of plate end flow separation on the hydrodynamic coefficients, in particular at high KC numbers. These results suggest that, despite local flow separation at the plate openings, global vortices at the model ends are most dominant for lower perforations. This will be discussed in greater detail throughout this chapter.

5.1.4 Effect of Porosity on Hydrodynamic Coefficients

Figures 5.14 and 5.15 present the dimensional added mass and damping force coefficients for all models, oscillation periods, and submergences. The aim is to illustrate how the hydrodynamic coefficients vary with the perforation ratio (r). The curves for both models follow the same trends, which serves as a further validation of the experimental results. Added mass coefficients show a clear decreasing trend with decreased distance to the free surface for both models, while damping coefficients show a constant increase with increasing amplitude for all values of z/D . Convergence towards zero for small KC numbers is also observed for both models.

The resulting plots show that the hydrodynamic forces are larger for C19 (with $r = 0.189$) than C28 (with $r = 0.280$) at all submergences and periods. Increased forces and hydrodynamic coefficients for structures with smaller perforation ratios is supported by findings in the previous and recent studies presented in Section 1.4 [2, 8, 13, 18]. For the case of deep water oscillations ($z/D = -1.68$), added mass coefficients are approximately 2.2 times larger for C19 for both periods. For the three next submergences ($z/D = -0.34, -0.25$ and -0.17) the added mass coefficients can be anywhere from 4 to 8 times larger for C19 depending on the oscillation period. The largest differences occur for $T = 2.0s$.

There is less difference in added mass for the smallest submergence, because both models exhibit very small and highly negative added mass coefficients. The damping coefficients are approximately 1.6 - 2.0 times larger for C19 for all periods and submergences.

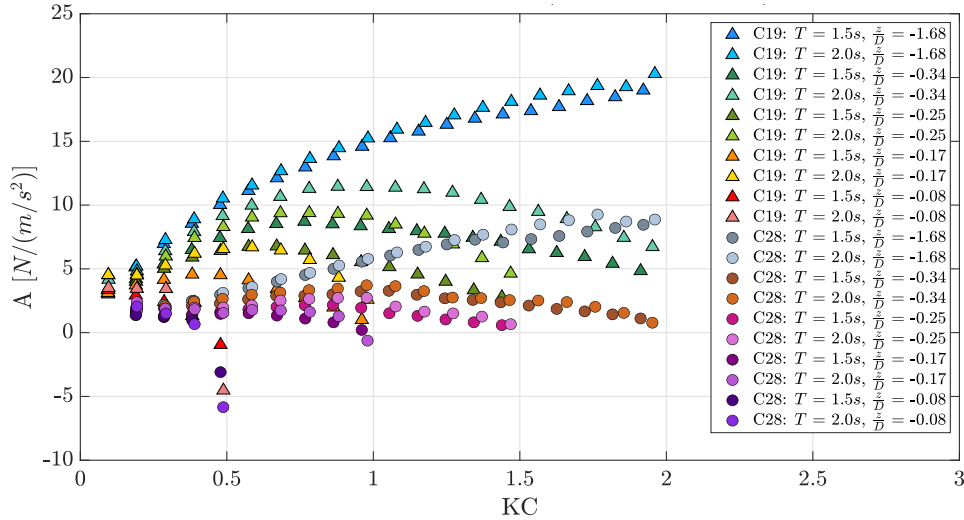


Figure 5.14: Dimensional added mass coefficients for C19 ($r = 0.189$) and C28 ($r = 0.280$) at $T = 1.5s$ and $T = 2.0s$ at all submergences.

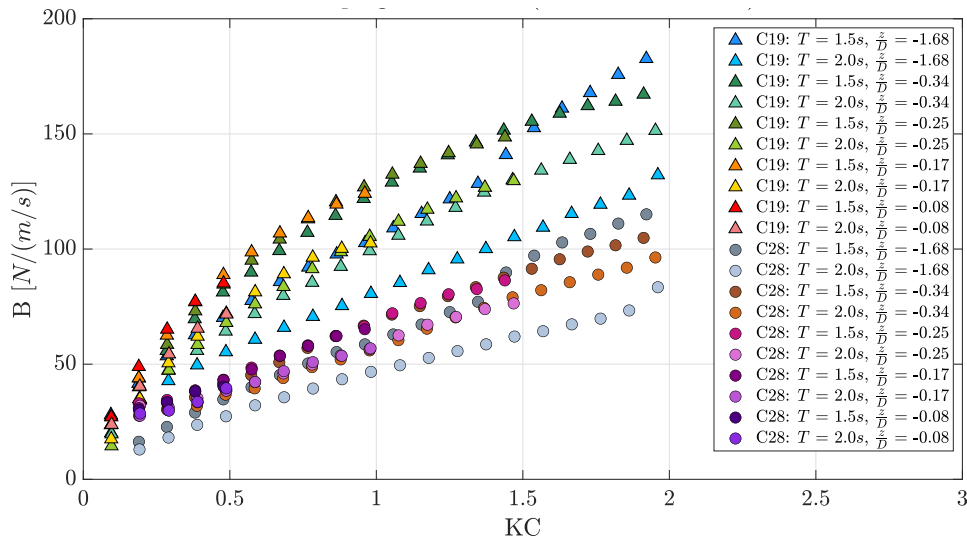


Figure 5.15: Dimensional damping coefficients for C19 ($r = 0.189$) and C28 ($r = 0.280$) at $T = 1.5s$ and $T = 2.0s$ at all submergences.

Larger forces for lower perforations can be explained by two main phenomena - the blockage effect and edge effects. The term blockage effect essentially implies that the fluid is blocked from flowing through the slits in the model, causing a build up of pressure on the lower side of the plate. Large static pressure differences across the plate give rise to larger hydrodynamic forces and cause the water to move through the slits at higher speeds. C19 has a lower perforation ratio and thus a higher blockage effect. This gives rise to more local vortical structures at the openings (because the flow is less able to flow straight through the slits in the model) and regions of higher pressure, which contribute to an increase in

the overall force on the model. The most prominent reason for differing forces between perforations is most likely a larger presence of vortical structures at the plate ends for structures with smaller perforation ratios. Mentzoni, 2019 [13] used a two-dimensional numerical viscous flow solver to visualize and observe the features of the flow field around three perforated models with perforation ratios $r = 0, 0.20$, and 0.40 . Results showed that the flow was globally deflected towards the sides of the plates for all tested configurations, but that vortices due to plate end separation were more prominent for lower perforations.

Figures 5.16 and 5.17 show the added mass to damping ratio for both models. These are presented to visualize the difference in magnitude for both force components. As previously stated, damping dominance is observed at all submergences and oscillation periods for both models. These figures further illustrate that damping dominance is largest for C28, i.e. damping dominance increases for larger perforation ratios. This is consistent with previous studies on perforated/ventilated models [2, 13, 18]. Results also show that damping dominance increases with decreasing submergence, which is in line with the decreasing trends observed for the added mass coefficients with increased proximity to the free surface.

It is clear that damping forces are dominant for all perforation ratios, oscillation periods, and submergences. The importance of this can be emphasized by looking back at the equation for the normalized force, presented in Section 2.4. The force amplitude is proportional to the square root of the non-dimensional added mass and damping coefficients squared. This means that if the damping component is highly dominant, it will account for a large percentage of the total hydrodynamic force acting on the structure. As discussed in Section 1.5, DNV-GL's recommended practice [5] only provides a method for estimating the added mass of perforated structures. Limited information is given on how to account for the perforation ratio when estimating the damping coefficients. If results show that damping is highly dominant for ventilated structures, and more so for increased porosity, then this lack of information reflects an underlying need for increased knowledge on the importance of damping loads on subsea modules and templates.

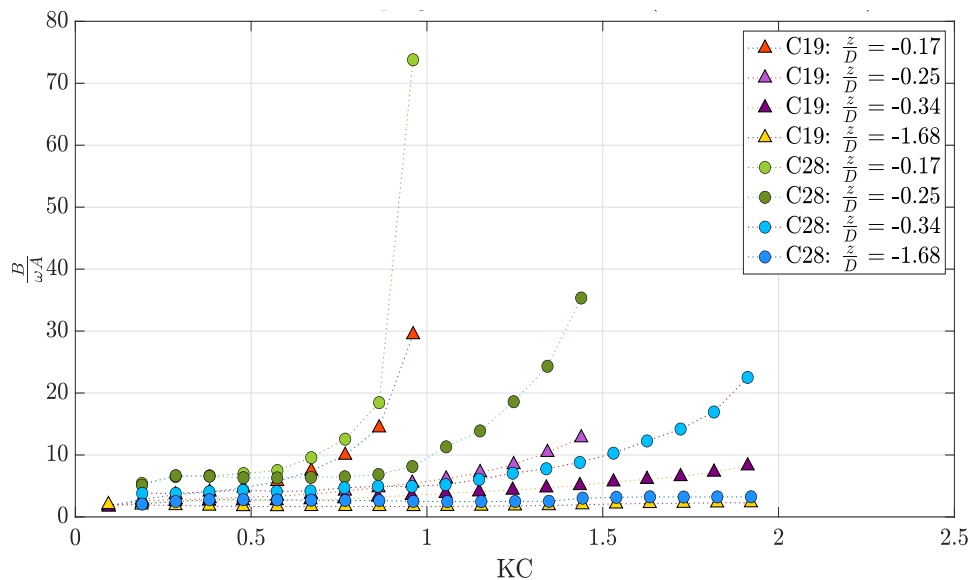


Figure 5.16: Added mass to damping ratio for C19 ($r = 0.189$) and C28 ($r = 0.280$) at all submergences, with oscillation period $T = 1.5s$.

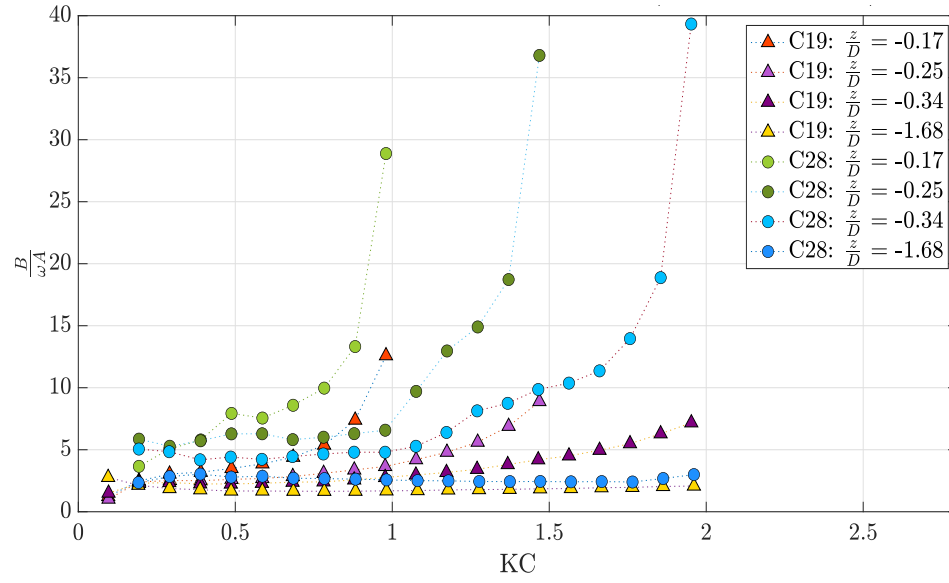


Figure 5.17: Added mass to damping ratio for C19 ($r = 0.189$) and C28 ($r = 0.280$) at all submergences, with oscillation period $T = 2.0s$.

5.2 Wave Tests

The results presented in this section serve the same purpose as the previous section regarding forced oscillation tests. Once again, results for the wave tests will be presented separately to convey an understanding of how the hydrodynamic coefficients and overall forces are affected by submergence and porosity.

5.2.1 Force Time Series

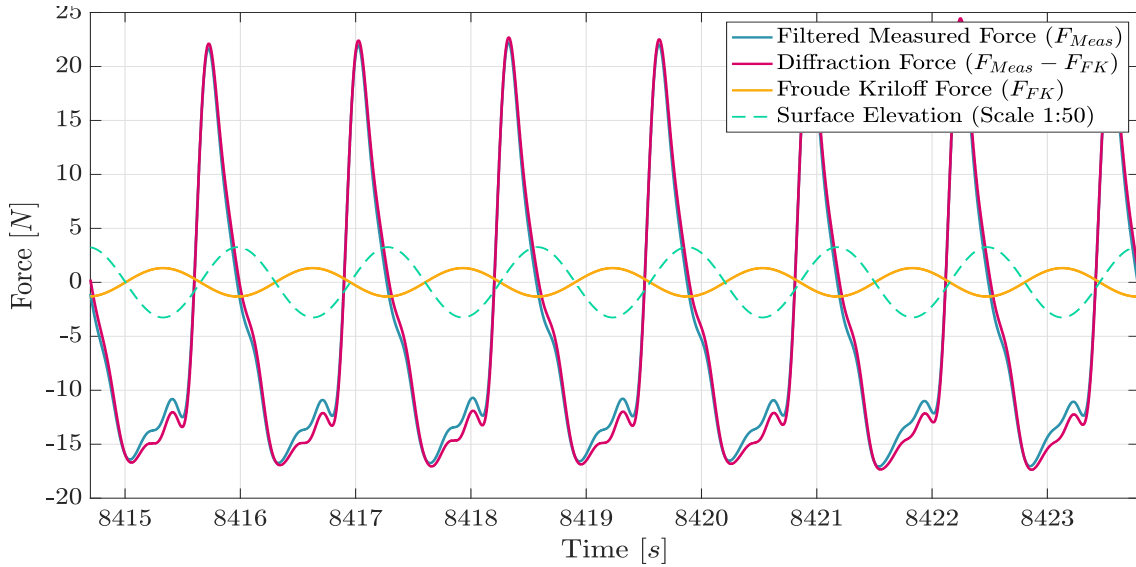


Figure 5.18: Force time series for C28 ($r = 0.280$) with seven full-amplitude wave cycles. Results are for $z = -2.5\text{cm}$, $\lambda/D = 8.89$ and $\lambda/H = 20$.

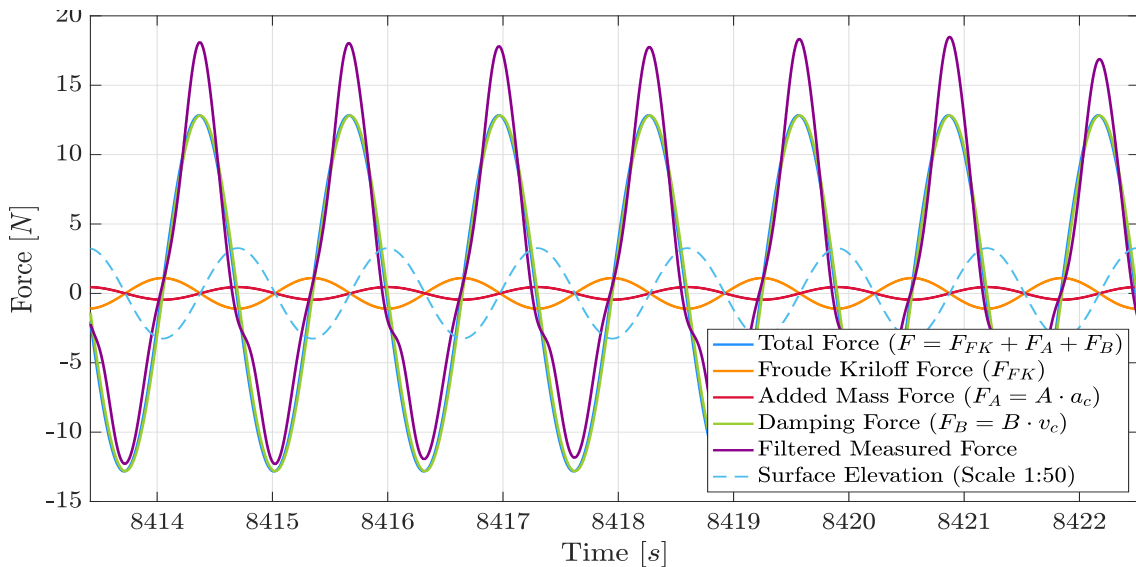


Figure 5.19: Force time series for C28 ($r = 0.280$) with seven full-amplitude wave cycles. Results are for $z = -10\text{cm}$, $\lambda/D = 8.89$ and $\lambda/H = 20$.

Figures 5.18 and 5.19 illustrate two force time series for C28 ($r = 0.280$) for the steepest and longest waves. A total of seven full-amplitude wave cycles have been extracted to show the steady state forces acting on the model when it is fixed and subjected to incoming regular waves. The aim is to indicate how the forces vary with submergence, and to briefly highlight the difficulties in accurately predicting the hydrodynamic loads on structures present in the wave zone. Figure 5.18 depicts forces at $z = -2.5\text{cm}$, where the models are partly in and out of waves for all runs. Figure 5.19 depicts forces at $z = -10\text{cm}$, where the models are fully submerged for all wave periods and steepness. Additional force time series for C19 and C28 for the largest wave period ($T = 1.3\text{s}$, $\lambda/D = 8.89$) at varying submergence and steepness are presented in Appendices C.1 and C.2.

Both force time series show the measured force, which has been filtered to include higher order harmonics as described in Section 4.2. The Froude Kriloff force is calculated by use of the vertical wave particle acceleration at each rod center of the model, and is 180° out of phase with the surface elevation. The resulting diffraction force is found by subtracting the Froude Kriloff force from the measured force. When the models are fully submerged, this diffraction force can be decomposed into added mass and damping components (as seen in Figure 5.19). It is important to note that for the case of waves, it is somewhat inaccurate to refer to these forces as added mass and damping forces - they are force components proportional to the acceleration and velocity of the fluid particles in the wave. For simplicity sake, however, we refer to them as added mass and damping forces throughout this thesis. When the model is in and out of water, however, this decomposition will not give valid coefficients by use of the Fourier averaging technique. This due to the presence of higher order nonlinear effects, which can largely affect the overall forces on the body. According to the recommended practice by DNV-GL [5], the force should then be modeled as a complex water-entry force to include slamming and buoyancy components. Figure 5.18 for $z = -2.5\text{cm}$ illustrates the differences in the measured force when the model is in and out of water, as opposed to when the model is fully submerged. Results show that the measured force is larger than the forces for other submergences with corresponding wave steepness and period, with steep peaks that indicate slamming loads as the model is entering the water. The model is dry when the wave elevation is at its minimum, where water entry and loss of buoyancy give rise to negative forces. The slamming phenomenon is not in the scope of this thesis, thus it will not be discussed in further detail. The results for $z = -2.5\text{cm}$ will only be presented as force times series, and included in the Appendix. This serves as an important reminder on how the hydrodynamic loads change and increase in complexity when structures are directly present in the wave zone.

The results for $z = -10\text{cm}$ (depicted in Figure 5.19) show trends that are representative for the two other submergences where the models are fully submerged. The added mass and Froude Kriloff forces are small, and 180° out of phase with each other. For some waves the added mass is negative, resulting in an added mass curve that is in phase with the Froude Kriloff force. As a result, the diffraction force is nearly equal to the measured force and the damping force is nearly in phase with the diffraction force. This shows a clear damping dominance, which will be discussed later. The total force is re-calculated through summation of the Froude Kriloff, added mass, and damping components. Unlike forced oscillations, this first order force does not accurately predict the measured forces on the model. In addition to larger peaks, the measured force also lacks symmetry. When plotted against the measured force filtered around the harmonic frequency only, however, they are identical. This shows that, for the case of fully submerged wave tests, the added mass and damping components can be used to predict the first order loads on structures in waves.

5.2.2 Effect of Submergence and Porosity on Hydrodynamic Coefficients

Hydrodynamic coefficients are calculated for submergences $z = -5, -7.5, \text{ and } -10\text{cm}$ for wave periods ranging from $T = 0.9 - 1.3\text{s}$. As discussed in Section 4.2, these coefficients are found under the assumption that the body is fully submerged and that wave particle velocity and acceleration are constant over the model (i.e. long wave approximation). For the case of a vertical cylinder of diameter D subjected to incident regular waves of length λ , this long wave approximation is valid for $\lambda/D > 5$. For the present case with several horizontal cylinders, no such validity range can be expressed with certainty.

Added Mass Coefficients:

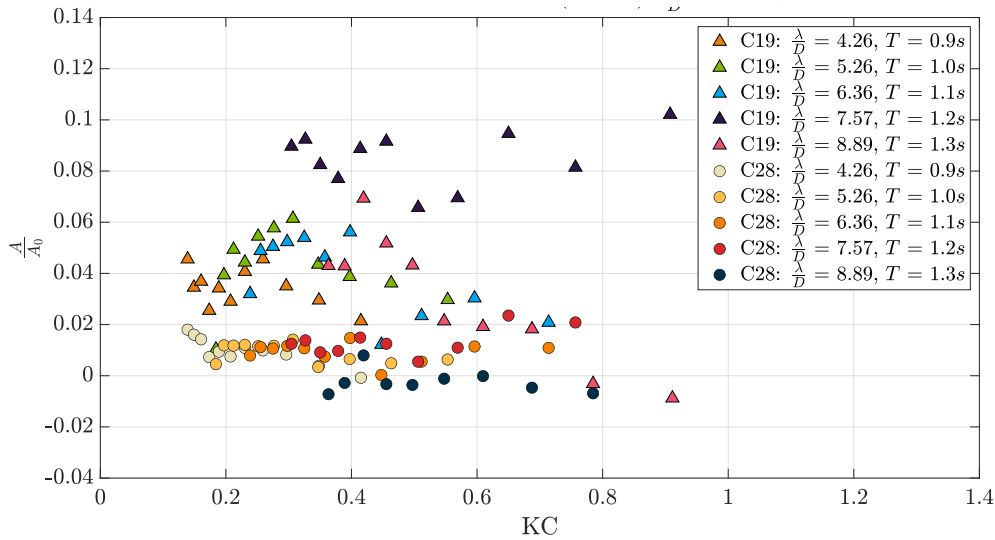


Figure 5.20: Non-dimensional added mass coefficients vs. KC for C19 ($r = 0.189$) and C28 ($r = 0.280$) at $z = -10\text{cm}$ for all wave periods and steepness.

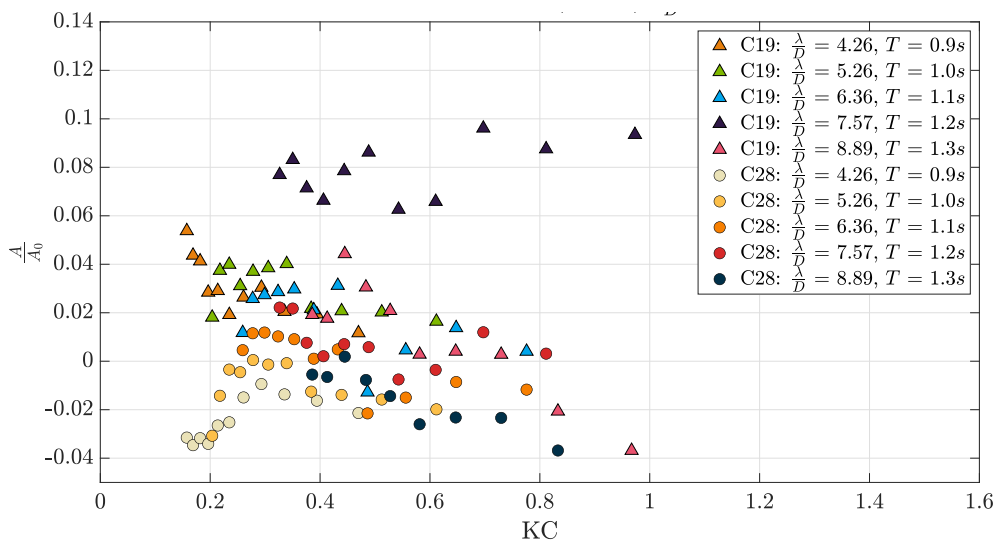


Figure 5.21: Non-dimensional added mass coefficients vs. KC for C19 ($r = 0.189$) and C28 ($r = 0.280$) at $z = -7.5\text{cm}$ for all wave periods and steepness.

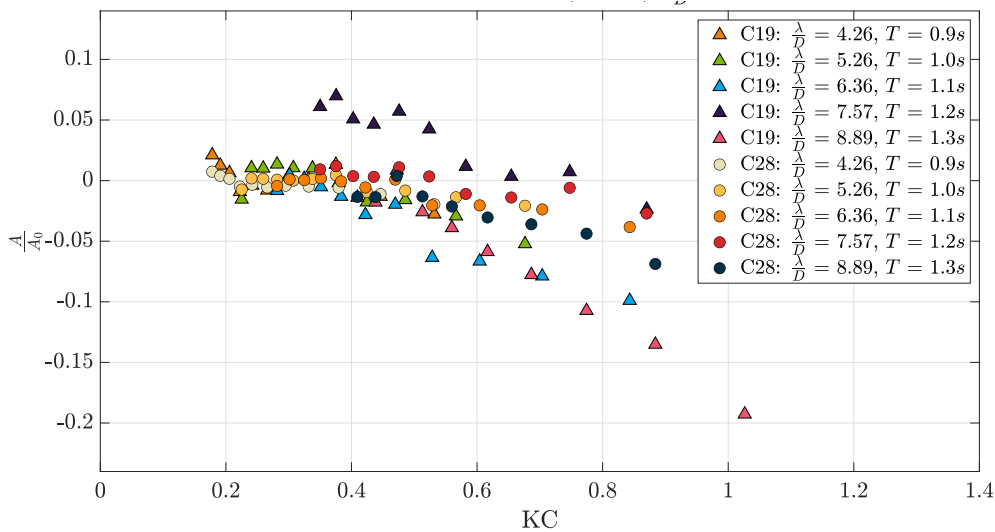


Figure 5.22: Non-dimensional added mass coefficients vs. KC for C19 ($r = 0.189$) and C28 ($r = 0.280$) at $z = -5\text{cm}$ for all wave periods and steepness.

Non-dimensionalized added mass coefficients for C19 and C28 at all submergences and wave periods are presented in Figures 5.20 to 5.22. As was observed in the force time series presented in the previous subsection, the added mass contribution to the overall hydrodynamic force is small. This is also reflected in the current plots. Significantly small added mass coefficients were also observed by Gupta, 2018 [8], who performed wave tests on C19 at a submergence of 55cm below the mean water level. The current data shows large scatter for $z = -7.5\text{cm}$ and $z = -10\text{cm}$, making the results difficult to interpret. This scatter is most prominent for C19, where data at $T = 1.2\text{s}$ is somewhat divergent from the rest. The reason for this is unknown. It can be noted that the added mass coefficients are larger for C19, which has the lowest porosity.

It is interesting to see that only the data at $z = -5\text{cm}$ provides any real trends for the added mass coefficients, without the presence of too much scatter. Neglecting the results at $T = 1.2\text{s}$ for C19, the data for both models are also quite similar despite differences in porosity. Both models show a clear decreasing trend for this submergence, where most coefficients are negative. Negative added mass is observed for all submergences, and the occurrence seems to decrease with increased distance to the free surface. Mciver & Evans, 1984 [10] studied the occurrence of negative added mass for submerged oscillating bodies. They showed that free surface effects were an important factor in the occurrence of negative added mass, and that rapid changes in added mass and damping at small submergences could be explained in terms of near-resonant standing waves. Free surface effects seem like a reasonable explanation for these experimental results, because as the figures show, the occurrence of negative added mass is most prominent for the smallest submergence.

Figure 5.23 presents the added mass to damping ratio for C19 and C28 for wave periods $T = 1.0 - 1.3\text{s}$ at all three submergences. Due to the large spread in data points, the y axis showing the relative magnitude is plotted in the logarithmic scale. This plot further illustrates the significant difference in magnitude between the added mass and damping coefficients, which are yet to be presented. There is a clear damping dominance in waves for all perforations, submergences, and wave periods. This damping dominance is even more prominent than results for forced oscillations in otherwise still water. The data points are

once again difficult to interpret due to the wide spread in data, but it seems that damping dominance is largest for C28. Similar to the case of forced oscillations, this means that damping dominance increases with perforation ratio. This is once again supported by previous studies, and most likely due to differences in the flow field around the body for varying porosity and differing interactions between the models and the surrounding fluid. These results once again emphasize the importance of accurate estimates of the damping loads, as these are even more dominant for structures subjected to incoming regular waves.

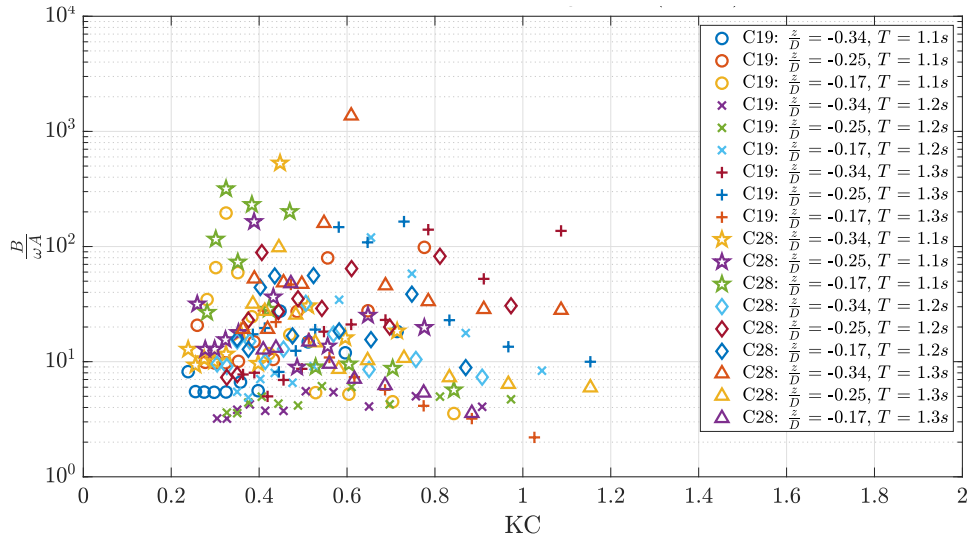


Figure 5.23: Magnitude of the added mass to damping ratio vs. KC for C19 ($r = 0.189$) and C28 ($r = 0.280$) at all submergences for wave periods $T = 1.1 - 1.3s$.

Damping Coefficients:

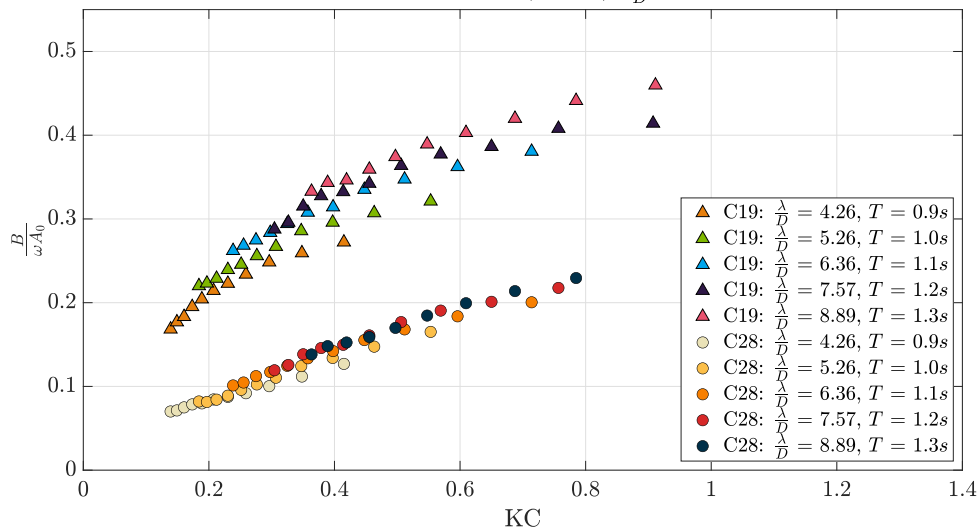


Figure 5.24: Non-dimensional damping coefficients vs. KC for C19 ($r = 0.189$) and C28 ($r = 0.280$) at $z = -5cm$ for all wave periods and steepness.

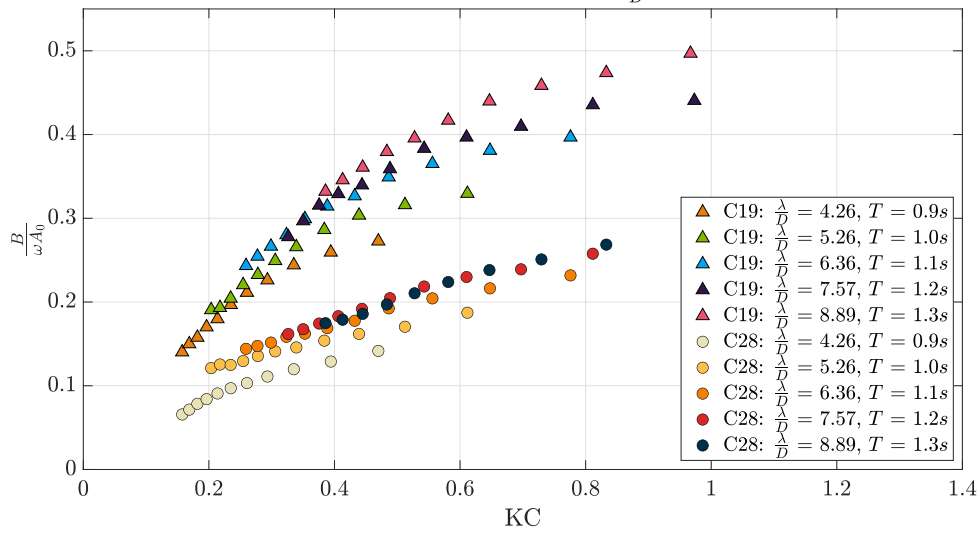


Figure 5.25: Non-dimensional damping coefficients vs. KC for C19 ($r = 0.189$) and C28 ($r = 0.280$) at $z = -5cm$ for all wave periods and steepness.

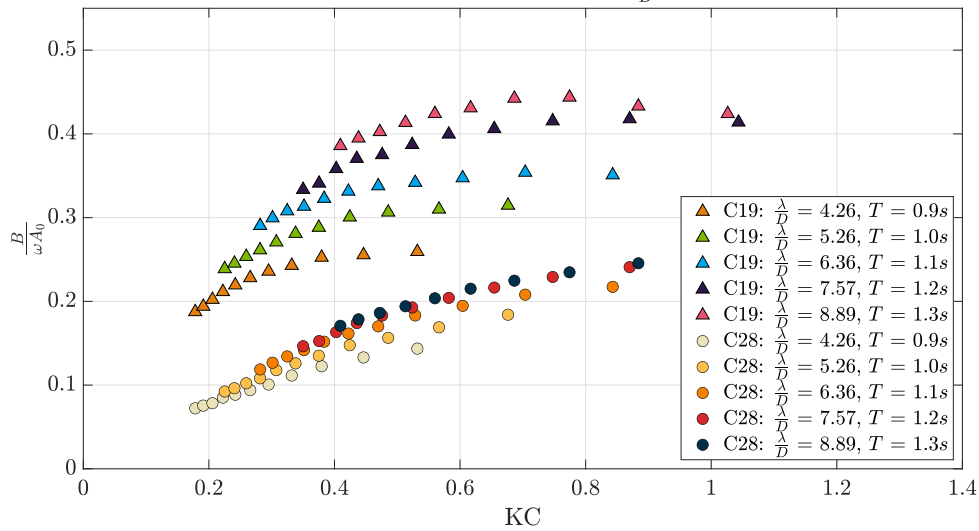


Figure 5.26: Non-dimensional damping coefficients vs. KC for C19 ($r = 0.189$) and C28 ($r = 0.280$) at $z = -5cm$ for all wave periods and steepness.

Figures 5.24 to 5.26 show the non-dimensionalized damping coefficients for C19 and C28 at all submergences and wave periods. As already mentioned and illustrated in Figure 5.23, there is a clear damping dominance for both models at all values of z , wave period, and steepness. As opposed to the added mass coefficients, the non-dimensional damping coefficients follow a steadily increasing curve for increasing values of KC . A clear amplitude dependence is therefore observed. Damping is larger for C19 than C28, i.e. for the model with the lowest perforation ratio. Damping coefficients for C19 are approximately 2 times larger than most corresponding values for C28. As discussed for the case of forced oscillations, this is most likely due to differences in flow separation around the models. Mentzoni, 2019 [13] showed through numerical simulations and visualizations of the resulting flow fields that forces were larger for models with lower perforation ratios. He suggested that

this was due to larger global vortices at the model ends and a higher blockage effect for the models with lowest perforation.

Largest damping is observed for the highest wave period ($T = 1.3s$) at all submergences for both models, and the smallest damping is observed for the lowest wave period ($T = 0.9s$). It is evident that the period dependence increases with decreased submergence, as is to be expected closer to the free surface. This period dependence is especially evident for C19 (similar to what was observed for forced oscillations), which is once again possibly due to the larger presence of flow separation and plate end vortex formation for lower perforation ratios. It can also be due to the simple fact that the models interact differently with the surrounding fluid and the free surface. Period dependence is most clear for $z = -5cm$, which also illustrates the somewhat striking differences between the data points for C19 and C28. The damping for C19 at this submergence also seems to decrease for larger values of KC, but this trend is not present for C28. This decrease could imply that there are higher order effects that become increasingly important for the largest waves at the lowest submergences (i.e. when the model is nearly in and out of water). For lower values of KC, the results show that the magnitude of the damping coefficients is larger at the smallest submergence ($z = -5cm$). For the other two submergences, the results are quite similar.

Drag Coefficients:

Figures 5.27 to 5.29 show the drag coefficients in waves for C19 and C28. As discussed in the previous section on harmonically forced oscillations, these coefficients are calculated under the assumption that the damping force is purely quadratic in nature. The experimental data are once again plotted against the suggested curves by Graham, 1980 [7] for a solid plate in oscillatory flow. In agreement with the previous results, the drag coefficients for C19 are larger than the coefficients for C28 at all submergences. As the KC number decreases, these differences become smaller. This is most evident for the lowest submergences. At the lowest values of KC, the drag forces can be 2 - 3 times larger for C19 depending on the wave period. Once again, more period dependency is noted for C19. This period dependence increases with decreased proximity to the free surface.

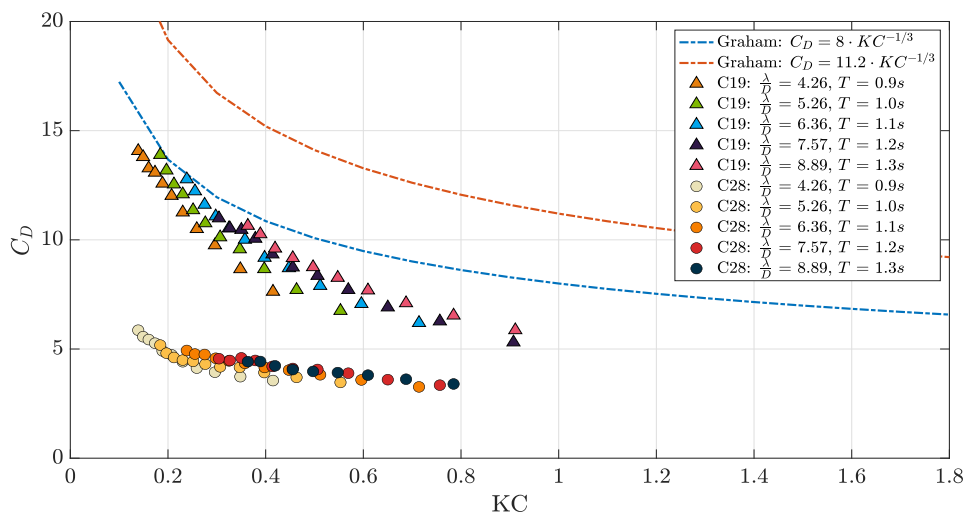


Figure 5.27: Drag coefficients in waves vs. KC for C19 ($r = 0.189$) and C28 ($r = 0.280$) for $z = -10cm$. Results are plotted against the suggested curves by Graham, 1980 [7].

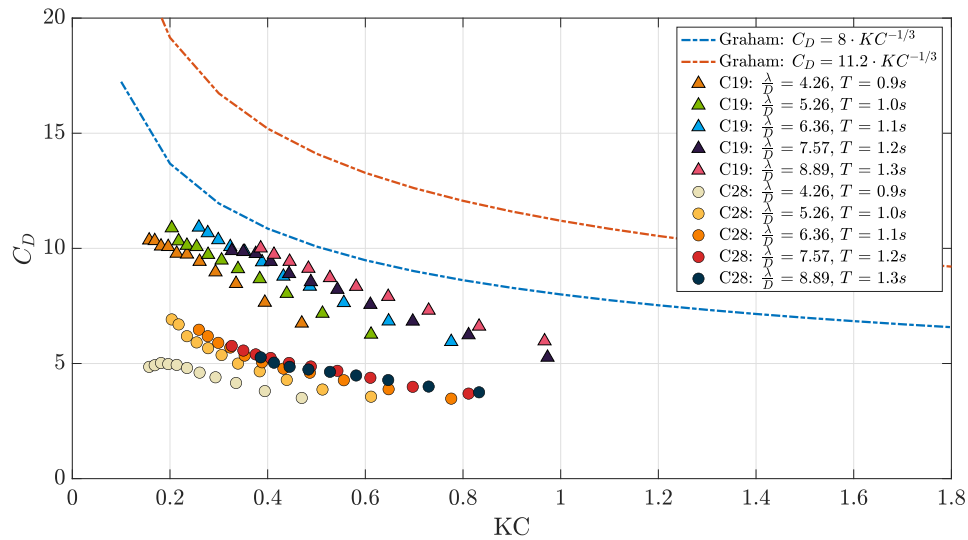


Figure 5.28: Drag coefficients in waves vs. KC for C19 ($r = 0.189$) and C28 ($r = 0.280$) for $z = -7.5cm$. Results are plotted against the suggested curves by Graham, 1980 [7].

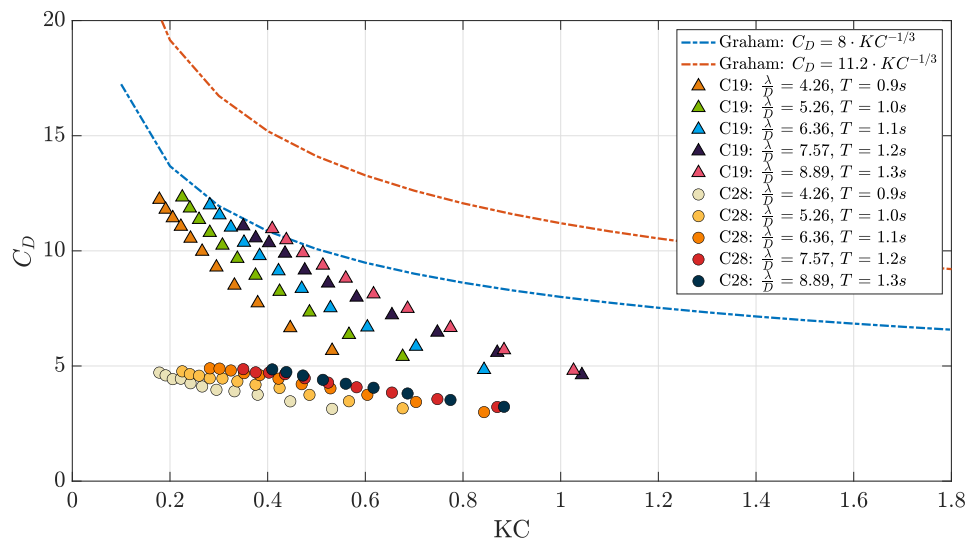


Figure 5.29: Drag coefficients in waves vs. KC for C19 ($r = 0.189$) and C28 ($r = 0.280$) for $z = -5cm$. Results are plotted against the suggested curves by Graham, 1980 [7].

Some similarities are noted between the experimental results and the suggested values by Graham for C19 at the lowest KC numbers. Both curves are clearly conservative compared to the results for C28, but this was also observed for forced oscillation tests. It is yet again important to emphasize that Graham's results are based on solid plates in infinite fluid, thus the observed differences seem within reason. Results suggest that the lower curve ($C_D = 8KC^{-1/3}$) could be used to give sufficient, yet somewhat conservative, estimates for the drag coefficients on perforated models with lower perforation ratios in waves.

5.2.3 Normalized Force and Comparison with Wave Tests by Fredrik Mentzoni

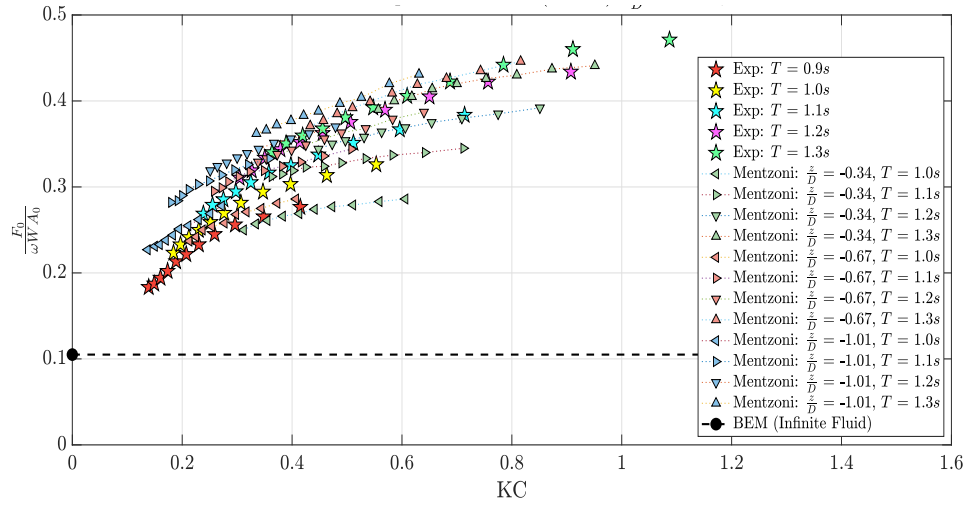


Figure 5.30: Normalized force amplitude for C19 at $z = -10\text{cm}$ ($z/D = -0.34$) for all four wave periods. Values are plotted against results by Mentzoni, 2020 [14] for C19 for wave periods $T = 1.0 - 1.3\text{s}$ at submergences $z = -10, -20,$ and -30cm .

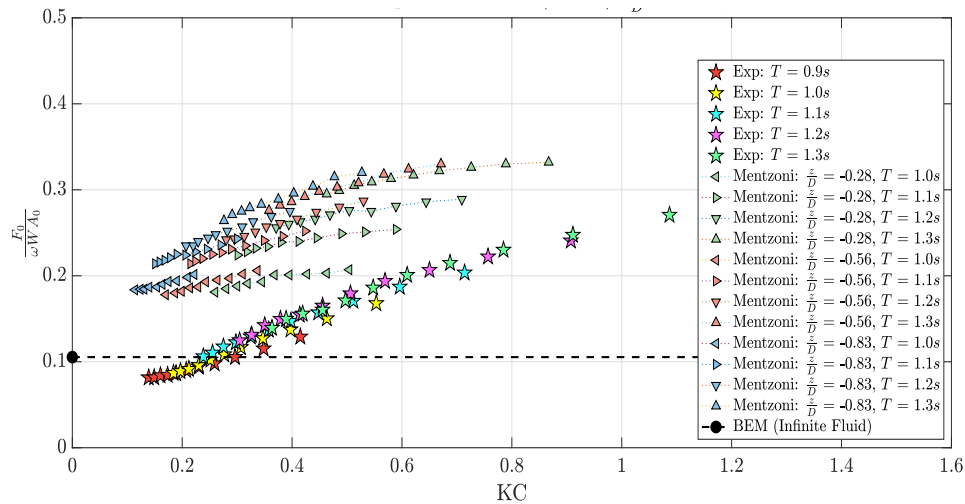


Figure 5.31: Normalized force amplitude for C28 at $z = -10\text{cm}$ ($z/D = -0.34$) for all four wave periods. Values are plotted against results by Mentzoni, 2020 [14] for S28 for wave periods $T = 1.0 - 1.3\text{s}$ at submergences $z = -10, -20,$ and -30cm .

We also present values for the normalized force, as described in Section 2.4. This is defined as the square root of the non-dimensionalized added mass and damping coefficients squared. For the case of waves, the Froude Kriloff contribution is also included. These values are compared to those calculated by Mentzoni, 2020 [14] for an overall validation of the experimental results. Mentzoni performed wave tests at $z = -10, -20$ and -30cm submergence with models C19 and S28. The latter is a square cylinder model with the same perforation ratio as C28, i.e. $r = 0.280$. Figures 5.30 and 5.31 depict the experimental normalized force values for C19 and C28 for $z = -10\text{cm}$ plotted against the experimental values by Mentzoni.

Results by Mentzoni show a higher normalized force for C19 than S28 for a given KC number, i.e. higher forces for lower perforation ratios. The same is observed in current experiments, where the normalized force is approximately twice the size for C19 than corresponding data points for C28. This once again emphasizes the fact that lower perforation ratios give rise to larger hydrodynamic loads, most likely as a result of differing flow patterns around the models and blockage effects. The results for C19 show good agreement with results by Mentzoni, but results for C28 lie on the lower side. This could be considered reasonable due to differences in cylinder geometry, which seems to be of more importance for larger perforations. It is somewhat peculiar, however, that the results for C28 show significantly less period dependence than the results for S28 by Mentzoni, but the reasons for this are difficult to properly identify. Mentzoni also found that the normalized force depends on both the wave period and submergence. This is reflected in the results for C19, but data points for C28 show significantly less dependence on the wave period. Mentzoni also uses the Boundary Element Method (BEM) and a potential flow solver to give limiting values for $KC \rightarrow 0$ in infinite fluid. These values are 0.1050 and 0.1054 for C19 and S28 respectively. For C19 this value fits the current experimental results very well, giving increased confidence in the experiments. The value is too high for C28, but this is to be expected due to differences in cylinder shape.

5.3 Comparison of Forced Oscillations and Waves

The final goal of this thesis is to compare the hydrodynamic loads on perforated models subjected to incoming regular waves and forced to harmonically oscillate in otherwise still fluid. Forced oscillation trials are a common method of finding the hydrodynamic loads and coefficients for structures in oscillatory flow, thus it is important to investigate how these values compare to the forces on fixed structures in waves. The aim of this section is therefore to quantify and visualize these differences, as well as provide a basic understanding as to why they occur. We compare data at submergences $z = -5, -7.5$ and -10cm where the models are fully submerged for all tested KC numbers. To be able to explain any observed differences, this section will delve deeper into the findings of a recent publication by Fredrik Mentzoni, who has utilized numerical tools to study the flow around perforated models in oscillations and waves. This section is therefore a combination of previous work and the findings of the current experiments.

5.3.1 Added Mass and Damping Coefficients

The previous sections in this chapter have studied forced oscillations and waves separately, where the main focus has been on the added mass and damping coefficients and how these vary with porosity and submergence. For both cases, one of the most important observations is a significant damping dominance for both models. This damping dominance is largest for models with higher perforation ratios, but the overall hydrodynamic forces increase with decreased perforation. It has also been illustrated that the added mass coefficients decrease significantly with increased proximity to the free surface in both oscillations and waves, with highly negative values observed for the smallest submergence. For the case of forced oscillations, the added mass coefficients (although small) follow distinct curves where they increase to a maximum at a specific KC number, followed by a decrease towards zero and negative values as the amplitude of motion increases. This excludes the results for deep water oscillations. For the case of waves, however, there is large scatter in the data.

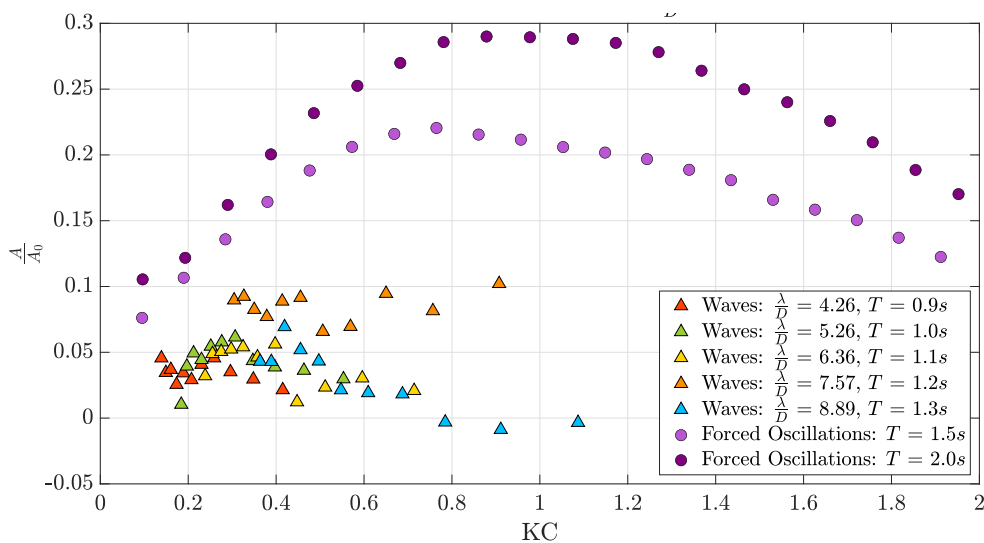


Figure 5.32: Comparison of non-dimensional added mass coefficients in forced oscillations and waves. Results are for C19 ($r = 0.189$) at $z = -10\text{cm}$.

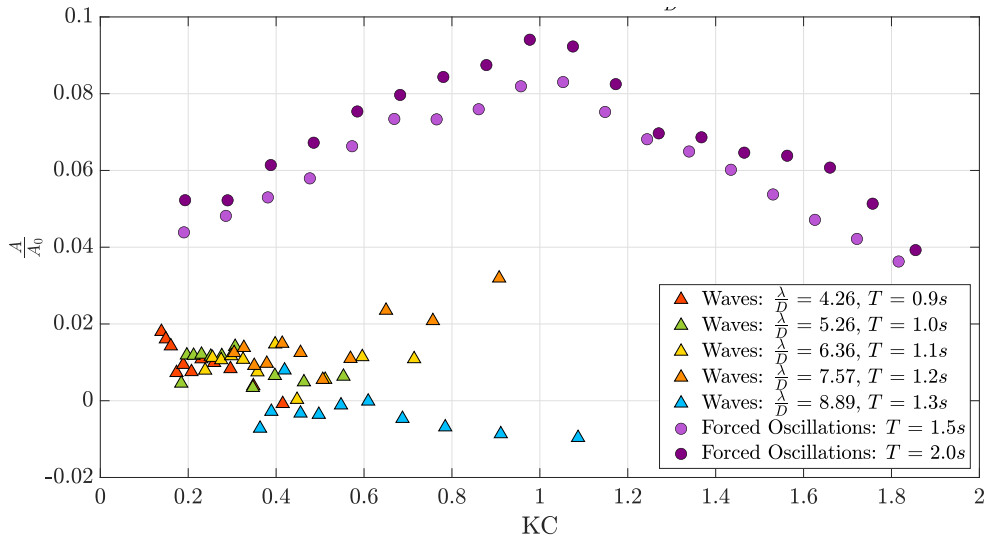


Figure 5.33: Comparison of non-dimensional added mass coefficients in forced oscillations and waves. Results are for C28 ($r = 0.280$) at $z = -10cm$.

Figures 5.32 and 5.33 show the added mass coefficients for C19 and C28 at a submergence of $z = -10cm$. Although both test cases have small added mass coefficients in comparison to the damping force contribution, there is a significant difference in the results between waves and forced oscillations. As previously mentioned, one of the first things one notices is the difference in the behavior of the coefficients. For forced oscillations, a clear trend is observed in the data. For both models the coefficients increase to a maximum value at $KC \approx 1$, and continue to decrease towards zero as the KC number increases. Some period dependence is noted, which is more apparent for C19. In waves, the data points are more scattered and difficult to interpret. The difference in magnitude is also important to note. Depending on the wave period, the coefficients for forced oscillations can be up to 10 times larger or more than the coefficients for wave tests. Gupta, 2018 [8] observed that added mass coefficients in waves were approximately one-tenth of the value for forced oscillations in deep water, thus it can be assumed that these differences are within reason.

Figures 5.34 and 5.35 show the corresponding damping coefficients for C19 and C28 at the same submergence. Results for deep water oscillations and the wave radiation damping coefficients (which have also been non-dimensionalized) are also included for reference. Unlike the added mass coefficients, the damping coefficients show the same trends for forced oscillations and waves. There is a clear increase with increasing KC , showing that the coefficients are amplitude dependent for both cases. One can note a clear similarity between the damping coefficients at low KC numbers. The coefficients converge towards zero as the KC number becomes increasingly small, both for waves and oscillations. For C19, the coefficients in waves and oscillations converge together at $KC \approx 0.2$. For C28 there is less similarity between the damping coefficients for the same submergence, as data values for forced oscillations at $z = -10cm$ do not converge towards zero in the same manner as the results for C19. However, the damping coefficients in waves converge towards the coefficients for deep water oscillations at low KC values. This lack of similarity will be discussed in the final section of this chapter regarding experimental errors. One can also note that both cases show minimal period dependence. Furthermore, there is little similarity between the wave radiation damping and the damping in waves.

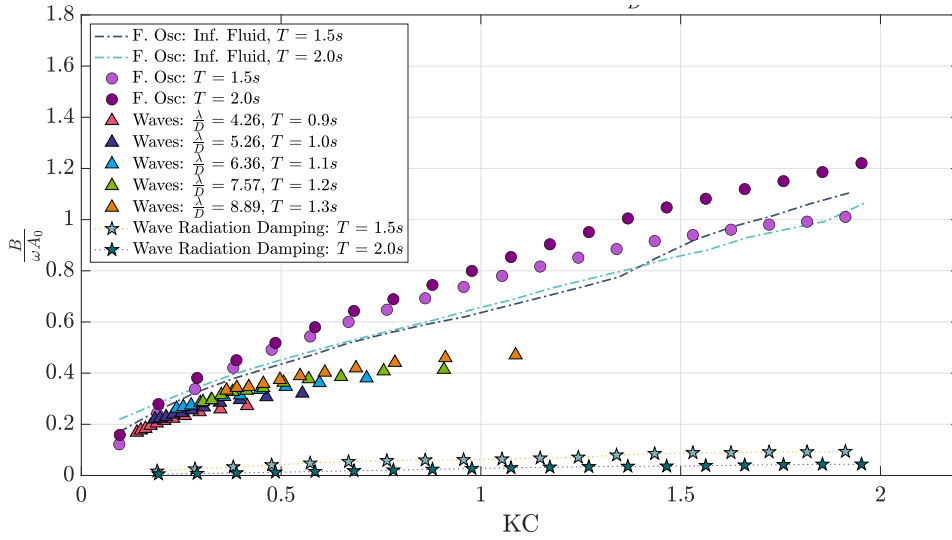


Figure 5.34: Comparison of non-dimensional damping coefficients in forced oscillations and waves. Results are for C19 ($r = 0.189$) at $z = -10\text{cm}$. Results for deep water oscillations ($z = -50\text{cm}$) and wave radiation damping are also included.

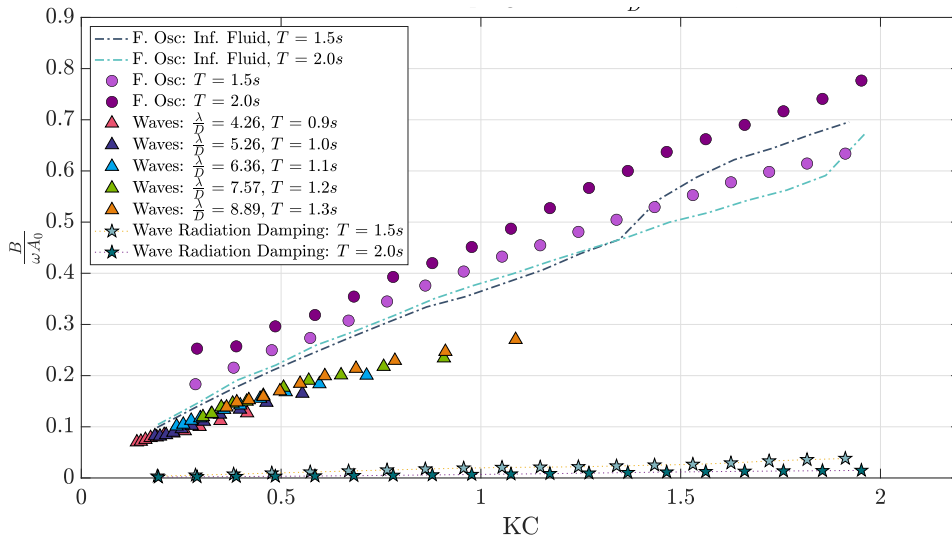


Figure 5.35: Comparison of non-dimensional damping coefficients in forced oscillations and waves. Results are for C28 ($r = 0.280$) at $z = -10\text{cm}$. Results for deep water oscillations ($z = -50\text{cm}$) and wave radiation damping are also included.

This section has only presented a comparison of coefficients for one submergence, but the remaining results for added mass and damping coefficients for C19 and C28 are included in Appendices A.1 to A.4. Due to the large damping dominance observed in forced oscillations and waves, it seems more fitting to continue this comparison by investigating the normalized force. The added mass coefficients are difficult to compare due to the scatter observed for waves, and in cases where the added mass is very small it is most productive to study the overall hydrodynamic loads acting on the models. The normalized force is calculated as presented in Section 2.4, and will be discussed in the following subsection.

5.3.2 Normalized Force and the Importance of Flow Separation

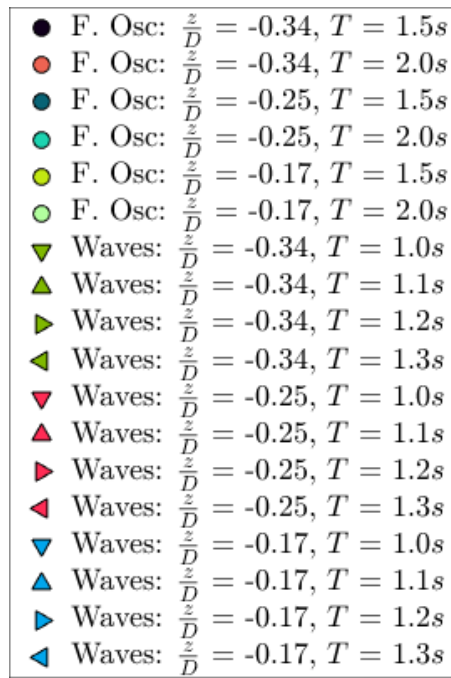


Figure 5.36: Legend for remaining figures showing results for the normalized force and drag coefficients (valid for C19 and C28).

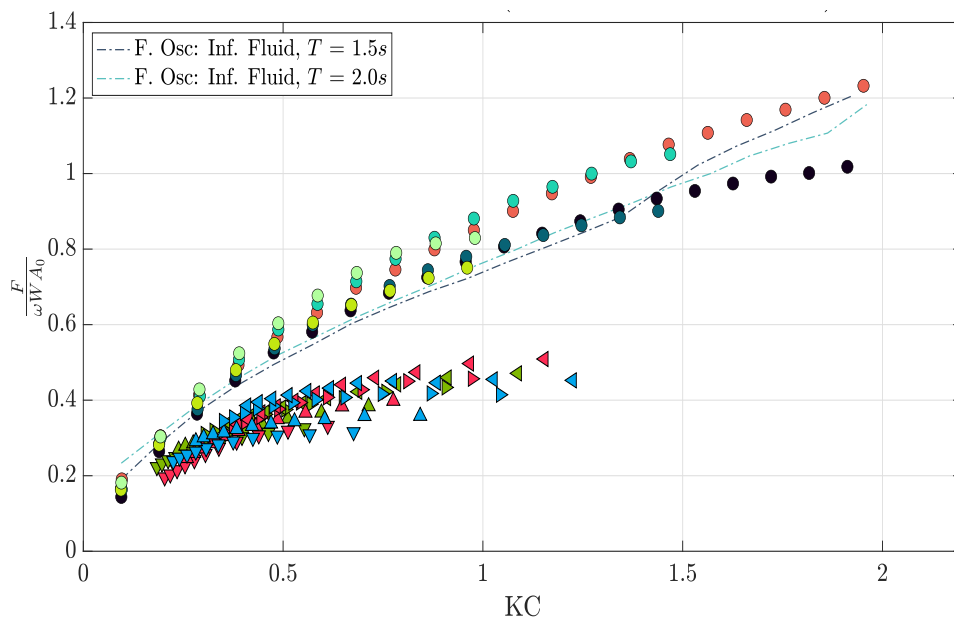


Figure 5.37: Comparison of the normalized force amplitude vs. KC for C19 ($r = 0.189$) in incident waves and forced oscillations. The legend is described in Figure 5.36. Results for deep water oscillations ($z = -50cm$) at $T = 1.5s$ and $T = 2.0s$ are also included.

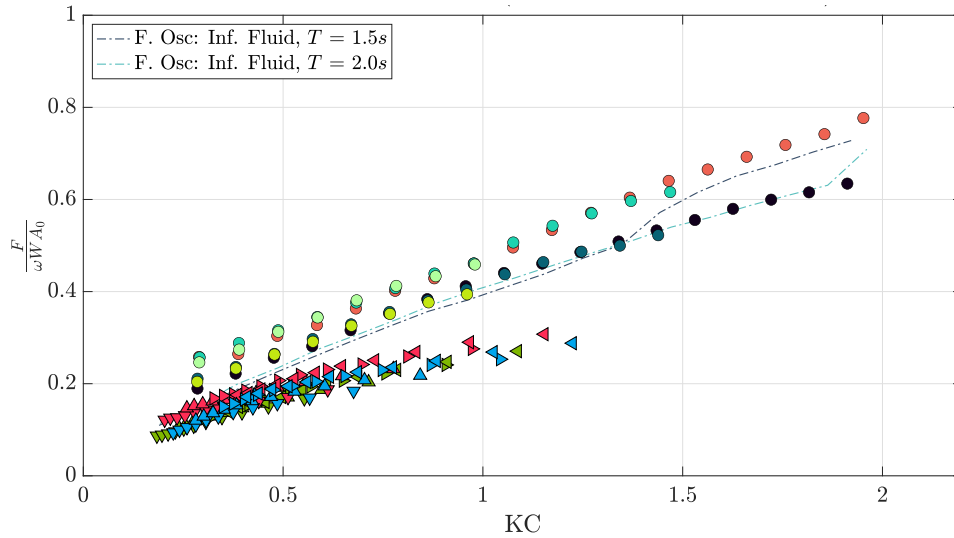


Figure 5.38: Comparison of the normalized force amplitude vs. KC for C28 ($r = 0.280$) in incident waves and forced oscillations. The legend is described in Figure 5.36. Results for deep water oscillations ($z = -50\text{cm}$) at $T = 1.5\text{s}$ and $T = 2.0\text{s}$ are also included.

Figures 5.37 and 5.38 depict the normalized force amplitudes for C19 and C28, plotted against the KC number. These figures contain data for all relevant submergences, where the data points for forced oscillations and waves are described in the legend in Figure 5.36. Four wave periods are considered: $T = 1.0\text{s}$, $T = 1.1\text{s}$, $T = 1.2\text{s}$, and $T = 1.3\text{s}$. It must be noted that these are slightly lower than the periods for forced oscillations, which are $T = 1.5\text{s}$ and $T = 2.0\text{s}$. The conditions are therefore not entirely similar, but the results show that variations in the wave period do not give rise to drastic differences in the force, thus it seems reasonable to compare the two cases. Results for deep water oscillations have also been included to serve as a reference point for the data. The main goal is to investigate the differences in the forces between harmonically oscillating plates and plates subjected to incoming regular waves, not to delve into the details of varying submergence. The effect of submergence for each test case has been investigated separately in the previous sections of this chapter. The data points are therefore presented in a combined plot, but results for separate submergences can be viewed in Appendix A.7 for C19 and Appendix A.8 for C28.

The results show that with increasing KC number, the normalized force on the models in incident waves becomes moderately to considerably smaller than the normalized force on the models when they are forced to oscillate. For the smallest tested KC numbers, the forces are similar for both waves and oscillations. It can also be seen that all values converge towards zero as the KC number approaches its zero limit for both models. This convergence is not as clear for the lowest submergences of C28 where data points follow a somewhat flatter curve, but reasons for this will be discussed in the following section on experimental errors. It can be noted that the similarity in forces occurs earlier for C28. While there is an approximate 20-50% difference in forces for C19 at $\text{KC} = 0.25$, the forces in waves are equal to those of deep water oscillations at the same amplitude of motion for C28. Differences can range anywhere from 25 - 100% for both C19 and C28 at $\text{KC} = 0.5$ and $\text{KC} = 2.5$ depending on the period and submergence, but the most important trend to note is that the differences increase as the KC number increases. These are approximate percentage differences based on the above figures and can therefore

deviate, but the values show a clear difference between waves and oscillations for a large KC range. It is assumed, based on the trends of these curves, that the differences will increase as the amplitude increases. As discussed in Section 5.1, Mentzoni [13] showed that the hydrodynamic coefficients for models with lower perforations are larger due to the larger presence of global vortex formation at the plate ends. This could explain why larger differences are observed for C19, if assumed that there are large differences in the type of flow field observed around the models in waves and oscillations. Even though these differences in the nature of the flow will also be relevant for C28, the differences in the forces will be lower if it is assumed that the plate end vortices are less prominent. We therefore need to take a closer look at the importance of plate end flow separation.

The importance of flow separation has briefly been discussed for the separate cases of forced oscillations and waves. To discuss the differences between waves and forced oscillations, we first need to understand the overall importance that plate end separation has on the total hydrodynamic loads. Due to the fact that CFD simulations are not in the scope of this thesis, but rather an important example of further work, we use results from the Doctoral Thesis by Fredrik Mentzoni on the hydrodynamic loads on complex structures in the wave zone. This serves as a reference point to examine and understand the results of this thesis, which is closely related based on experiments. If no other reference is given, the following explanations and findings are based on the study by Mentzoni, 2020 [11].

To further illustrate how flow separation at the plate ends affects the total hydrodynamic loads, Mentzoni performs so-called Hybrid CFD simulations for two perforated plates with porosities $r = 0.19$ (P19) and $r = 0.28$ (P28). These simulations are run with a potential flow solver at the plate ends, and a viscous flow solver at the plate center. This entails that the fluid can flow past the ends of the model, but plate end flow separation does not occur. Flow separation is therefore limited to its local form, i.e. at the openings along the width of the model. These results are compared to a viscous flow solver for the same plates, where flow end separation is allowed to occur.

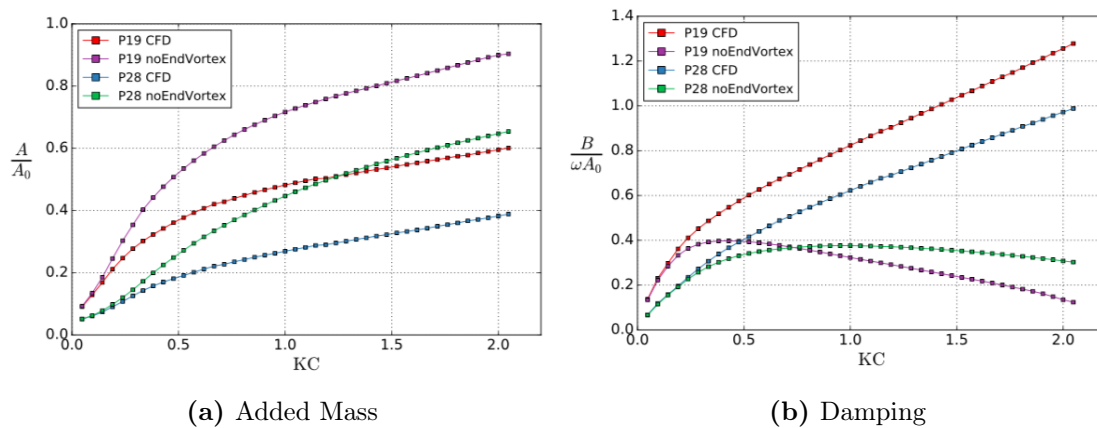


Figure 5.39: Added mass and damping coefficients vs. KC for P19 and P28, with and without the effects of plate end flow separation. Results are from the Doctoral Thesis by Mentzoni, 2020 [11].

Figure 5.39 illustrates the added mass and damping coefficients for the two models, both with and without the effects of plate end flow separation. It should be noted that these are results for simulations in infinite fluid, i.e. without the presence of a free surface. Results show an increase in added mass and reduction in damping for simulations without plate

end vortices. These are similar to the results from the semi-analytical method by Molin, 2011 [16] - the damping coefficients have a distinct maximum peak before they decrease with increased KC number, and the added mass coefficients increase for all values of KC (as shown in Figure 1.2). Looking back at Figure 1.3 from the study by Sandvik et al. [18], the comparison between the two cases are quite similar. The effect of plate end separation shows a clear importance on the coefficients, in particular the damping components. While the damping coefficients increase when end flow separation is accounted for, the added mass contribution decreases for all amplitudes. Results by Mentzoni and Sandvik also show that plate end flow separation depends on the KC number, i.e. for small amplitudes the effects are negligible. These results clearly illustrate that damping is largely under-predicted when plate end effects are not included, and further highlights their importance on the total hydrodynamic loads acting on structures either oscillating or subjected to incoming regular waves. Our results in this thesis have shown that damping is highly dominant for both test cases, thus these effects must not be neglected when trying to understand the hydrodynamic loads on perforated structures.

Based on the above discussion, it is evident that plate end separation is a large contributing factor to the overall hydrodynamic loads experienced by the models. To further understand why the forces differ in waves, we need to observe how the global vortices differ for the two cases. For the case of waves, there is a nonzero velocity component which affects the behavior of the flow over the model. In order to study how these global vortices differ in waves, Mentzoni performs so-called orbital flow simulations on S28. This is a square cylinder model with the same porosity as C28 ($r = 0.280$). He uses the same numerical set up as for forced oscillations, but with differing boundary conditions - a nonzero horizontal velocity component for orbital flow.

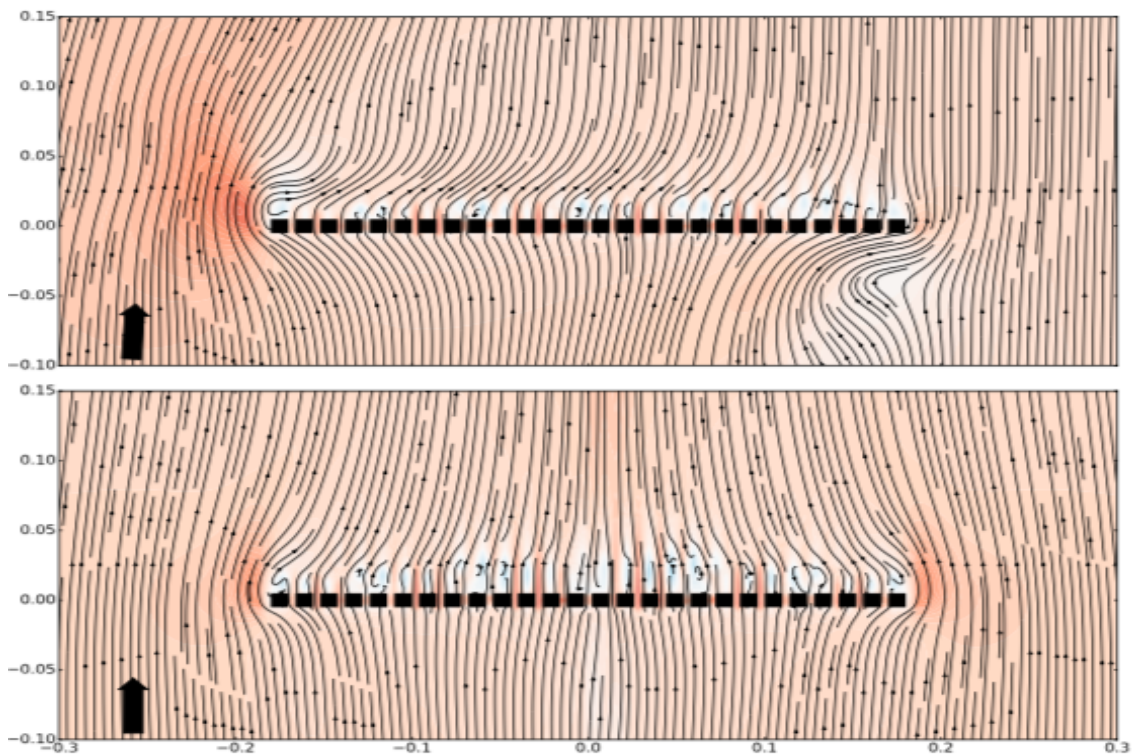


Figure 5.40: Streamline plots for S28 ($r = 0.280$) in orbital (top) and oscillating (bottom) flow conditions at $KC = 0.5$. Results are from the Doctoral Thesis by Mentzoni, 2020 [11].

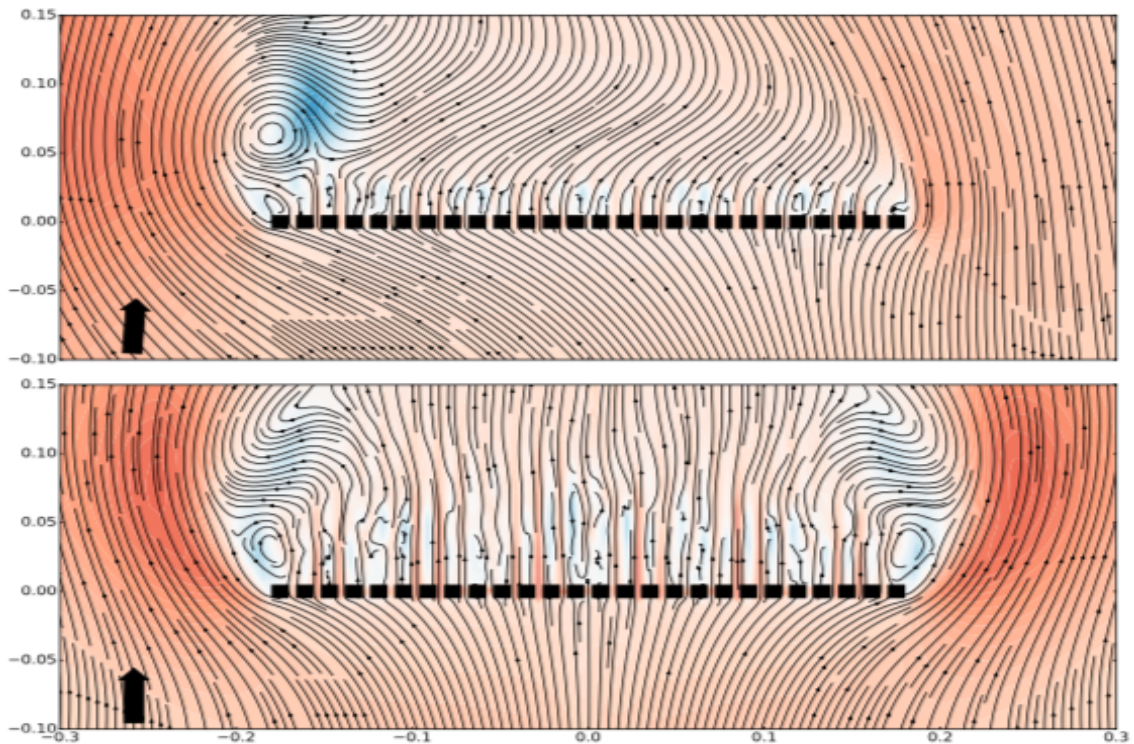


Figure 5.41: Streamline plots for S28 ($r = 0.280$) in orbital (top) and oscillating (bottom) flow conditions at $KC = 2.5$. Results are from the Doctoral Thesis by Mentzoni, 2020 [11].

Figures 5.40 and 5.41 show the resulting visualizations for S28 in orbital and oscillating flow conditions. Results are for $KC = 0.5$ and $KC = 2.5$. The top snapshot in both figures represents the results for orbital flow, while the lower snapshots are for the same model in oscillating conditions. The normalized force for both conditions is also quantified in Figure 1.4, which was presented in the literature review in Section 1.4. For the lowest KC number (Figure 5.40), the differences in the flow field between the two cases are minimal. There are no large global vortices at the model ends for either condition, only local disturbances at the plate openings. This explains why the forces in our results show increasing similarities as the KC number decreases towards zero. It is evident that even in waves, there is a minimal presence of plate end flow separation at low amplitudes of motion. In Figure 1.4, forces in oscillating flow are approximately 7% larger at $KC = 0.5$. This percentage difference is evidently higher for our results at the same KC number, but we observe an increased similarity for lower ranges of KC . As previously mentioned, forces in waves for C28 are equal to forces for deep water oscillations at $KC = 0.25$, while C19 shows an approximate 25 - 50% difference at the same KC number.

For $KC = 2.5$ (Figure 5.41), Mentzoni observes major differences in the flow field. Large global vortices at the plate ends are observed for both test cases (which explains an increase in the forces with higher KC), which are clearly dominant to the local separation occurring at the plate openings. The most interesting finding comes by looking at the nature of these global vortices. For orbital conditions, only a single large plate end vortex is observed at the left side of the model. For oscillating flow, a symmetrical pattern of plate end vortices are observed on *both* sides of the model. Looking back at Figure 1.4, Mentzoni observes a 50% reduction in the normalized force for orbital conditions compared to oscillating flow. This

is similar to what we observe in our own results for slightly lower KC ranges. Figure 1.4 shows that in orbital flow, there is a clear reduction in the normalized force for $KC > 1.5$. This reduction gives rise to the larger differences we observe at higher KC ranges. The fact that there is only one vortex in orbital flow, resulting in lower pressure, can explain why the forces differ in waves when the amplitude of motion increases. It can be assumed that the increasing prominence of plate end separation as the KC number increases, combined with the observed differing separation patterns, cause the increased differences observed in our own results as the KC range increases.

It is important to remember that, as Mentzoni mentions, orbital flow is an idealization of waves without the effects of a free surface. In his wave experiments, he finds considerable differences in forces compared to the case of forced oscillations even at $KC = 0.5$, which looking back at Figure 1.4 is not the case for orbital flow. This is also reflected in our own results, where larger differences are observed for the same KC number. Compared to the CFD results, we also see that larger differences between waves and oscillations from our experimental results are observed for lower values of KC. There are therefore various factors that come into play when explaining the differences in forces between waves and forced oscillations, such as the distance to the free surface and other free surface effects that differ for both cases. Overall, based on the findings that have been presented throughout this thesis and previous studies, it is assumed that differences in global vortex formation plays a significant role in the differing hydrodynamic behavior. The results by Mentzoni therefore serve as a sufficient explanation for our results based on the scope of this thesis.

5.3.3 Comparison of Drag Coefficients

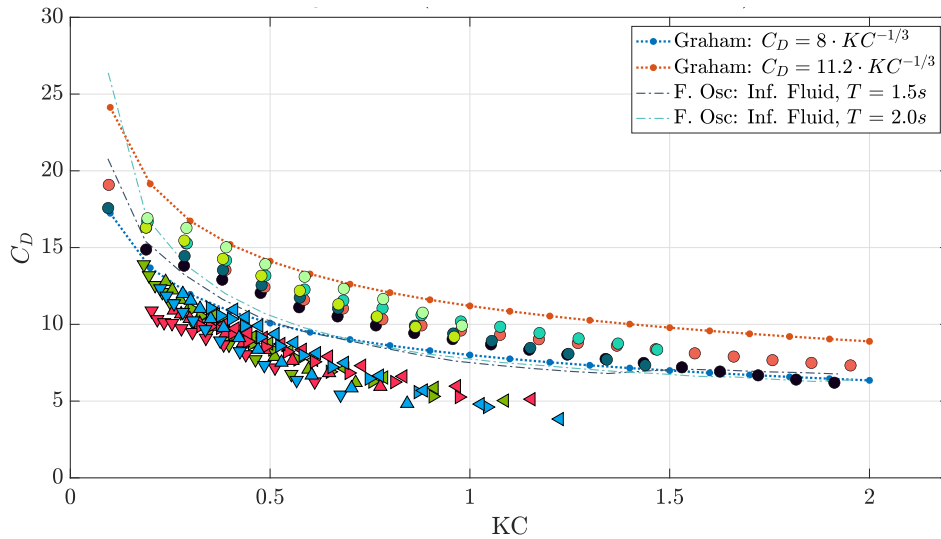


Figure 5.42: Comparison of the drag coefficients vs. KC for C19 ($r = 0.189$) in incident waves and forced oscillations. The legend is described in Figure 5.36. Results for deep water oscillations ($z = -50cm$) at $T = 1.5s$ and $T = 2.0s$ are also included, as well as suggested values by Graham, 1980 [7].

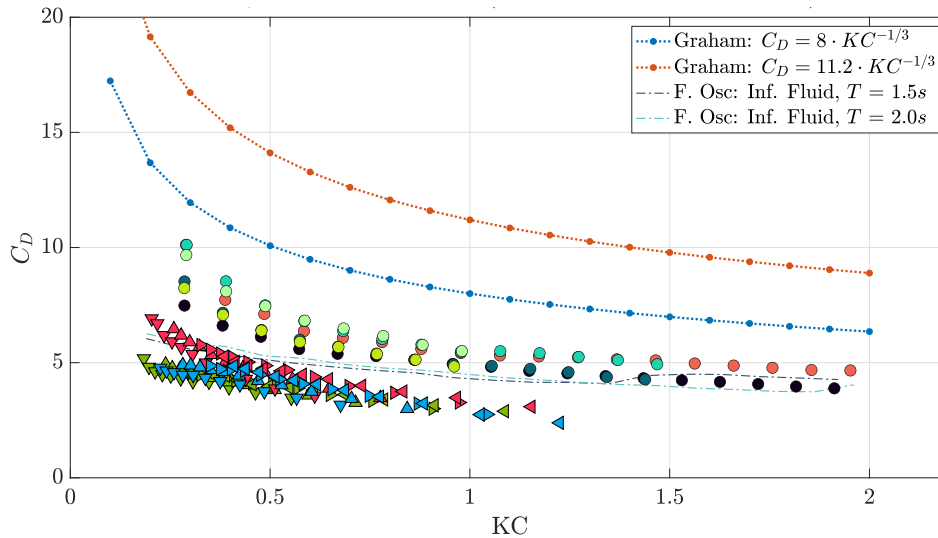


Figure 5.43: Comparison of the drag coefficients vs. KC for C28 ($r = 0.280$) in incident waves and forced oscillations. The legend is described in Figure 5.36. Results for deep water oscillations ($z = -50\text{cm}$) at $T = 1.5\text{s}$ and $T = 2.0\text{s}$ are also included, as well as suggested values by Graham, 1980 [7].

Figures 5.42 and 5.43 show the drag coefficients vs. KC for C19 and C28 for forced oscillations and waves. Deep water oscillation results at $z = -50\text{cm}$ are also included. As mentioned in previous discussions, the drag force is larger for C19 in both waves and oscillations. Models with lower perforation ratios experience a larger blockage effect, giving rise to a larger static pressure difference across the plate and thus a larger drag force. We also see an increase in drag force with decreased distance to the free surface for forced oscillations, and larger coefficients for the higher oscillation period of $T = 2.0\text{s}$. Comparing the drag forces for waves and oscillations, it is once again evident that wave tests give rise to lower forces. An increased similarity is observed for lower values of KC .

Experimental drag coefficients are also plotted against the suggested values by Graham, 1980 [7]. Comparing our experimental results to the values by Graham, we see that all results for C28 lie on the lower side of both curves. This is reasonable, as the suggestions by Graham are for a solid plate. We have seen throughout this thesis that the forces for models with higher perforations are lower due to a lower blockage effect and smaller global vortices at the plate ends. As previously discussed for C19, the values lie in between the theoretical and experimental curves by Graham. For deep water oscillations in particular, the drag coefficients are nearly identical to the curve for $C_D = 8KC^{-1/3}$ for most KC numbers. Although C19 is a perforated model, it becomes clear that even approximations for flat plates can give good estimates of the hydrodynamic coefficients. We have shown that the hydrodynamic loads are, most likely, dominated by the presence of large global vortices at the plate ends in oscillatory flow. Despite the presence of openings in the model, local flow separation and vortex formation will give small contributions in comparison to the larger global vortices. Although the size and nature of these global vortices will depend on the geometry of the plate (for example sharp-edged ends vs. cylindrical models), we can assume that at large amplitudes of motion, the plate end vortices will be of similar magnitude for flat plates and a ventilated model with low porosity. This could therefore serve as an explanation for the similarities observed in these results.

5.4 Discussion on Experimental Errors

Error is defined as the difference between the measured value and the true value. The difficulty with this is that the true value is rarely known. There are two main types of errors in experimental work - bias and precision error. Precision error represents the scatter in the experimental results, and is also referred to as random error. The precision error of an experiment can be found by running repeated tests. Bias errors are defined as systematic errors which can not be found from repeated measurements, but effective measures can be taken to minimize them.

For the case of forced oscillations, it is assumed that the precision error will be quite small. This due to the fact that 30 full-amplitude oscillation cycles were conducted, making it easier to extract steady state force measurements for further calculations. The oscillation parameters were consistent across these cycles, and the spread in resulting data was small. For the case of waves, 10 full-amplitude wave cycles were conducted. In hindsight, it would have been favorable to conduct tests over 20 or more repeated cycles due to small variations in the measured force. A maximum difference of 9% in the force was observed across the extracted full-amplitude cycles, but for most waves this value was lower. Inconsistencies were largest for the smallest waves at lower periods, thus this must be taken into account when observing the results. It is therefore evident that precision error is larger for tests in waves, due to less consistency in the wave parameters across the repeated cycles.

An obvious source of bias error is error in measurement readings, especially in relation to the calibration of the sensors used in all experiments. As discussed in Section 3.4, careful consideration was taken in the calibration of all sensors, and all instrumentation was checked regularly to validate the calibration factors. A number of different configurations were tested (i.e. different models and positions), meaning that the rig was removed and screws were loosened/tightened between runs. This would introduce differences, although small, to the experimental environment. To ensure similar conditions between tests, extra time was taken when removing and re-installing the rig. Checks were made to ensure that the models were level when fastened to the plexi-glass plates, and the rig was installed as carefully as possible so that the distance from the plates to the tank walls was sufficiently equal on both sides of the rig. The position of the model was also accurately measured before each trial to ensure similarity between experiments. Based on this, it is assumed that errors related to instrumentation and rig set up are insignificant.

Other sources of bias errors are changes in the external test environment, such as water temperature and water level in the tank. As previously discussed, the wave probes were quite sensitive to these external factors. As a result, they were re-calibrated on a daily basis and checked thoroughly between tests. The water level in the tank varies each day due to leakage from the tank inlets and outlets, but due to the large volume of the tank, this leakage is assumed to be minimal. Variations in the water depth would not affect the accuracy of the forced oscillation results, but the water level is an important factor for tests in waves. The wave generator was calibrated for a depth of 1m, thus large and frequent variations would lead to differences between the generated and desired waves. However, only a handful of wave tests were run on a daily basis and the water level was checked prior to each test to detect any significant changes. Zero readings were also taken for all test cases (including forced oscillations) to limit any sensor drift related to changes in the external environment. As a result, these errors are also deemed insignificant.

The model presence for wave tests at lower submergences can also lead to uncertainties

in the measured forces, especially if water is reflected back onto the incoming waves. This could explain slight variations in the force measurements over the full-amplitude cycles. Transverse waves can also be a source of bias error, but it is assumed that contributions are negligible. Wave generation for the case of forced oscillations, as well as lingering motion of the water due to previous oscillations, can also affect the overall measured forces. A waiting time of one minute was added in between runs to ensure sufficiently calm water for each test, thus reducing effects due to motions of the free surface. These are all factors which are difficult to control and detect prior to experiments, but they are still important to mention as possible sources of uncertainty in the measurements.

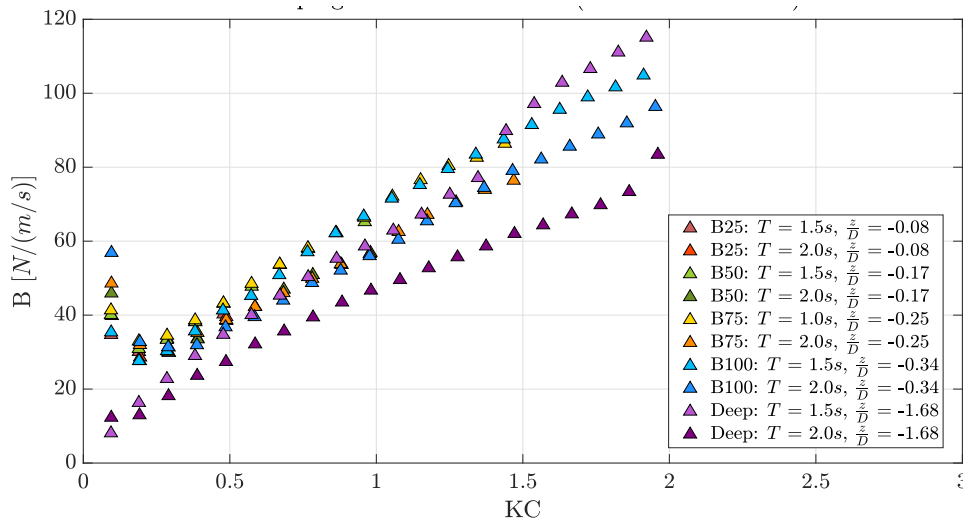


Figure 5.44: Damping force coefficients for C28 ($r = 0.280$) showing errors at low KC numbers for forced oscillation tests.

For the case of forced oscillations, evident errors were observed in the damping coefficients for C28 at $z = -2.5, -5, -7.5,$ and $-10cm$. Figure 5.44 shows incorrectly large data values at the lowest KC numbers. Oscillations in deep water were conducted separately, where the models were removed from the rig and manually installed at a deeper submergence. The four other submergences were conducted in a single run, where the position was automatically adjusted between each test case. Since these occurrences only occur for these positions, and not for C19 where the models were re-installed and conducted in an identical manner, it is tempting to conclude that these are errors due to the rig set up. One possibility is collisions with the tank walls for the smallest oscillations, but this is impossible to validate without physical evidence. The force on the model is found by subtracting the rig forces from the total measured force. If the net force on the model is small compared to the rig force, then the uncertainty increases. At large amplitudes, the forces on the model are much larger than those found in the empty rig trials. For the smallest oscillations they are very similar, thus increasing the uncertainty in the calculated forces used to find the damping and added mass coefficients. These errors are, however, not observed for the smallest oscillations in deep water or for the same submergences for C19. It is assumed that the results would follow a converging trend towards zero at low KC numbers, as was observed for C19. Due to these outlying values, the lowest data points were removed for C28. This must be taken into account when interpreting the results.

Chapter 6

Conclusion

The hydrodynamic loads on simplified subsea structures were investigated using experimental methods. Forced oscillation tests in deep water and at four varying submergences near the free surface were performed, as well as wave tests for the same four submergences. In the first case, the models (C19 and C28) were forced to harmonically oscillate in otherwise still fluid. In the second case, the models were fixed and subjected to incident regular waves with varying steepness and wave period. The goal was to study how the hydrodynamic loads varied with porosity and submergence, as well as provide a comparison of the loads in waves and oscillations.

Added mass and damping coefficients were presented for forced oscillations. Added mass coefficients showed a decreasing trend with decreased distance to the free surface, excluding the data for deep water oscillations. While a steady increasing curve was observed in infinite fluid, the four other submergences showed an increase in added mass up to a certain KC number, followed by a steady decrease towards zero and negative values. These values were also plotted against suggested values by DNV-GL, which were conservative in comparison to the experimental results. Corresponding to the observed decrease in added mass, there was an increase in the damping coefficients for decreased submergence. The wave radiation damping was shown to increase significantly closer to the free surface, but its overall contribution to the damping force was small. It could therefore be assumed that the main contribution to the damping force was from nonlinear effects like flow separation along the plates. The hydrodynamic coefficients showed a strong dependence on the oscillation amplitude, and more period dependence was observed for C19. Results also showed that the hydrodynamic loads were larger for C19, i.e. for the model with the lowest perforation ratio. The added mass force could be 2-8 times larger for C19 depending on the submergence, while the damping force was approximately 2 times larger than values for C28. Based on the findings of previous studies, it was discussed that these differences were due to the differing flow fields around each model. C19 would have a higher blockage effect, as well as larger global vortices at the plate ends. An important observation for all tests was a clear and significant damping dominance, where this damping dominance was largest for C28 which had the higher perforation ratio.

The separate discussion on the wave test results also focused mainly on the added mass and damping coefficients. The added mass coefficients were very small, and a significant scatter in data was observed. The coefficients became more negative with decreased distance to the free surface. Once again the damping force was significantly dominant, more so for the case of forced oscillations. Largest damping was observed at the smallest

submergence. Larger hydrodynamic loads were observed for the model with the lowest perforation ratio (C19), and this was yet again assumed to be due to the differing flow fields around each model. The hydrodynamic coefficients were highly amplitude dependent, and more period dependence was again observed for C19. The hydrodynamic coefficients were calculated for runs where the models were fully submerged in waves. Time series for $z = -2.5\text{cm}$ were therefore presented to show the differences in the hydrodynamic loads when the models were partly in and out of water. Results showed that the hydrodynamic loads acting on the models were larger, with sharper peaks that indicated the occurrence of slamming forces. It was not deemed accurate to calculate the coefficients for these runs, thus time series were only presented to highlight how the loads can vary when structures are present directly in the wave zone.

Due to the large damping dominance observed for both cases, the normalized force was used to compare forced oscillations and waves. The normalized force was largest for forced oscillations at mid to high KC numbers. A 25-100% difference was observed for both models depending on period and amplitude, where this difference increased for the highest tested KC values. The forces became increasingly similar at the smallest KC values. For C19 and C28, the normalized forces for waves and oscillations converged towards the same values at $KC \approx 0.2$. For C28, however, the wave data was most equal to the results from deep water oscillations. A brief discussion was given on the sources of error regarding forced oscillation tests for C28, which could explain why less convergence was observed for the three other submergences. The experimental results from this thesis were tied in to the results from the recent Doctoral Thesis by Fredrik Mentzoni [11] to provide reasoning for the observed differences. Flow visualizations by Mentzoni showed that only a single large vortex was present in orbital flow (which is an idealization of waves), while symmetrical plate end vortices were observed at both plate ends for oscillating conditions. It was assumed that these differing flow patterns were the main reason for the observed differences between normalized force values for waves and oscillations at increasing KC values.

There are several suggestions for further work related to the topics that have been explored throughout this thesis. As previously mentioned, CFD simulations are not in the scope of this project. They do, however, serve a vital role in validating the results and can provide valuable reasoning for the observed results. CFD results by Mentzoni [11] have been used to visualize vortex formations at the plate ends in infinite fluid. To understand the behavior of the hydrodynamic loads near the free surface, it would be useful to perform CFD simulations for oscillating and orbital conditions near a rigid wall and free surface. This will make it possible to isolate the effects of free surface interactions, as well as understand their contribution to the overall hydrodynamic loads. Another suggestion is to investigate 3D effects through experiments and CFD, as recent experiments and numerical simulations are only valid for a two-dimensional setting. CFD simulations for models with circular cylindrical members would also be useful for further validation of the results presented in this thesis. When it comes to experimental work, repeated tests for models with differing geometry, porosity and complexity (such as small-scale, complete modules) should be studied. It would also be beneficial to obtain high-resolution imaging of fluid behavior when the models are in close proximity to the free surface. This would give more insight into the effects of free surface interaction, which have been assumed to be important for both the case of forced oscillations and waves. Due to time limitations, this could not be achieved in this project.

References

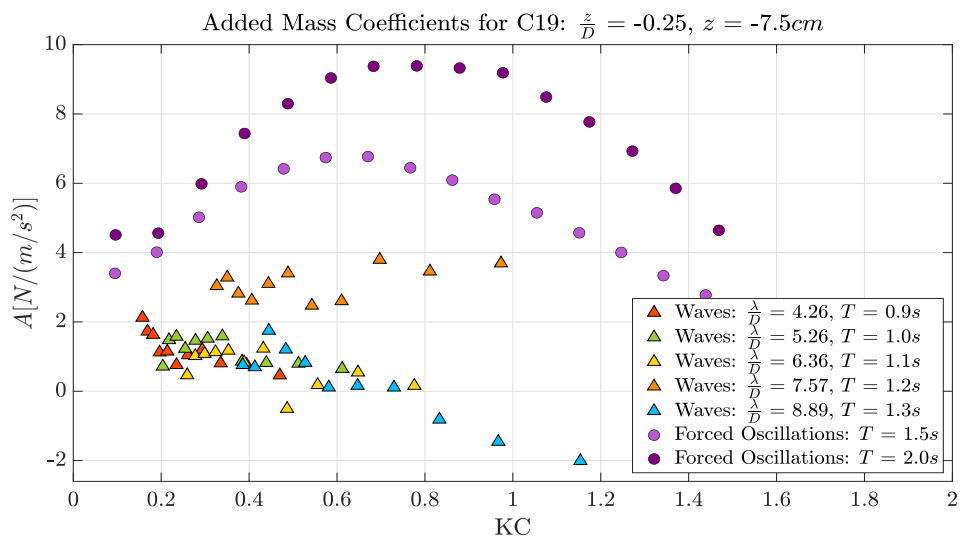
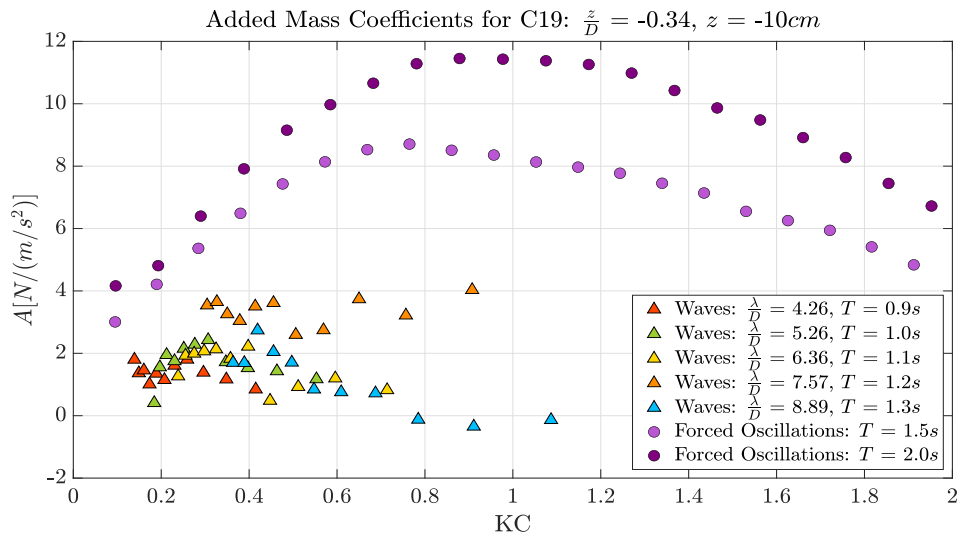
- [1] An, S. (2014). *Theoretical and experimental studies of wave diffraction and radiation loads on a horizontally submerged perforated plate*, Volume 2014:22. Trondheim: Norwegian University of Science and Technology, Faculty of Engineering Science and Technology, Department of Marine Technology.
- [2] An, S. and O. M. Faltinsen (2013). An experimental and numerical study of heave added mass and damping of horizontally submerged and perforated rectangular plates. *Journal of Fluids and Structures* 39, 87–101.
- [3] Blevins, R. D. (2003). *Applied Fluid Dynamics Handbook*. Malabar, Fla: Krieger Publ.
- [4] Brown, A., J. Thomson, and C. Rusch (2018). Hydrodynamic Coefficients of Heave Plates, With Application to Wave Energy Conversion. *IEEE Journal of Oceanic Engineering* 43(4), 983–996.
- [5] DNV-GL (2017). DNV-RP-H103: Modelling and Analysis of Marine Operations.
- [6] Faltinsen, O. M. (1993). *Sea loads on ships and offshore structures*. Cambridge Ocean Technology Series. Cambridge University Press.
- [7] Graham, J. M. R. (1980). The forces on sharp-edged cylinders in oscillatory flow at low Keulegan-Carpenter numbers. *Journal of Fluid Mechanics* 97(2), 331–346.
- [8] Gupta, P. (2018). *Experimental Investigation of Porous Structures in Splash Zone*. NTNU.
- [9] Kristiansen, T., E. B. Bachynski, D. Myrhaug, C. M. Larsen, and W. Lian (2019). *Marine Dynamics*. NTNU.
- [10] Mciver, P. and D. Evans (1984). The occurrence of negative added mass in free-surface problems involving submerged oscillating bodies. *Journal of Engineering Mathematics* 18(1), 7–22. Place: Dordrecht Publisher: Martinus Nijhoff, The Hague/Kluwer Academic Publishers.
- [11] Mentzoni, F. (2020). *Hydrodynamic Loads on Complex Structures in the Wave Zone*. NTNU. ISSN: 1503-8181.
- [12] Mentzoni, F., M. Abrahamsen-Prsic, and T. Kristiansen (2018). Hydrodynamic coefficients of simplified subsea structures. In *Proceedings of the ASME 2018 37th International Conference on Ocean, Offshore and Arctic Engineering*.
- [13] Mentzoni, F. and T. Kristiansen (2019). A semi-analytical method for calculating the hydrodynamic force on perforated plates in oscillating flow. In *Proceedings of the ASME 2019 38th International Conference on Ocean, Offshore and Arctic Engineering*.

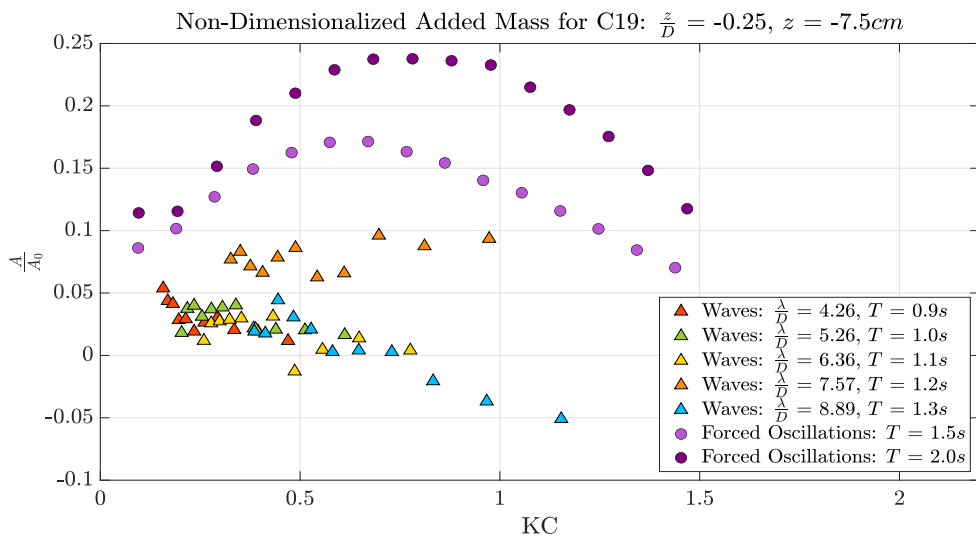
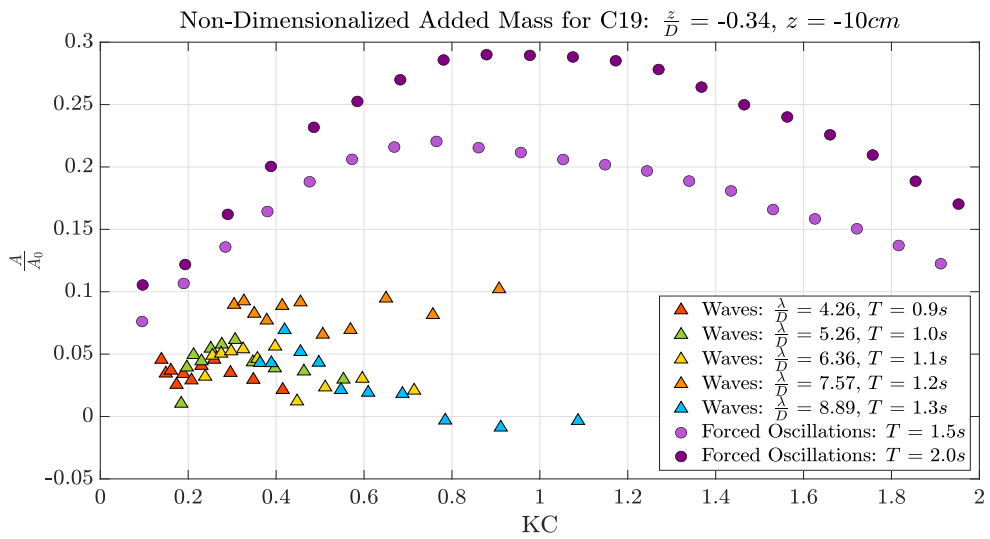
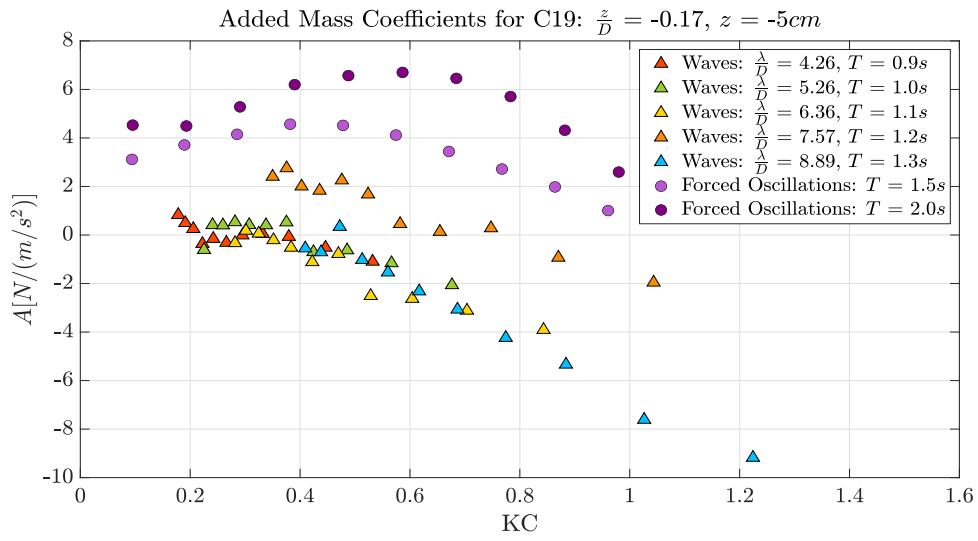
- [14] Mentzoni, F. and T. Kristiansen (2020). Two-dimensional experimental and numerical investigations of parallel perforated plates in oscillating and orbital flows. *Applied Ocean Research* 97.
- [15] Molin, B. (2001). On the added mass and damping of periodic arrays of fully or partially porous disks. *Journal of Fluids and Structures* 15(2), 275–290.
- [16] Molin, B. (2011). Hydrodynamic modeling of perforated structures. *Applied Ocean Research* 33(1), 1–11.
- [17] Morison, J., J. Johnson, and S. Schaaf (1950). The Force Exerted by Surface Waves on Piles. *Journal of Petroleum Technology* 2(05), 149–154.
- [18] Sandvik, P. C., F. Solaas, and F. G. Nielsen (2006). Hydrodynamic forces on ventilated structures. In *Proceedings of the Sixteenth International Offshore and Polar Engineering Conference*, pp. 54–58.
- [19] Sarpkaya, T. (1981). Morison’s Equation and the Wave Forces on Offshore Structures. Technical report, Naval Civil Engineering Laboratory, California.
- [20] Singh, S. (1979). *Forces on bodies in an oscillatory flow*. London: Department of Aeronautics, Imperial College, University of London.

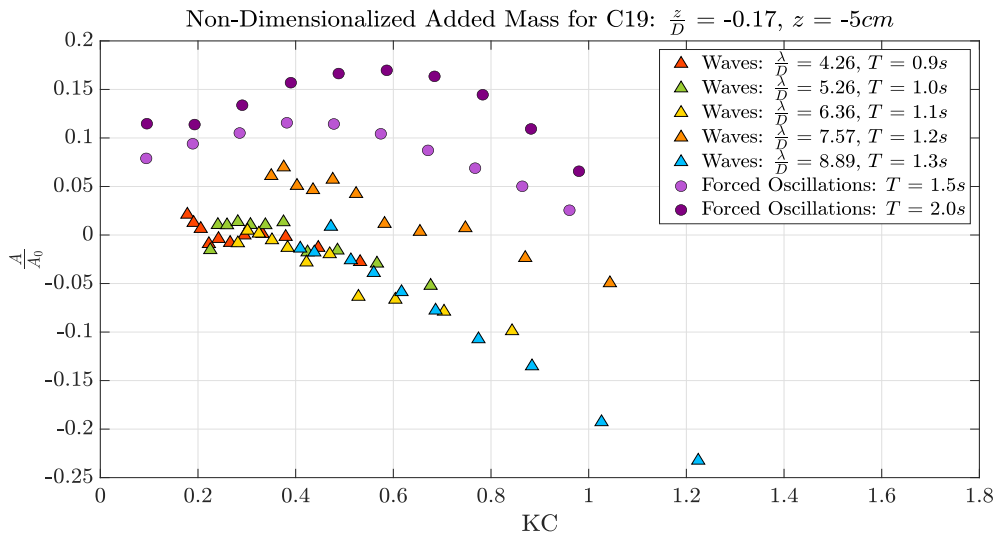
Appendices

A Comparison of Forced Oscillations and Waves

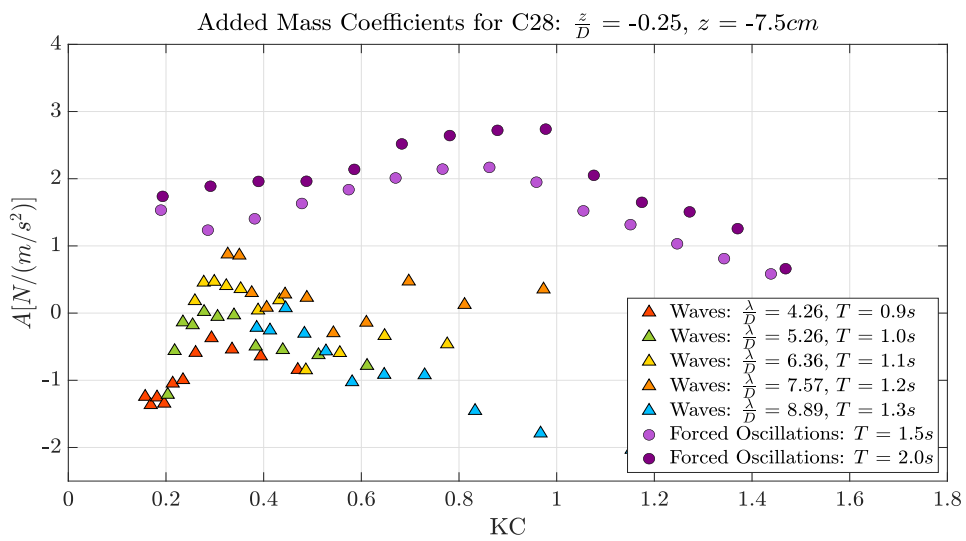
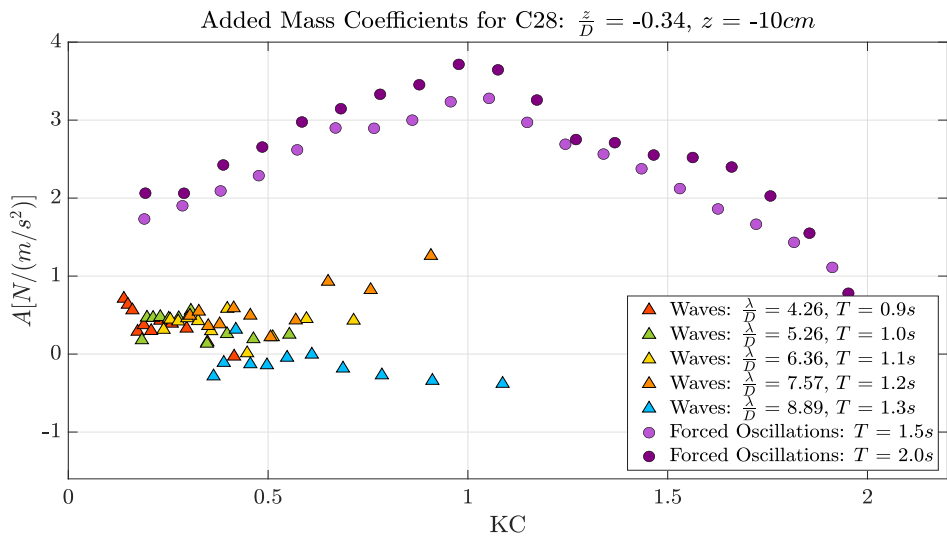
A.1 Added Mass Coefficients for C19

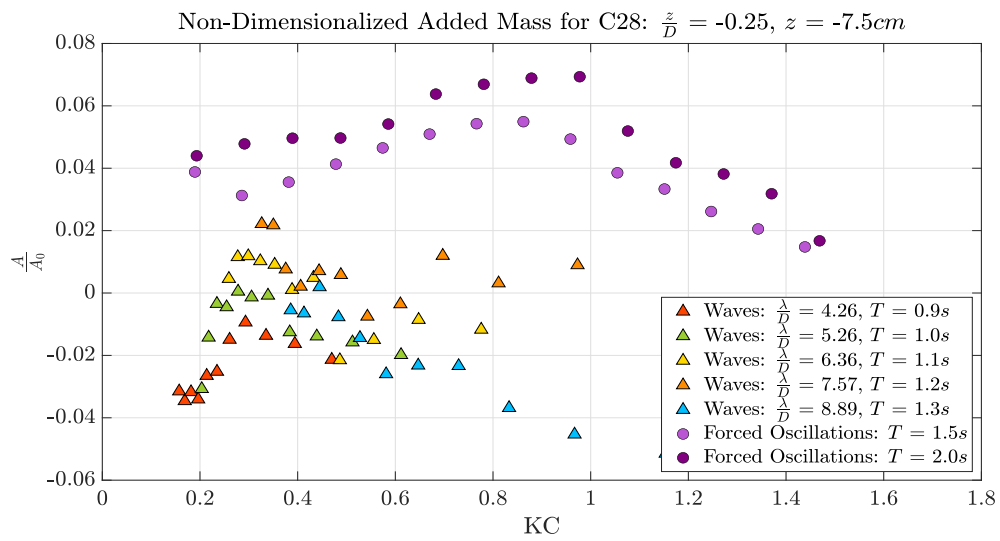
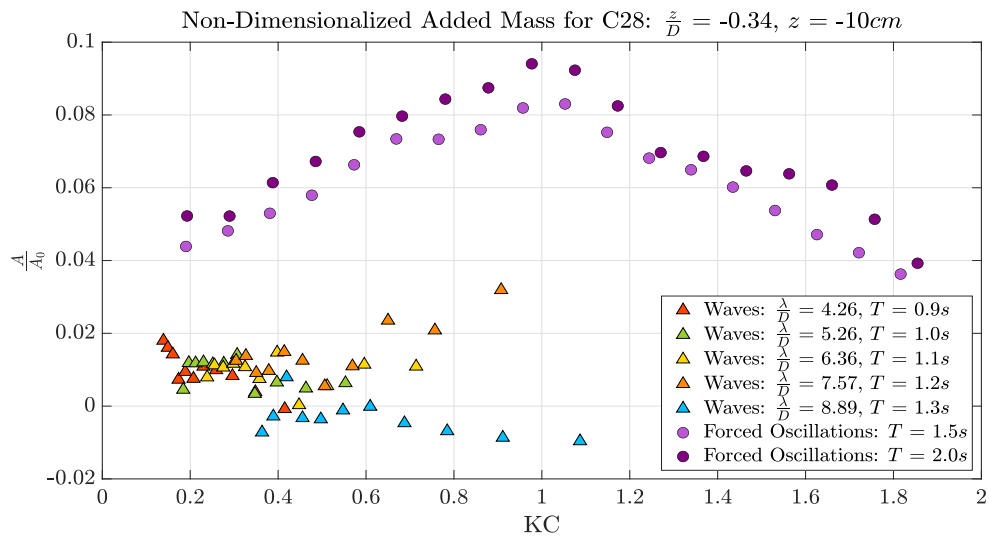
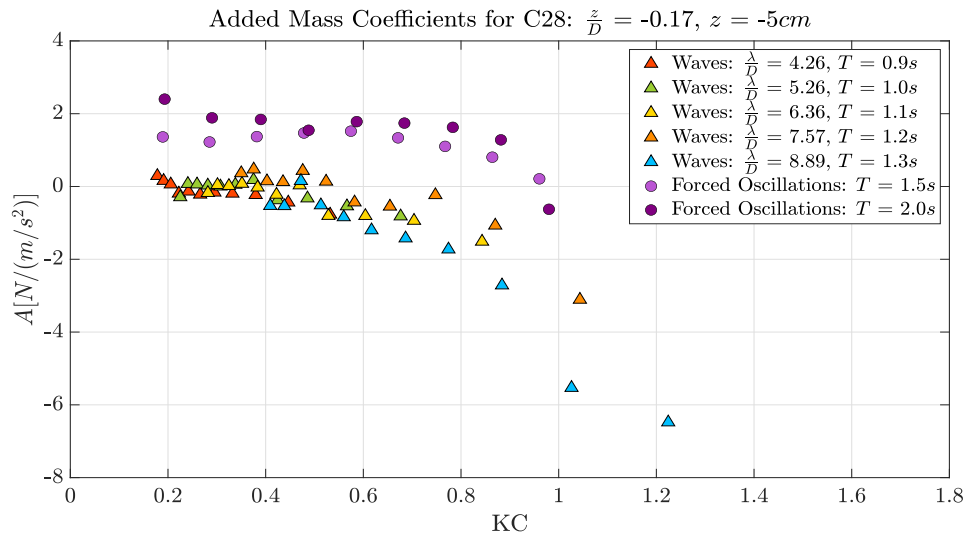


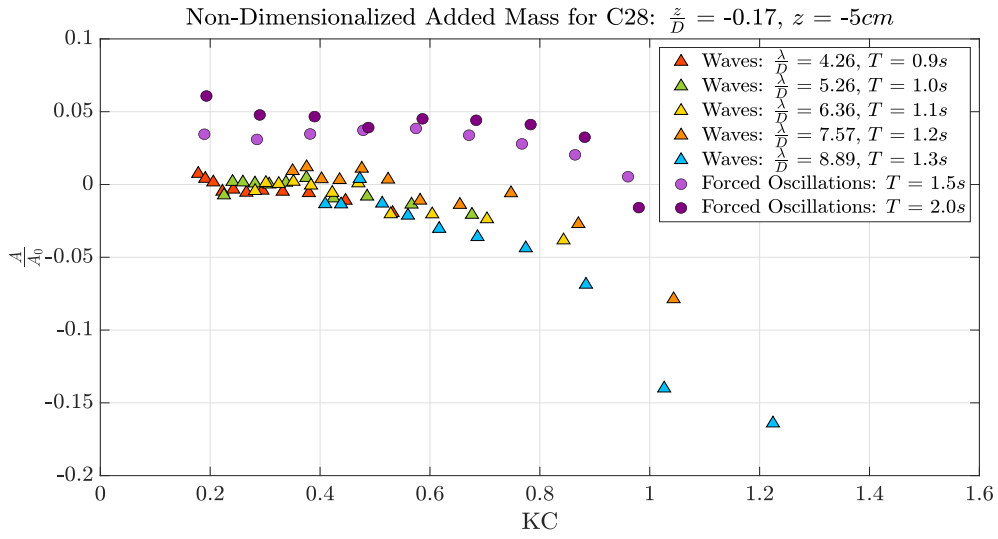




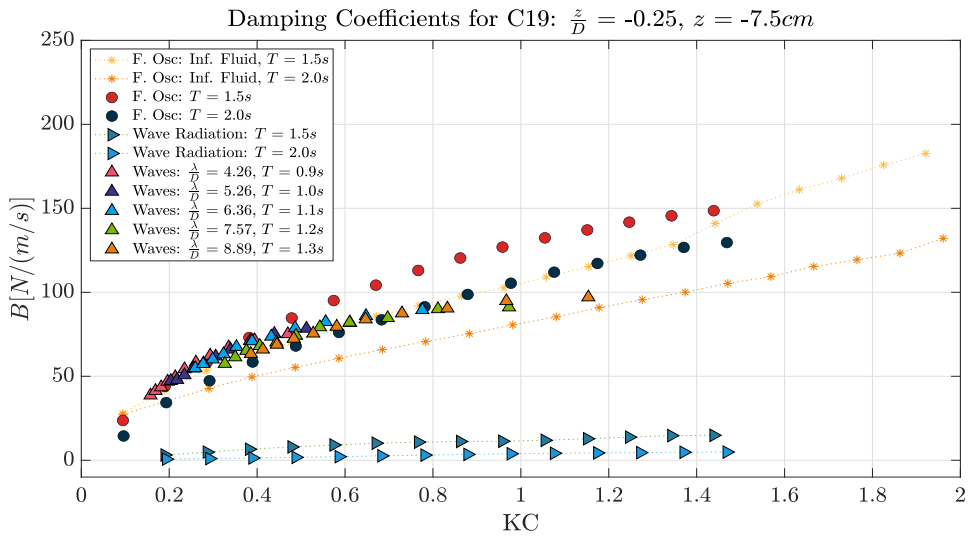
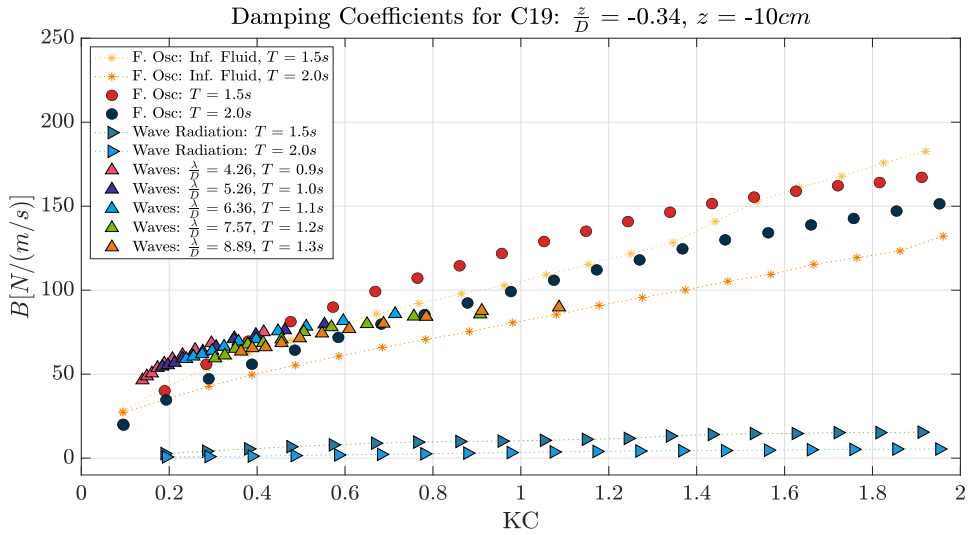
A.2 Added Mass Coefficients for C28

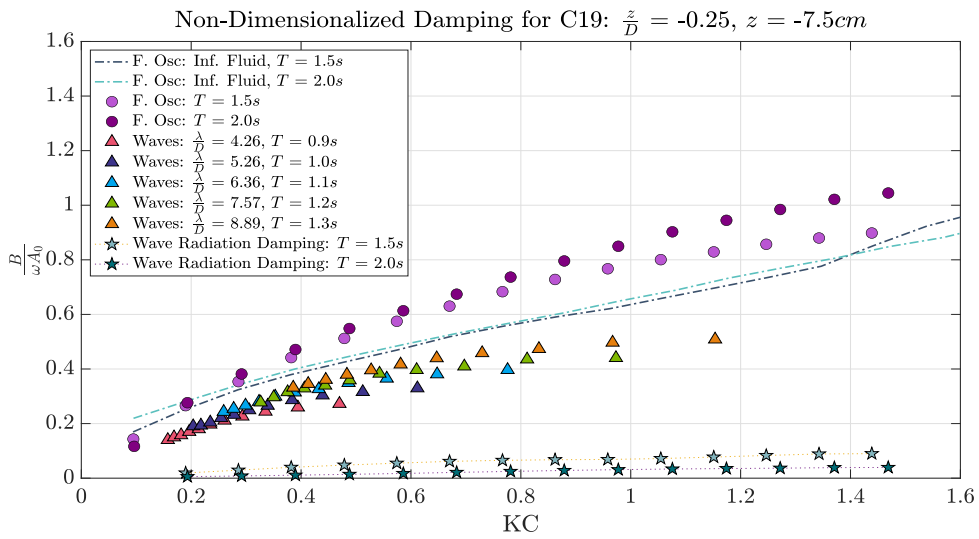
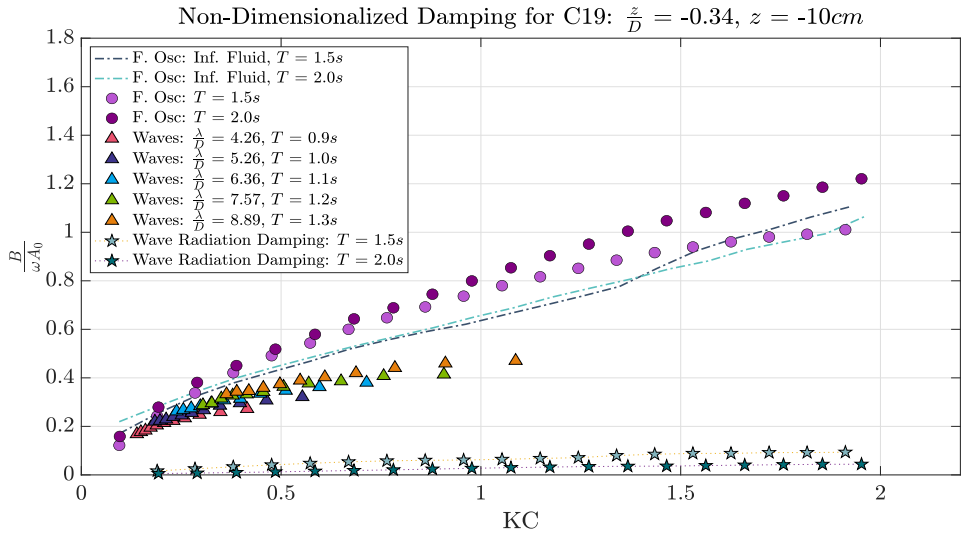
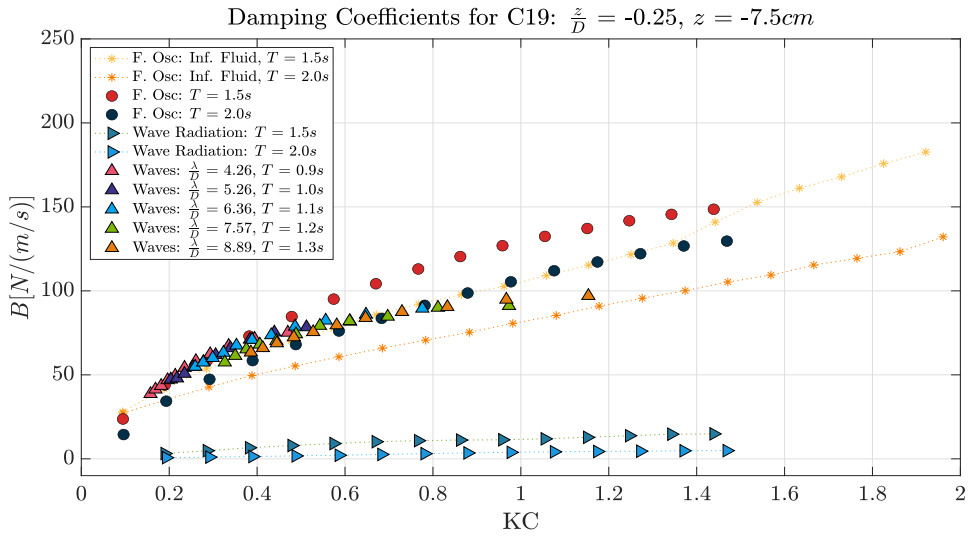


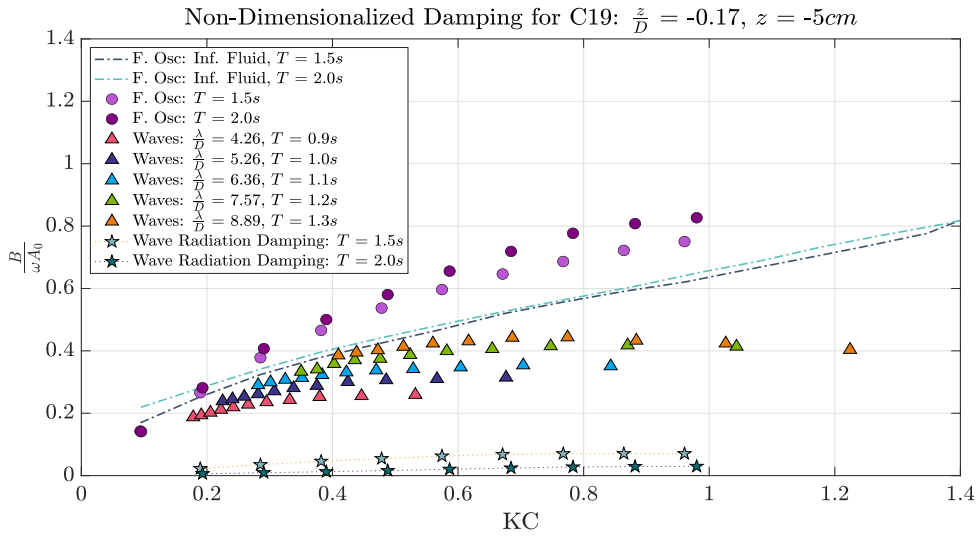




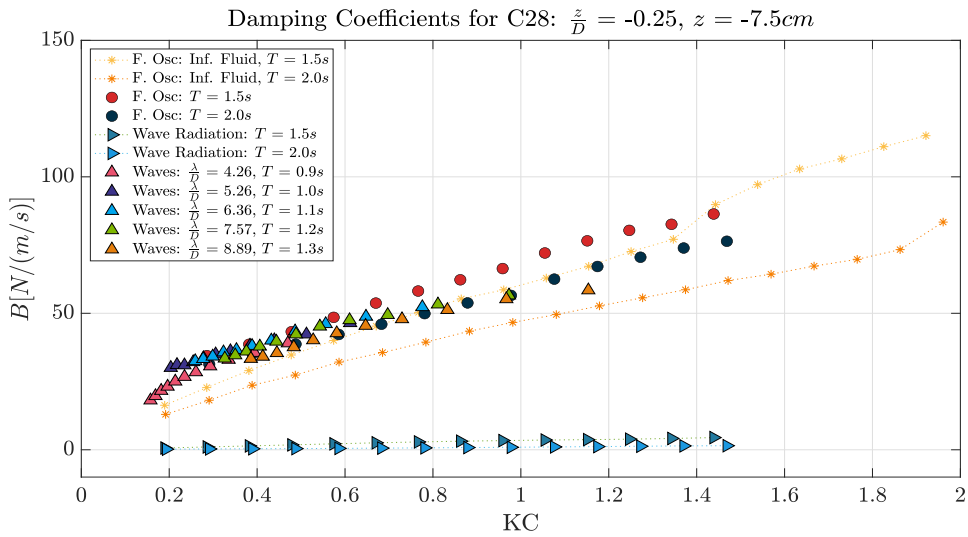
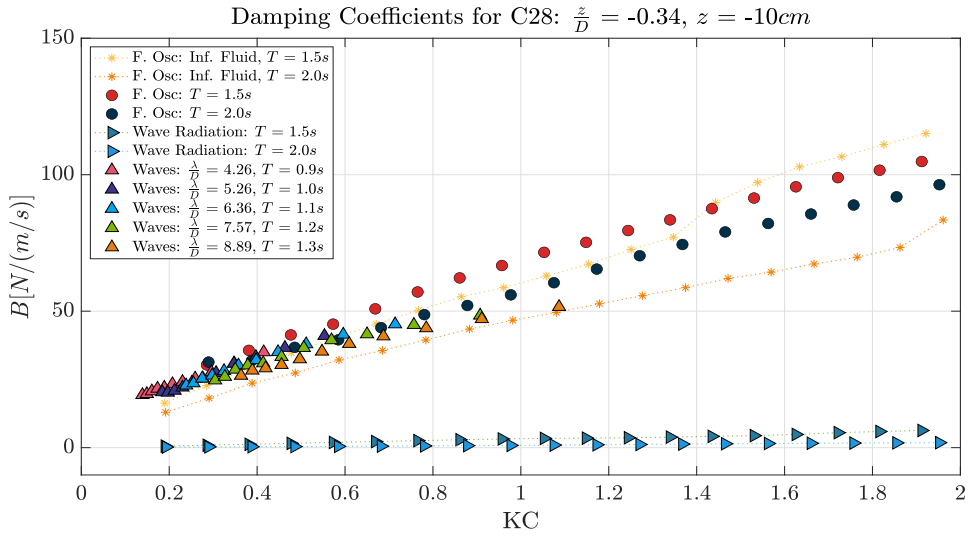
A.3 Damping Coefficients for C19

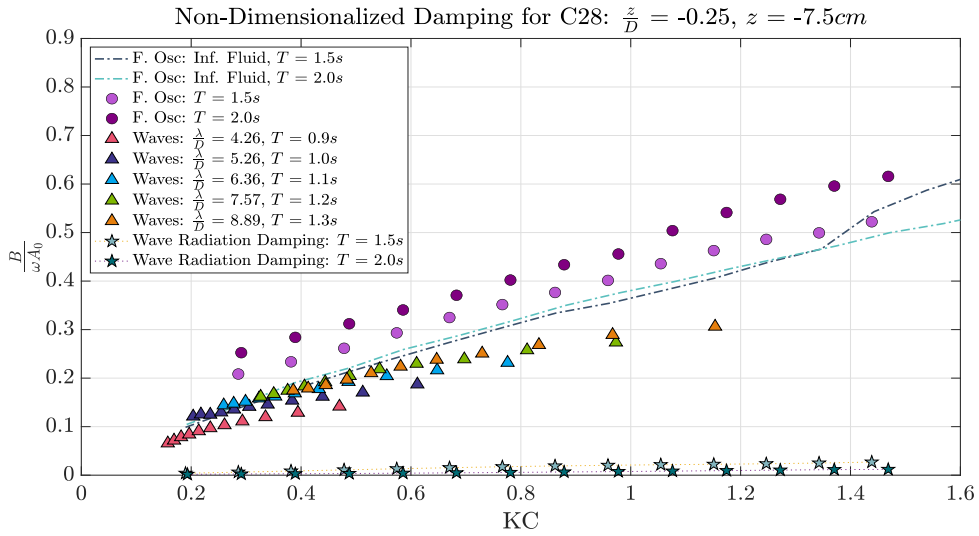
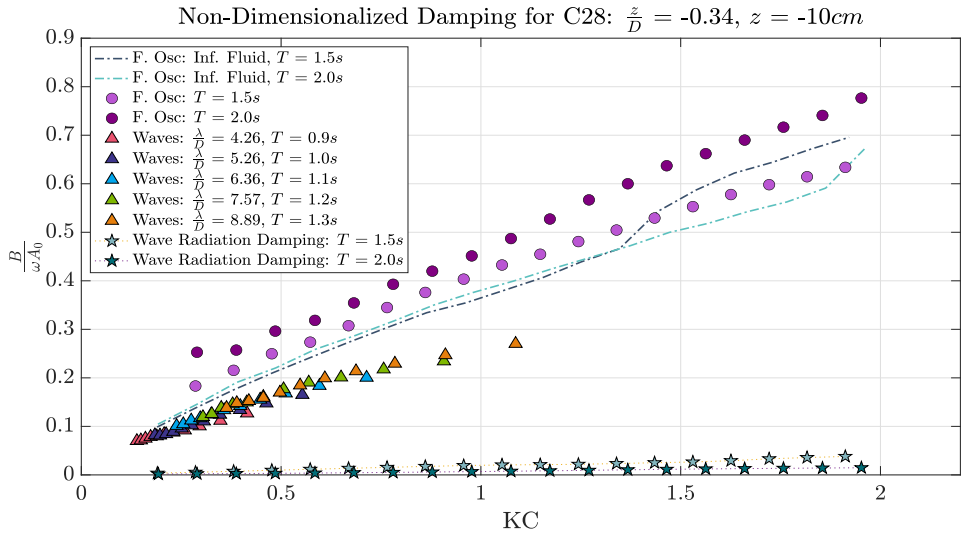
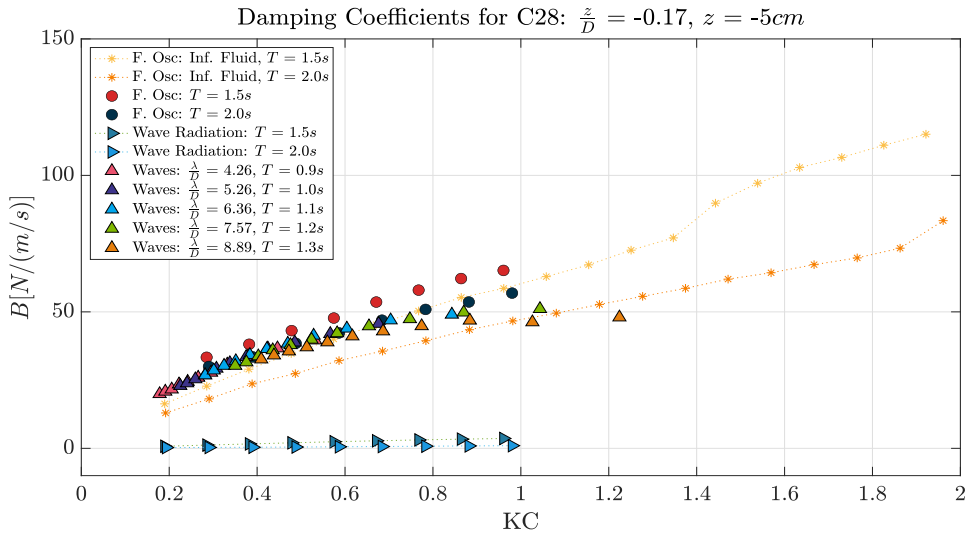


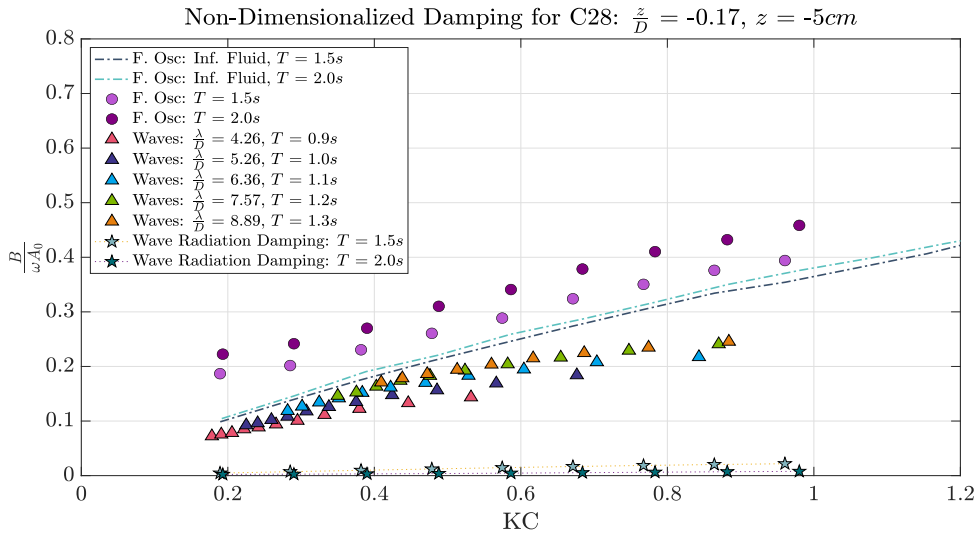




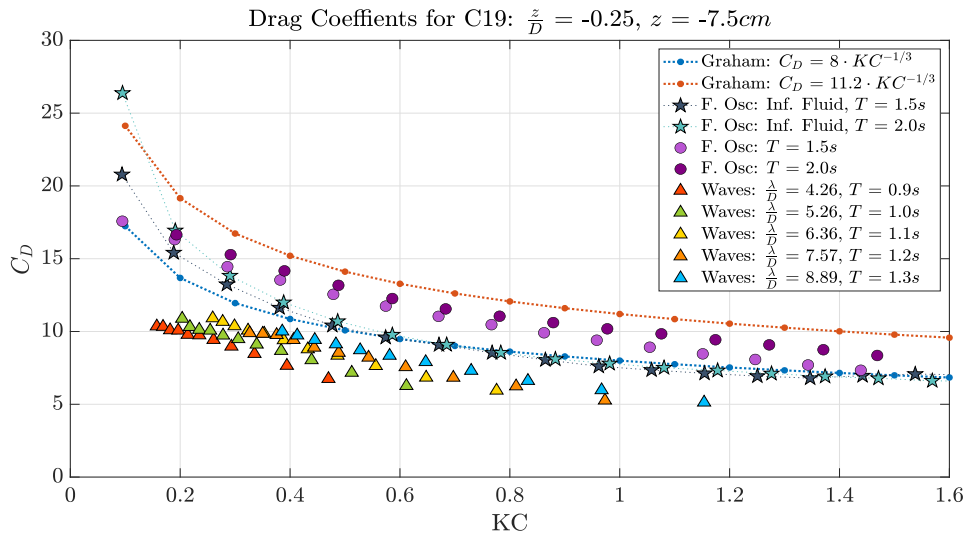
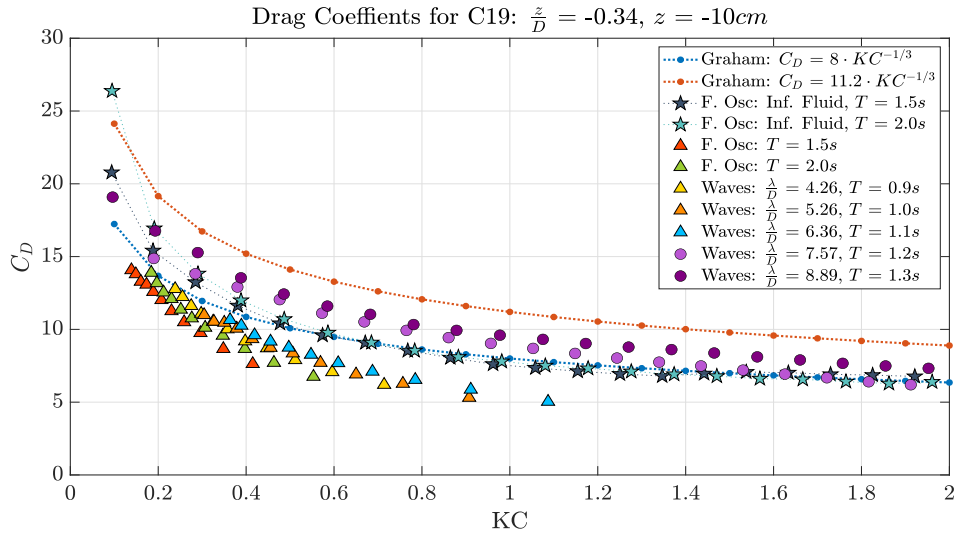
A.4 Damping Coefficients for C28

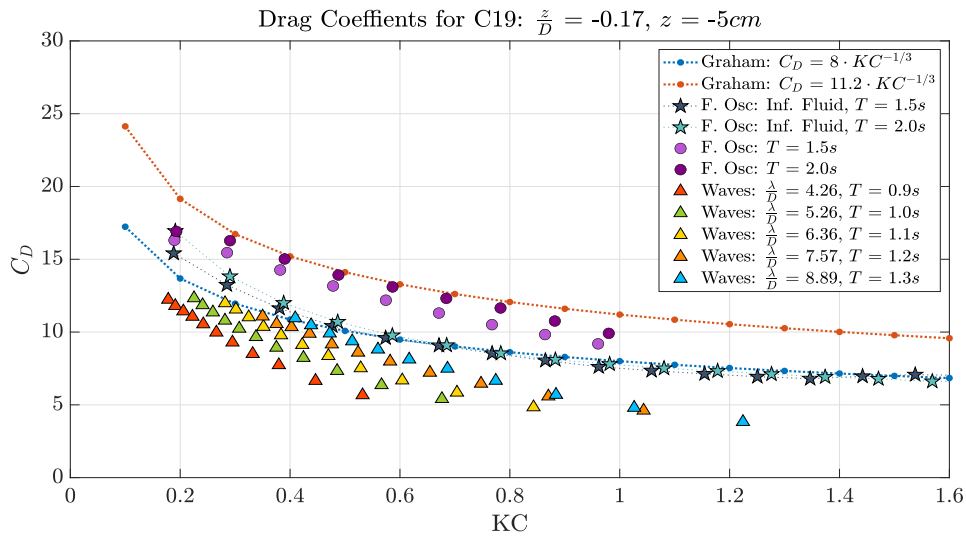




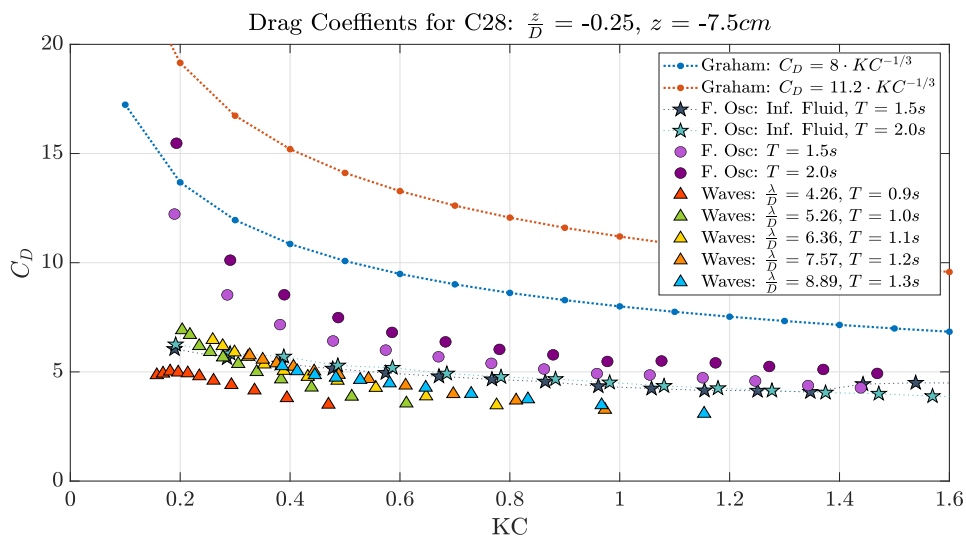
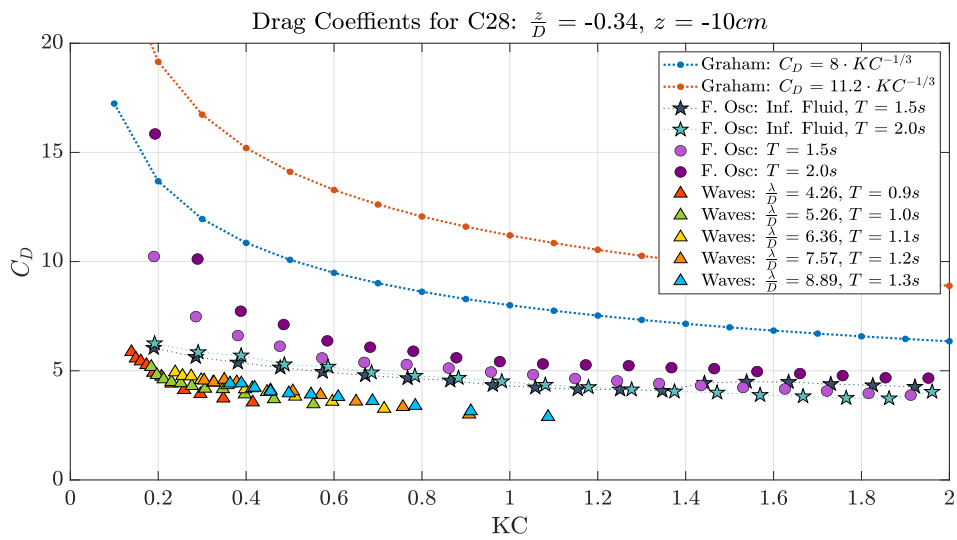


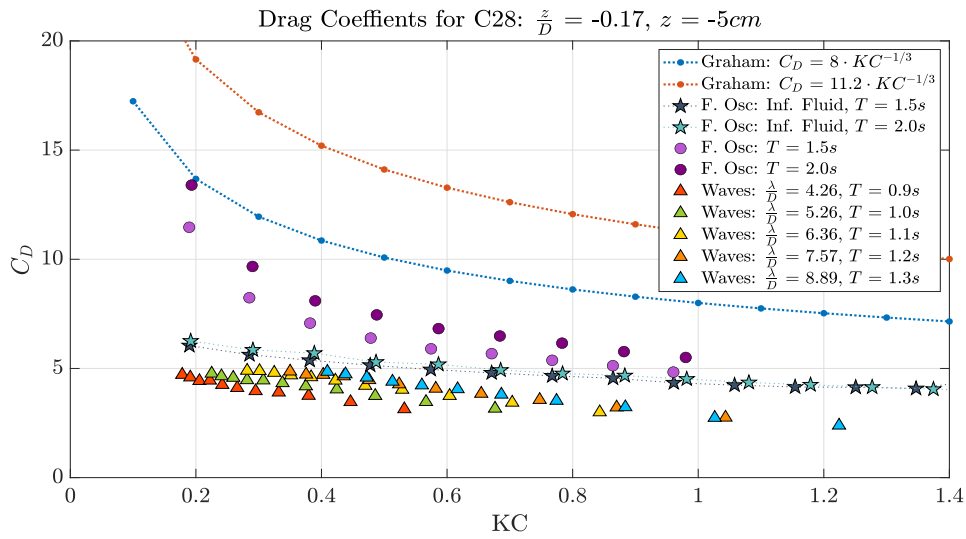
A.5 Drag Coefficients for C19



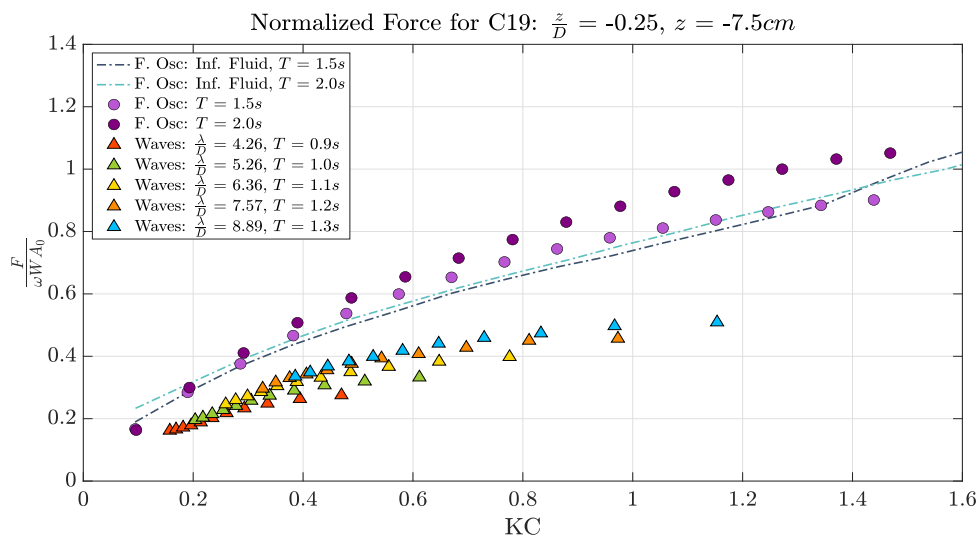
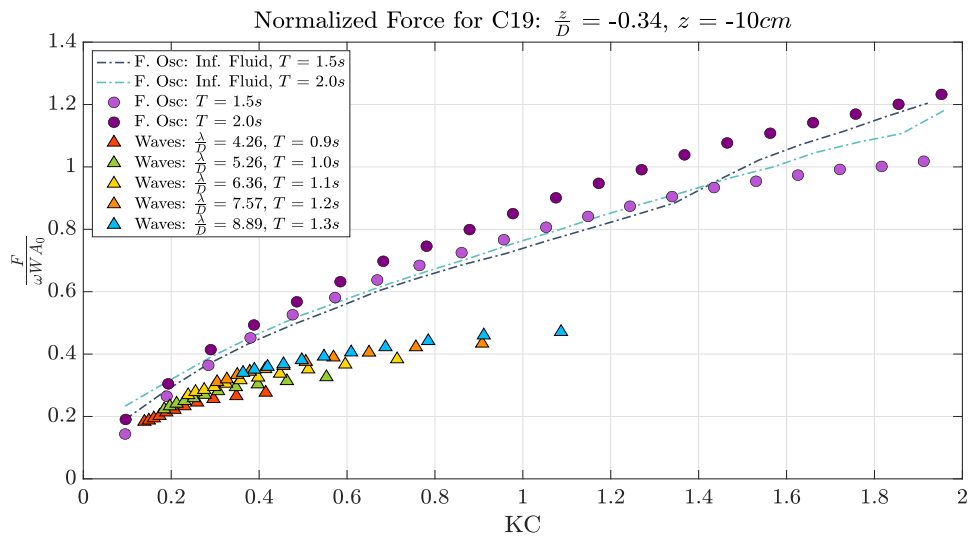


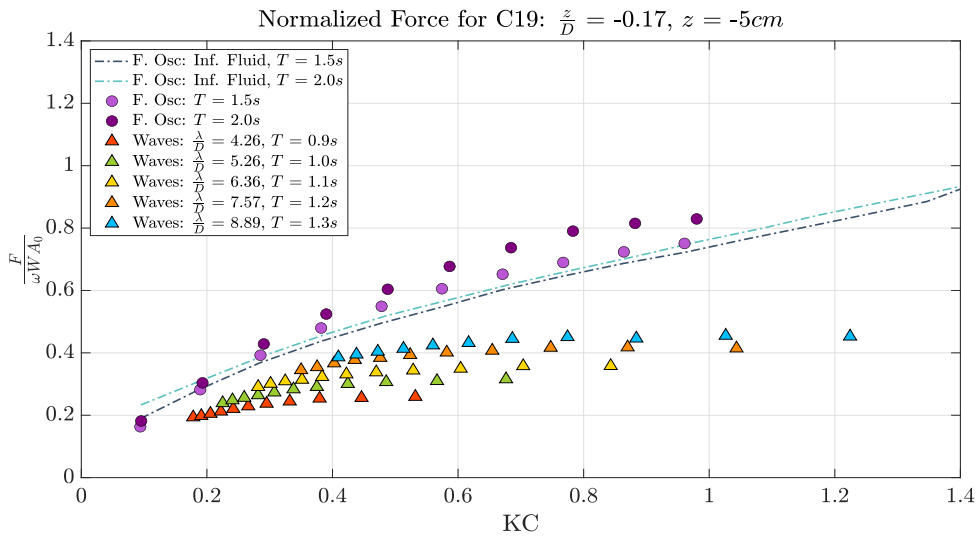
A.6 Drag Coefficients for C28



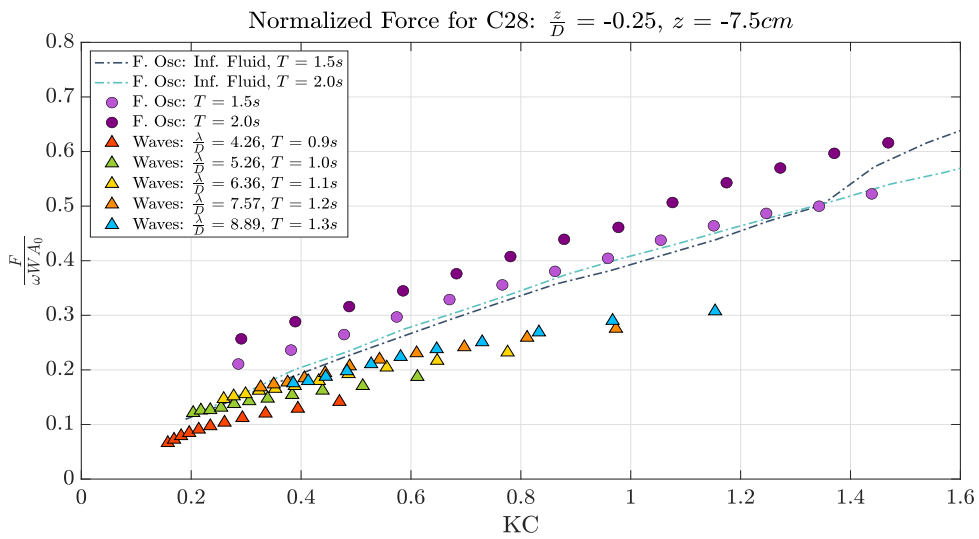
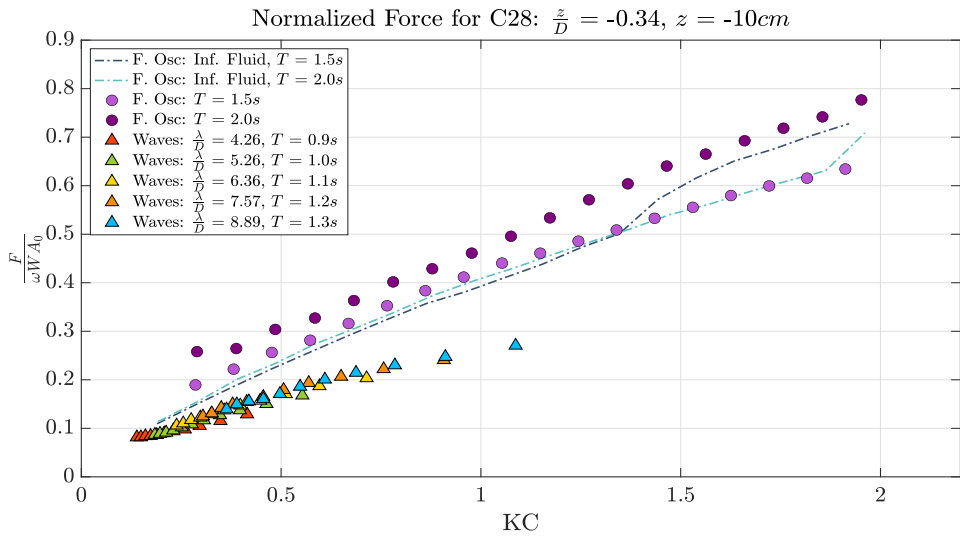


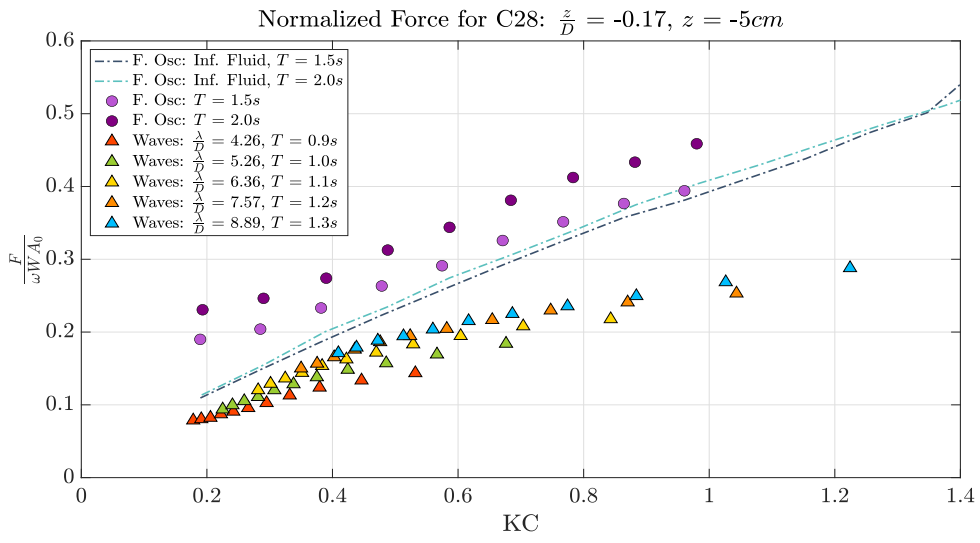
A.7 Normalized Force for C19





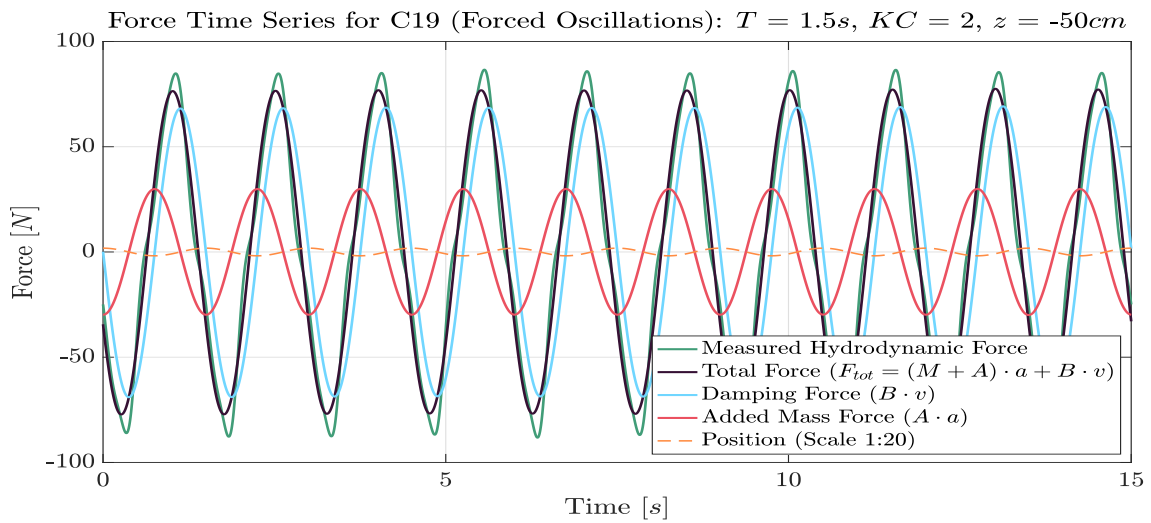
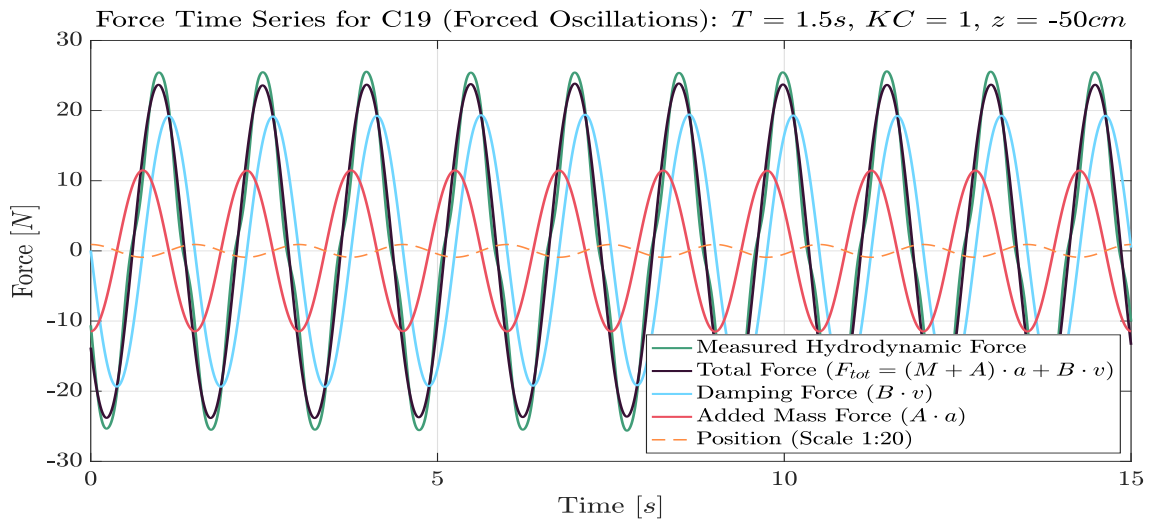
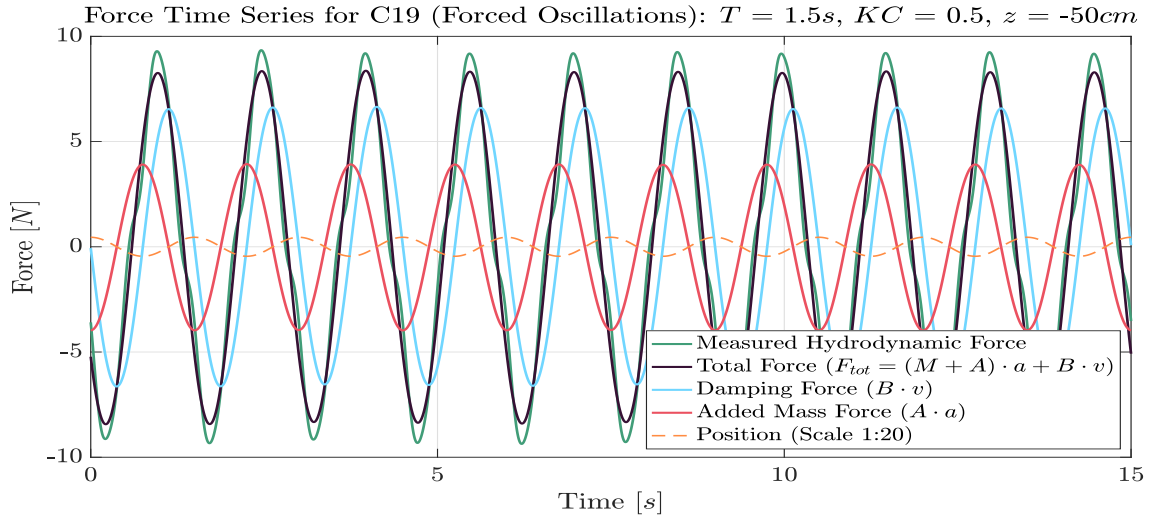
A.8 Normalized Force for C28

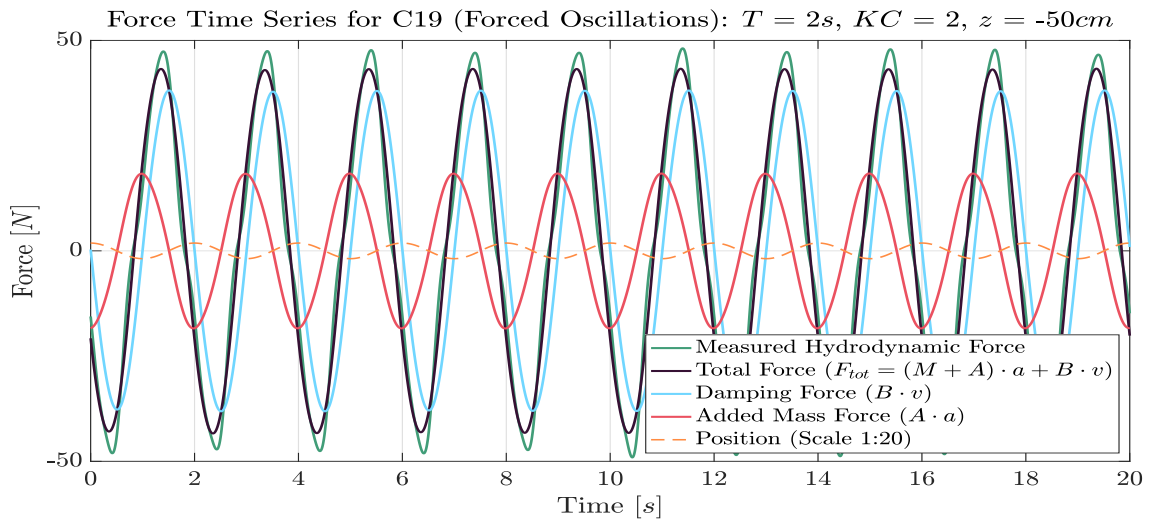
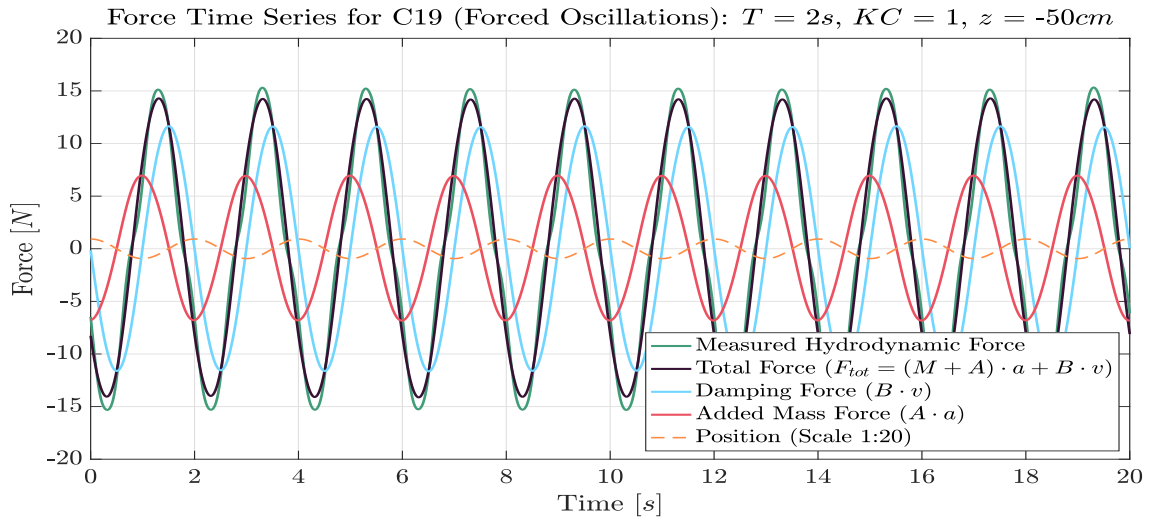
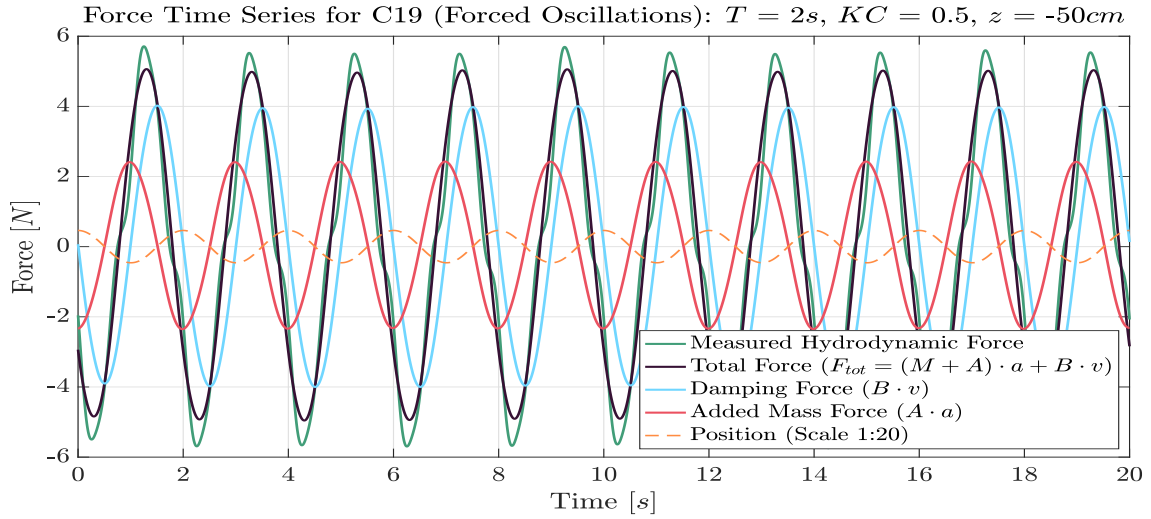


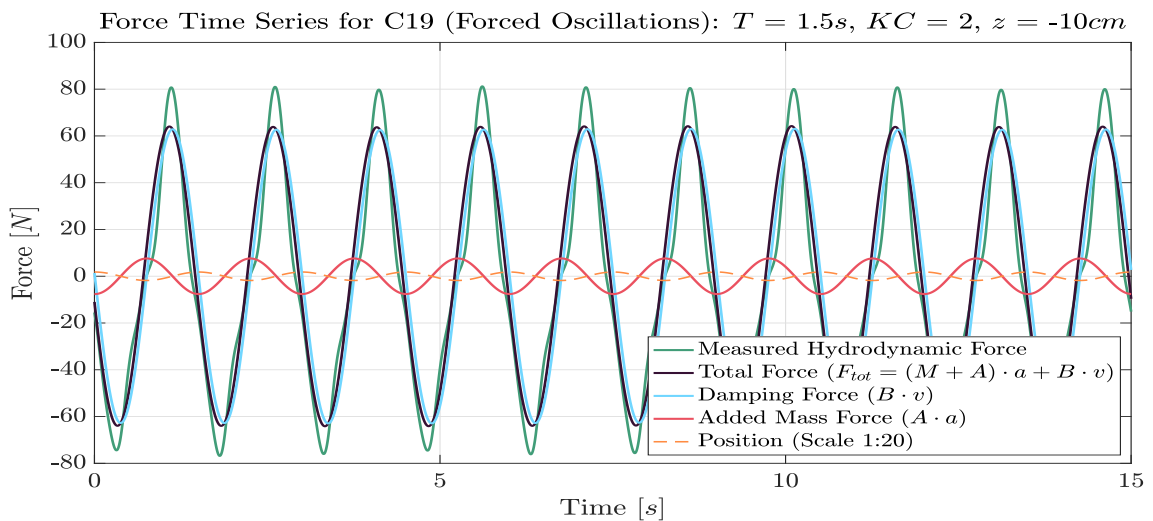
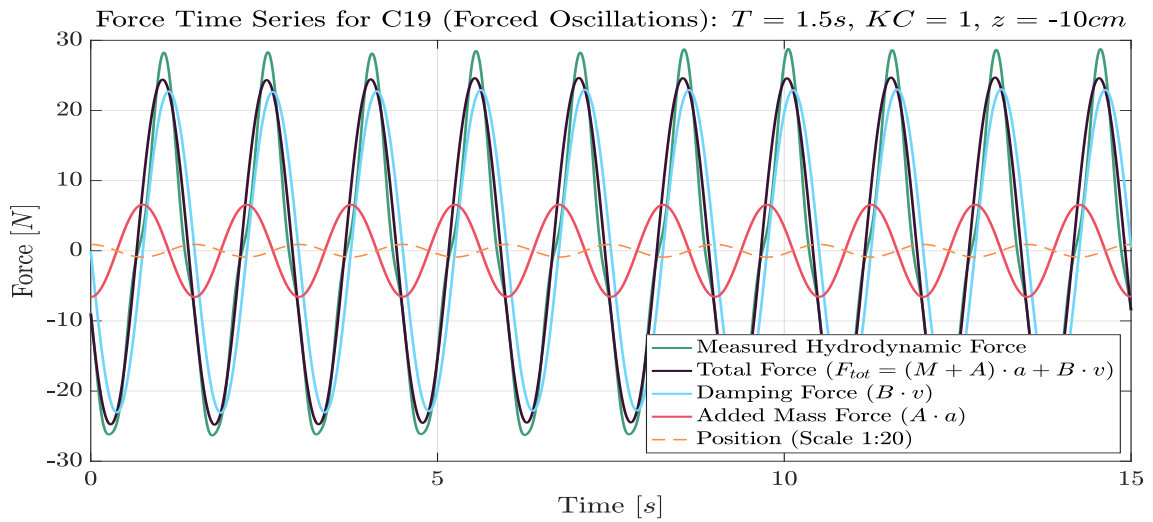
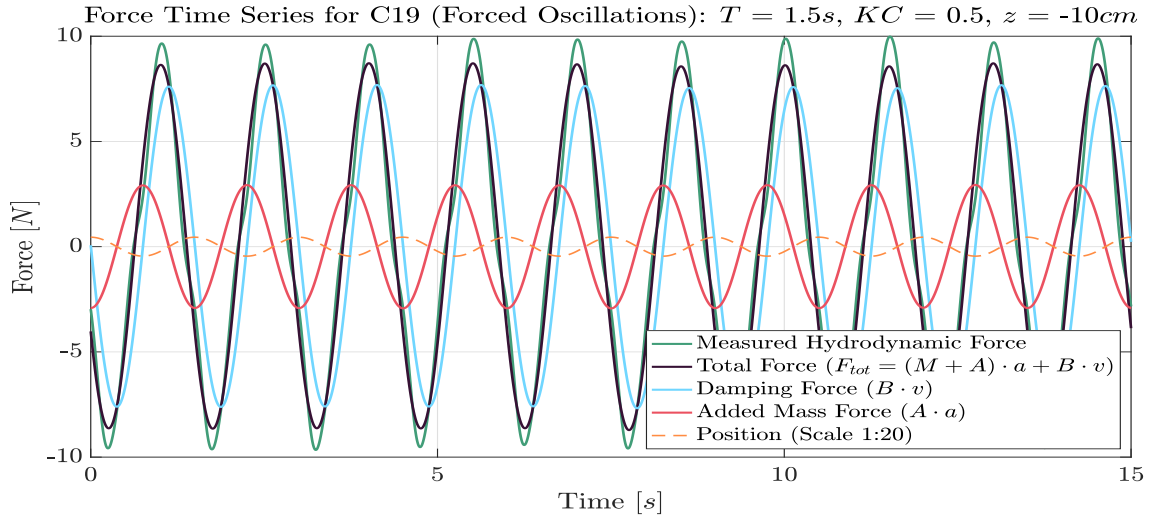


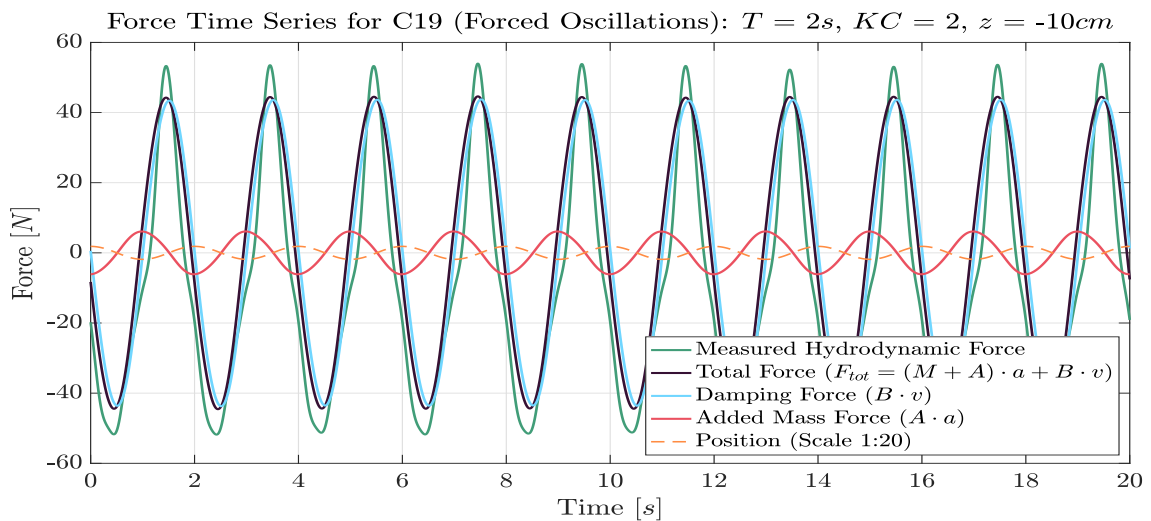
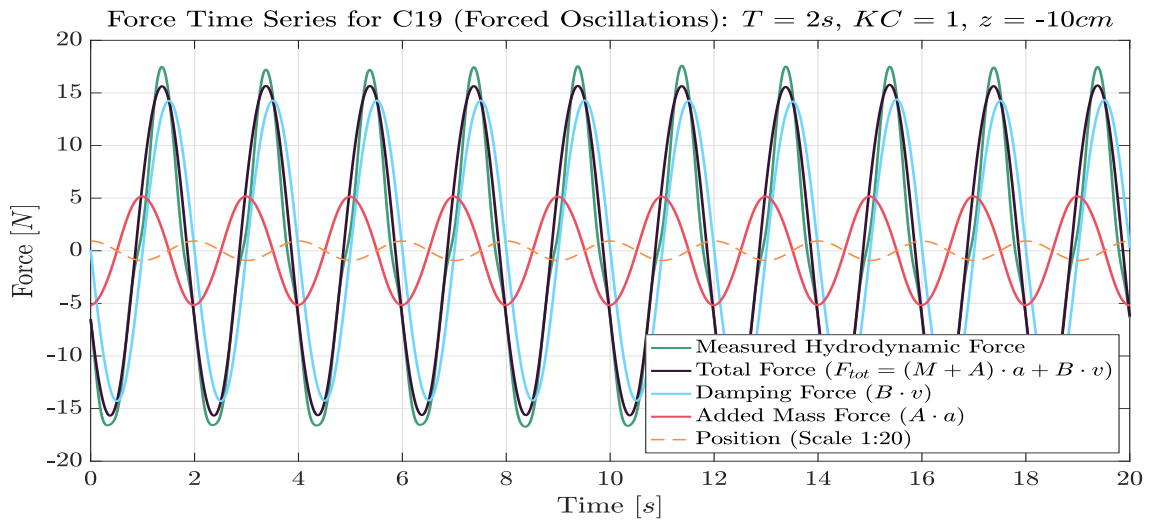
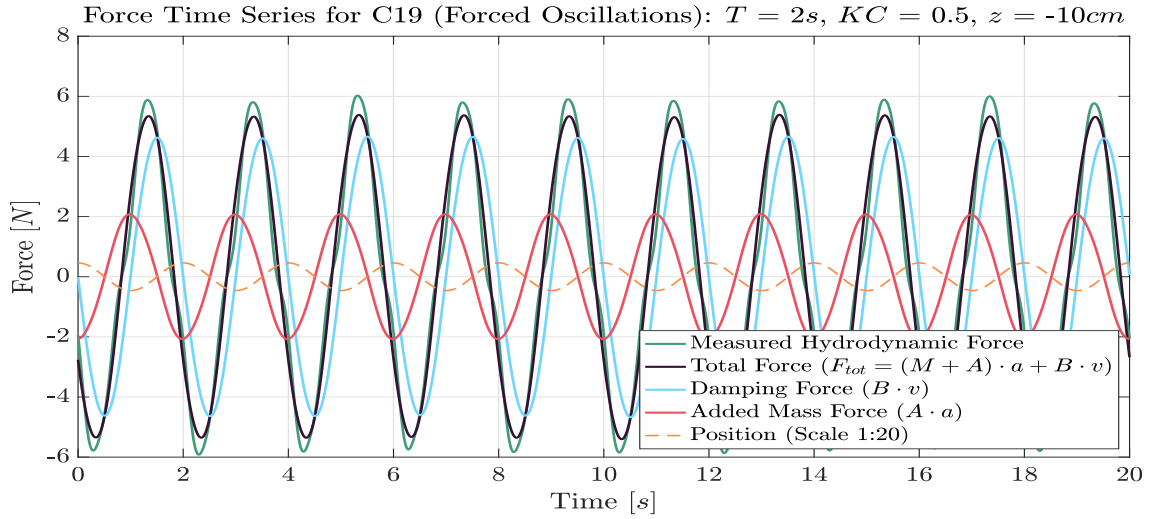
B Forced Oscillation Tests

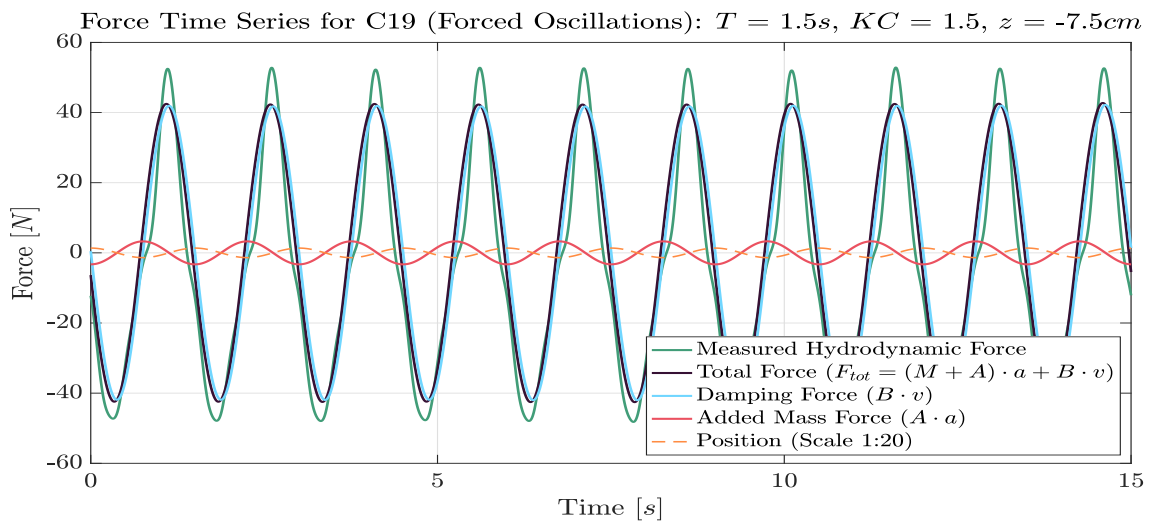
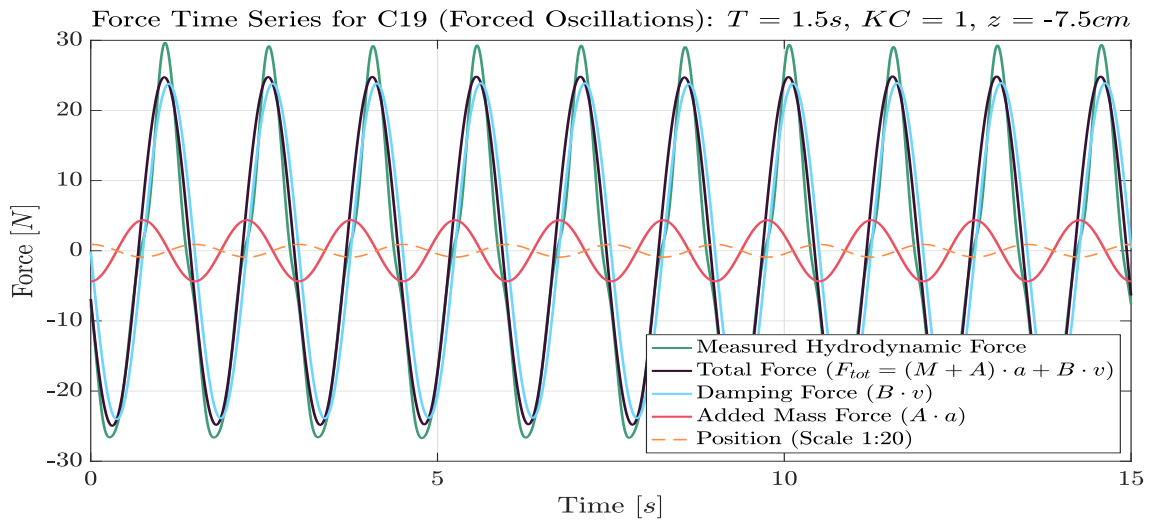
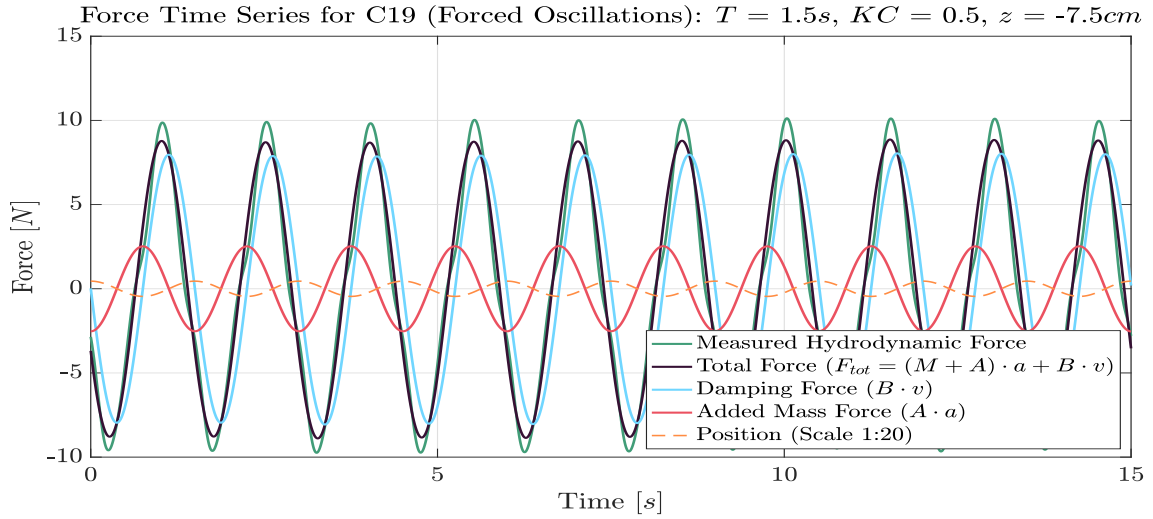
B.1 Force Time Series for C19

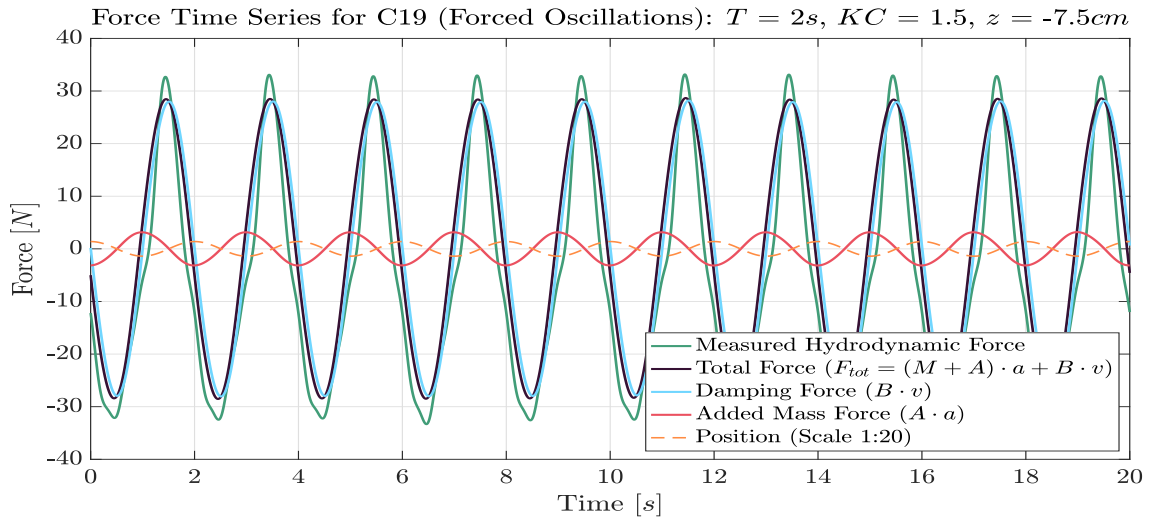
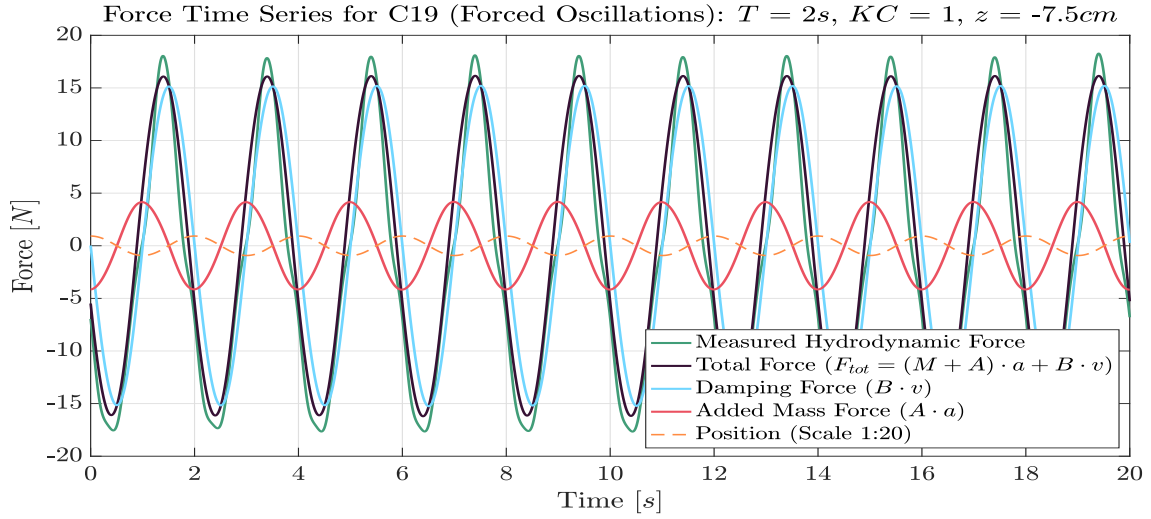
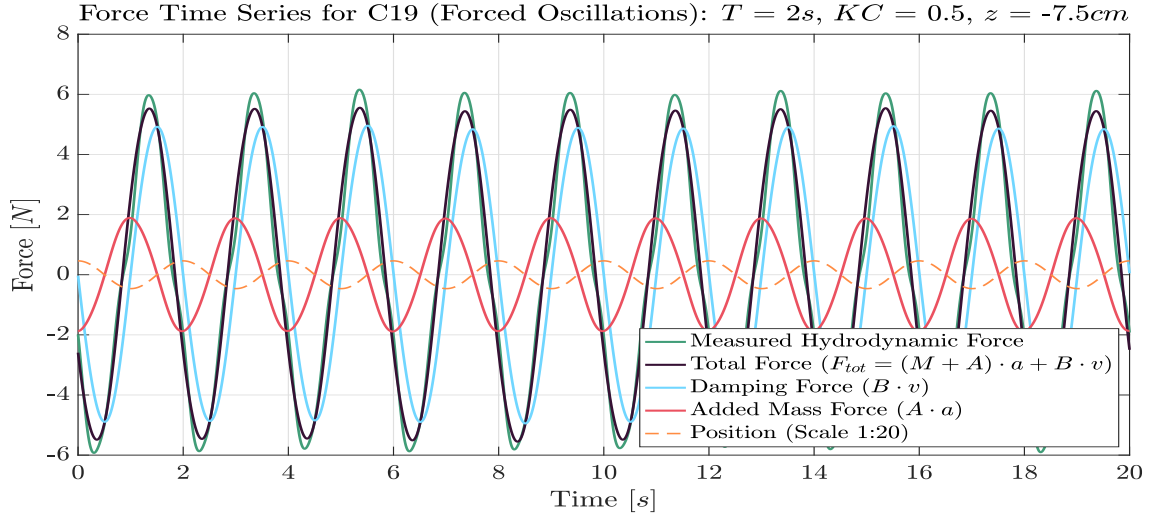


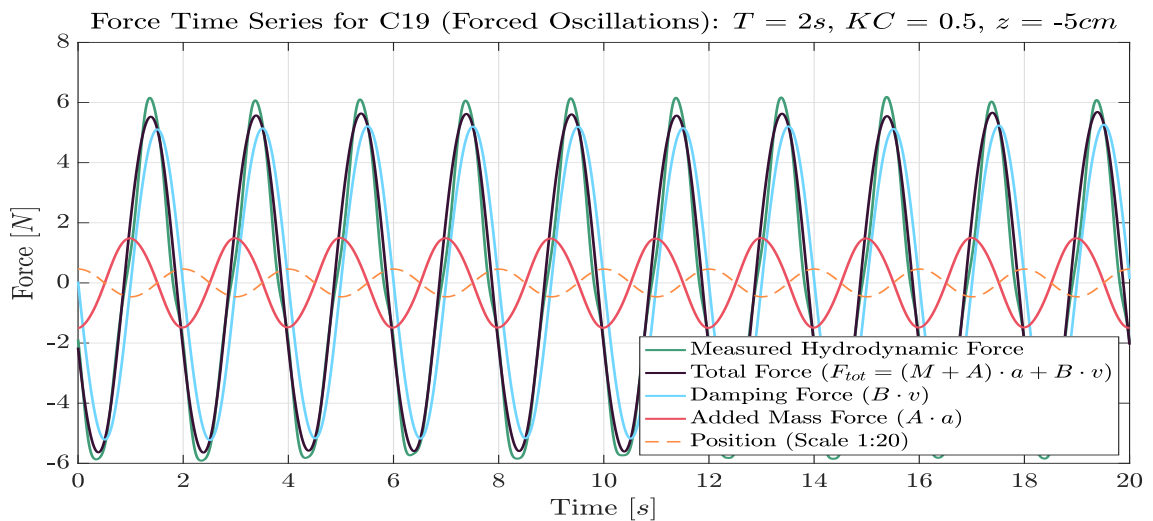
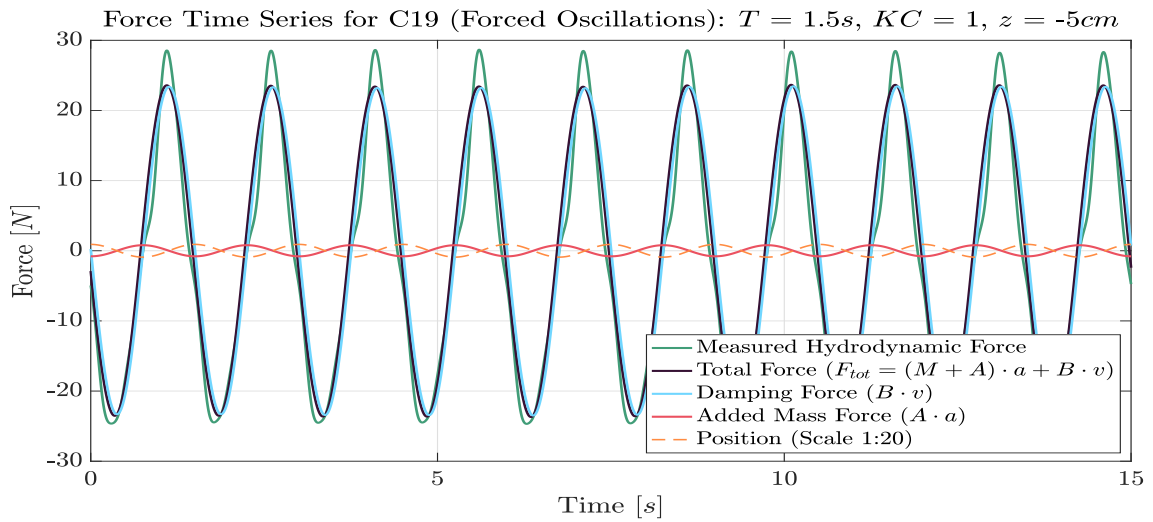
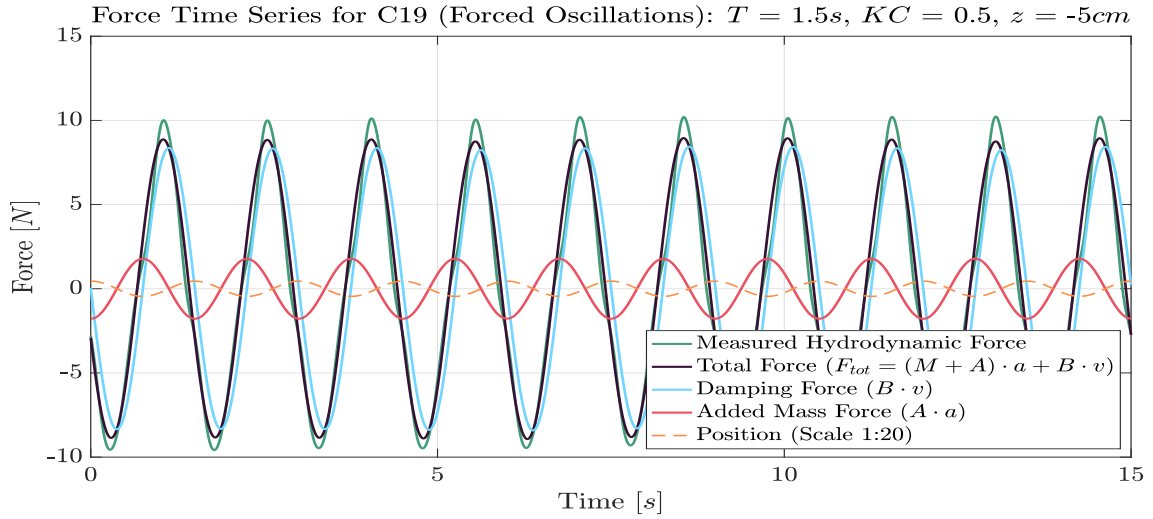


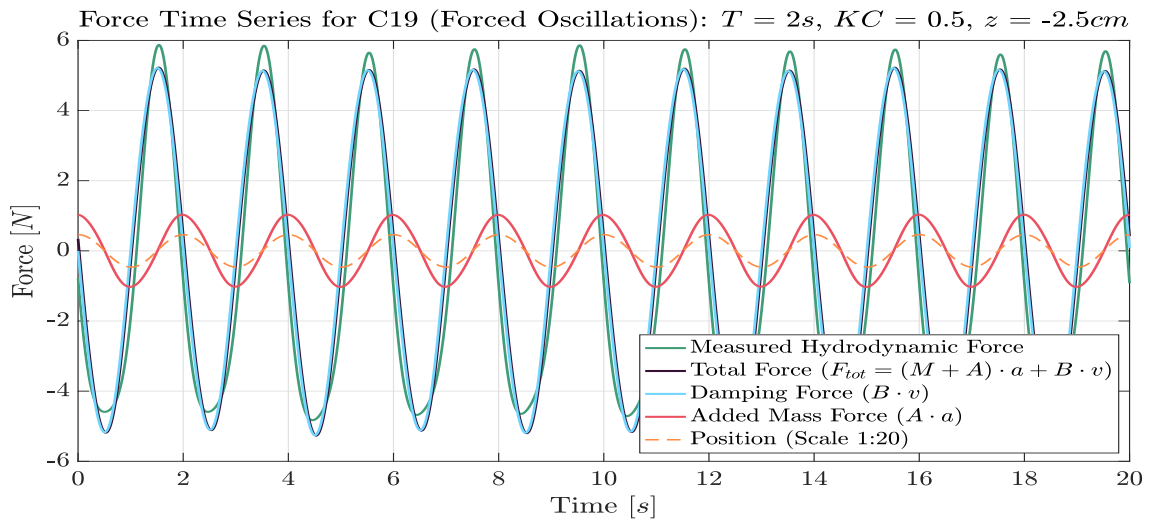
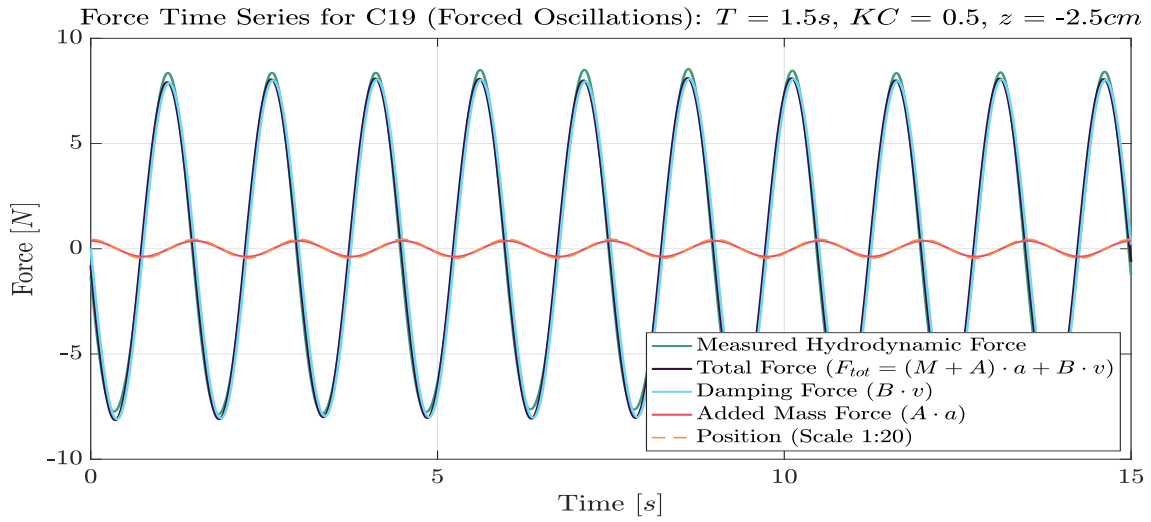
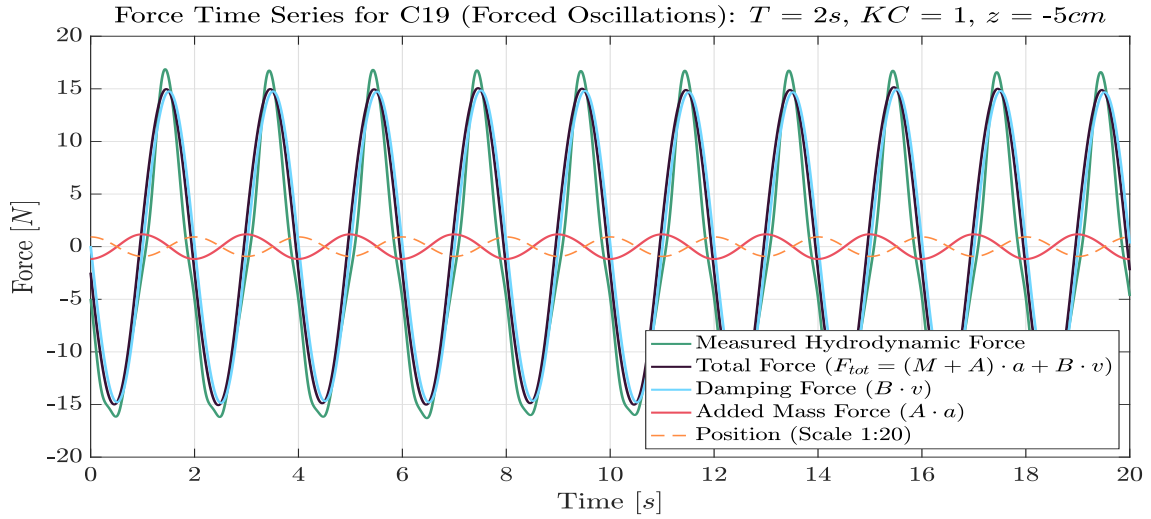




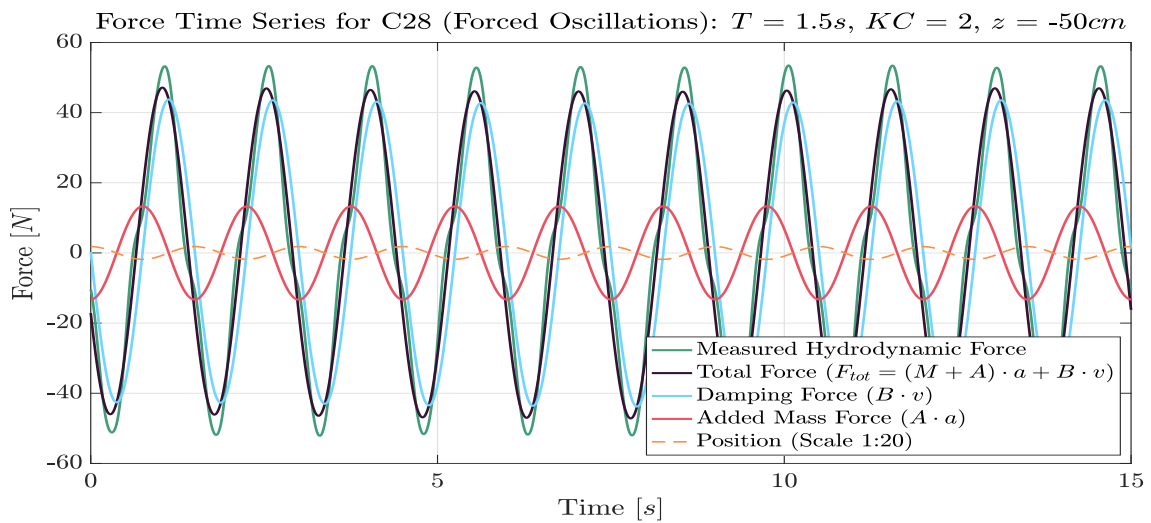
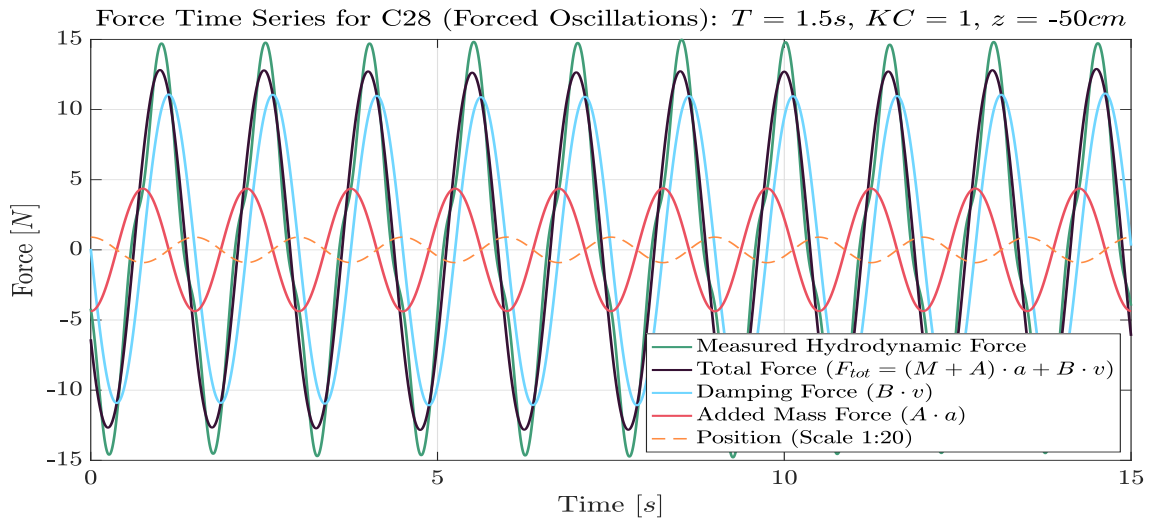
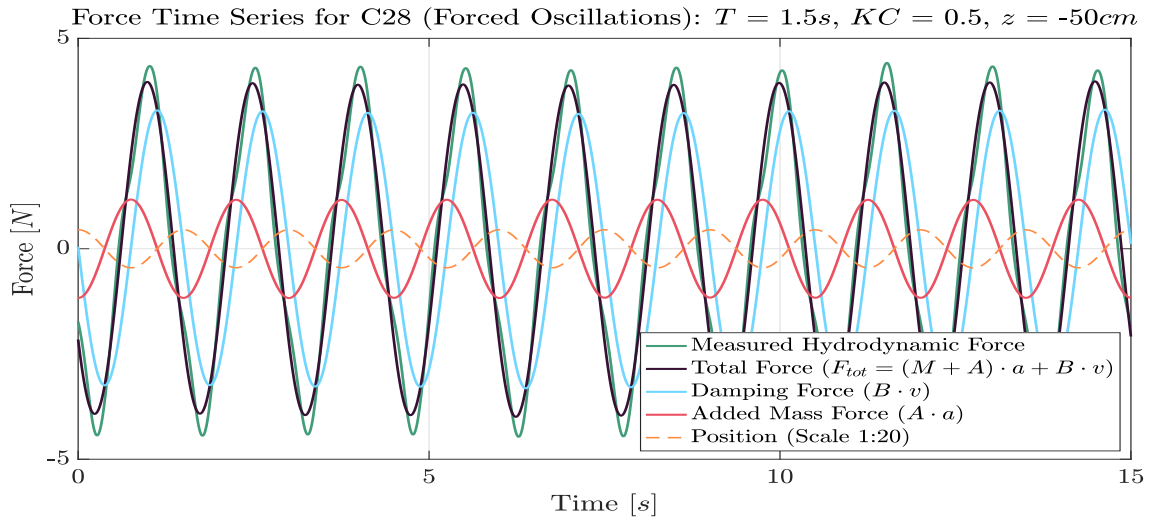


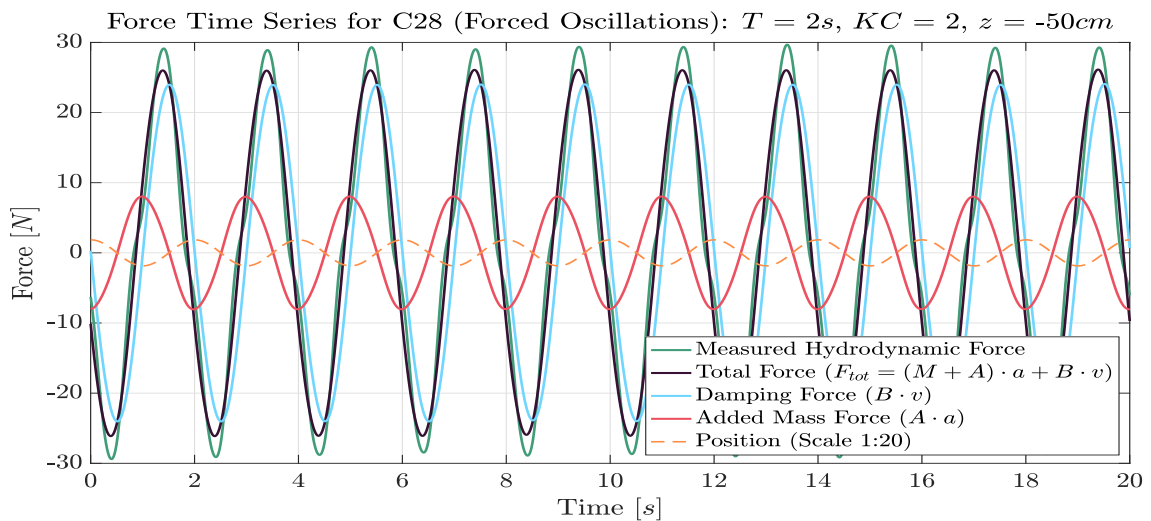
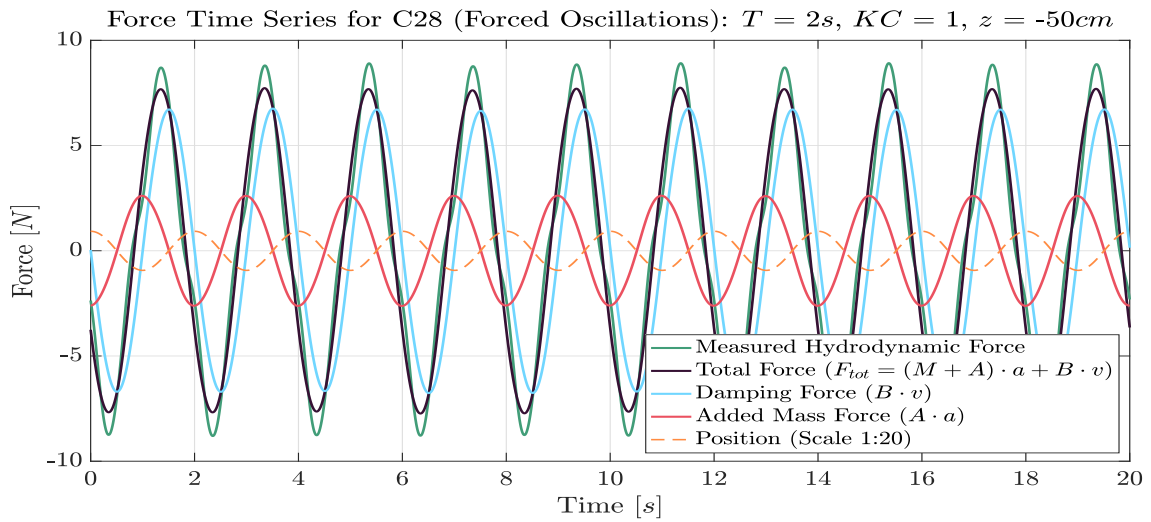
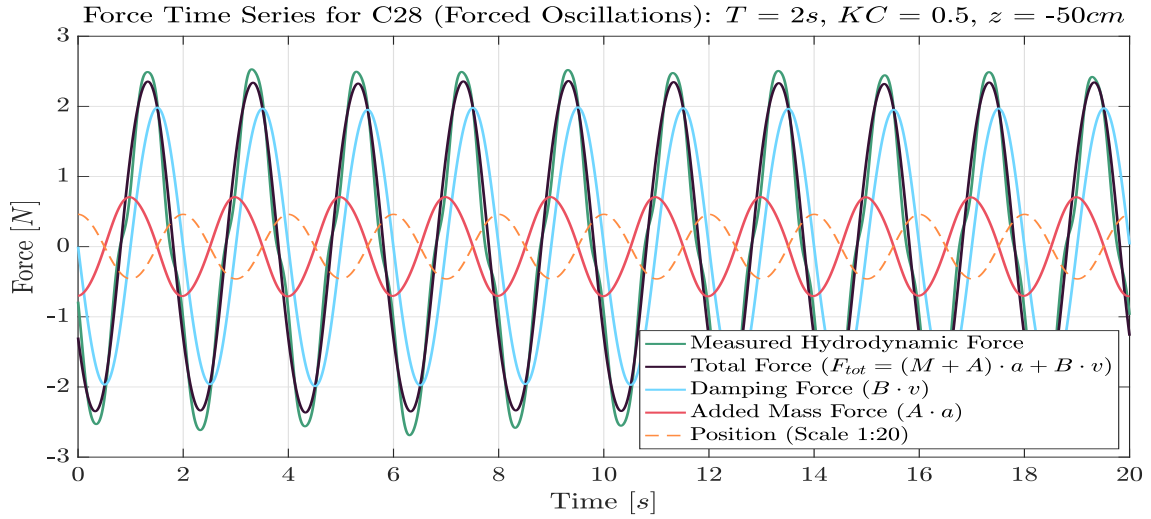


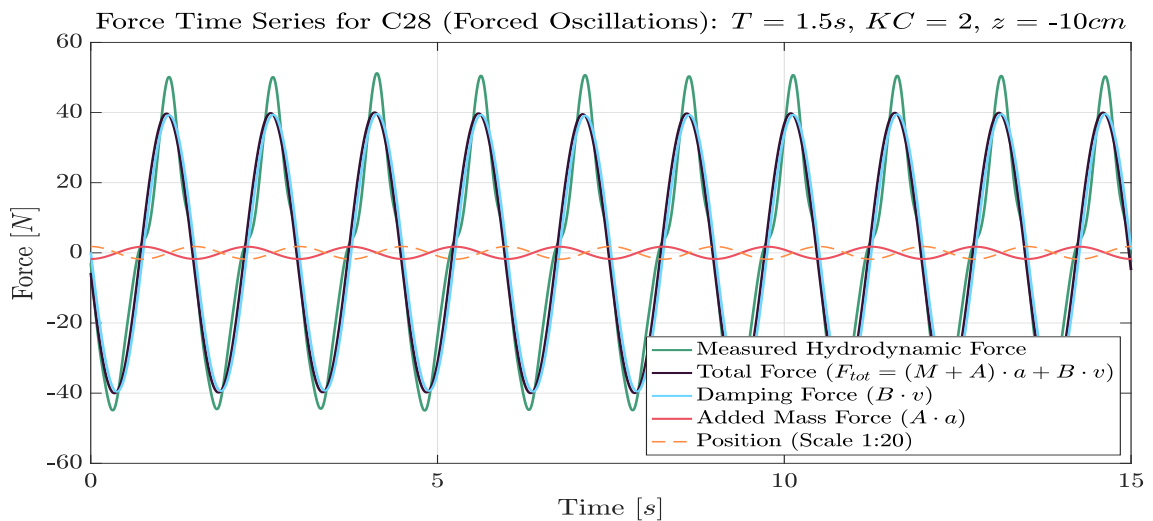
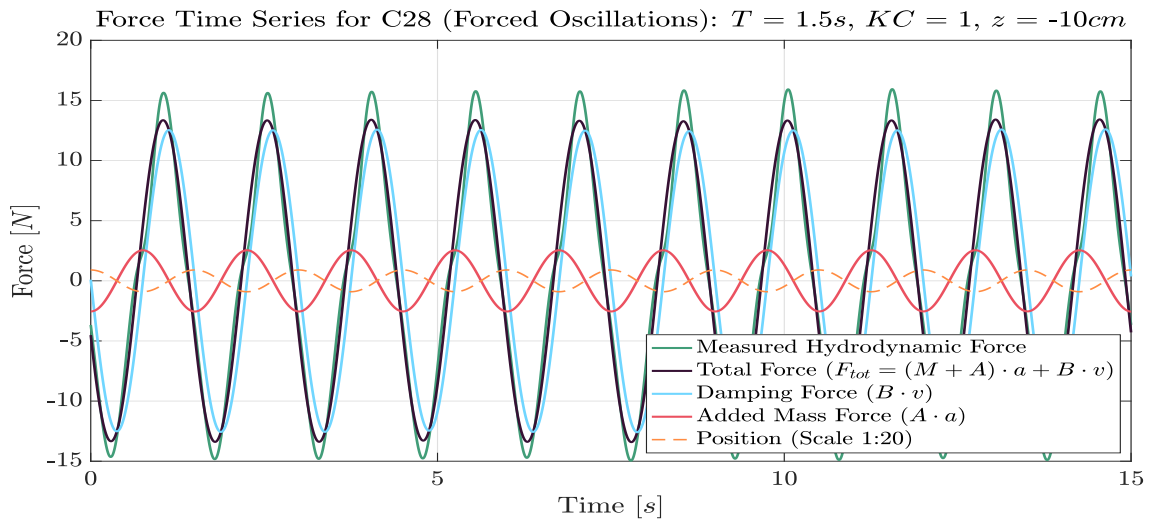
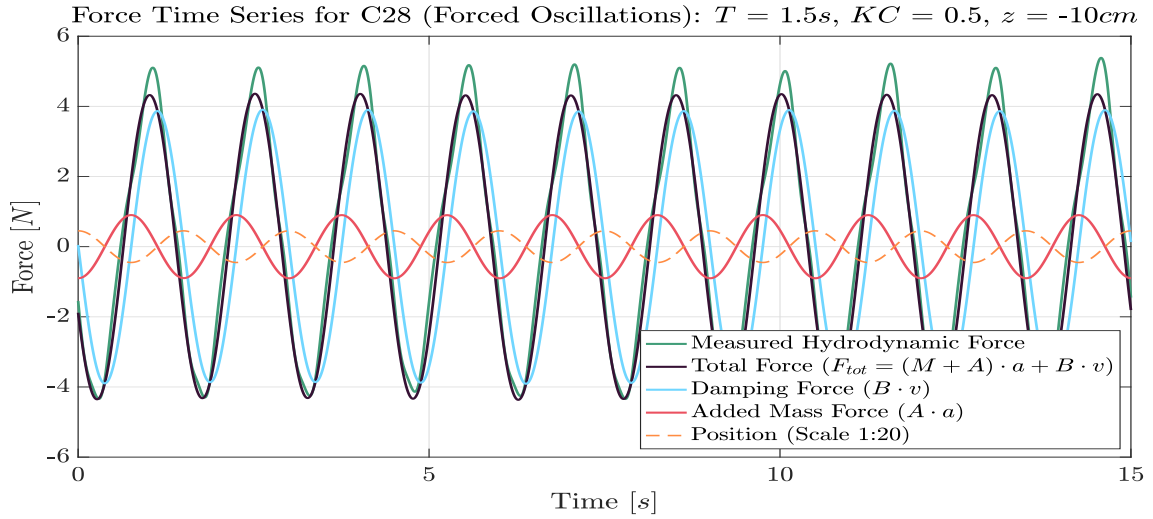


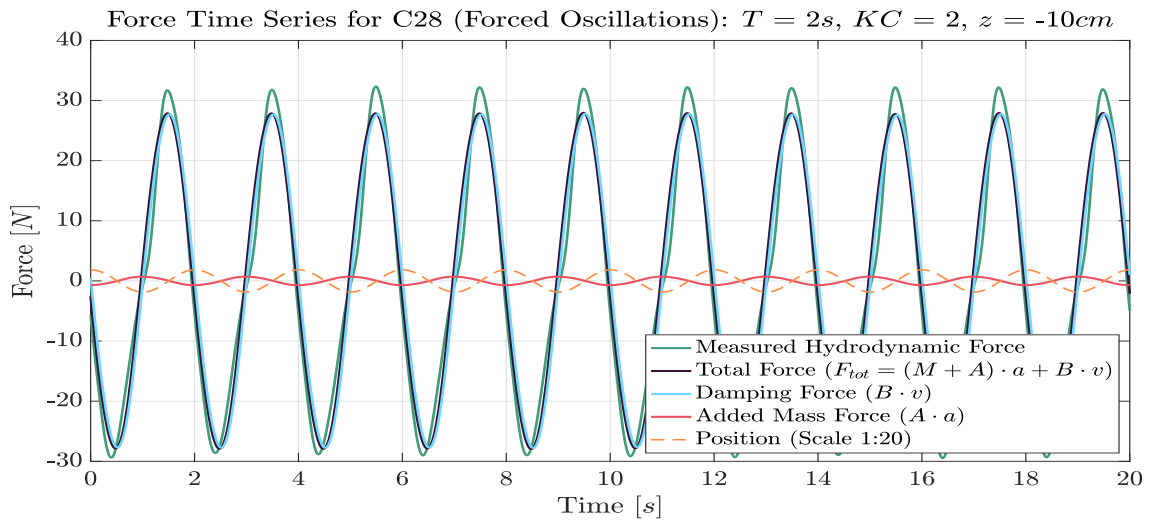
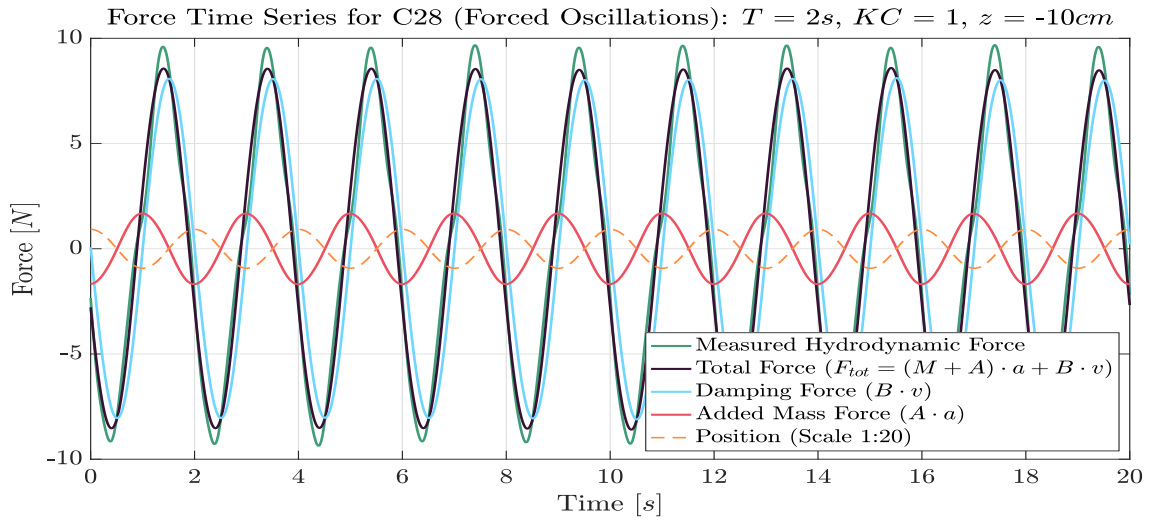
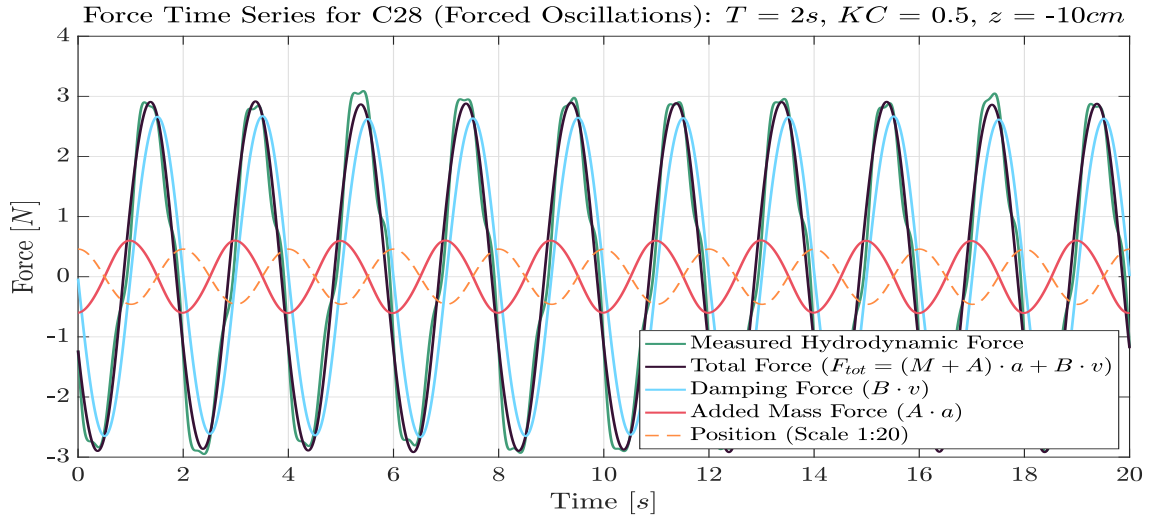


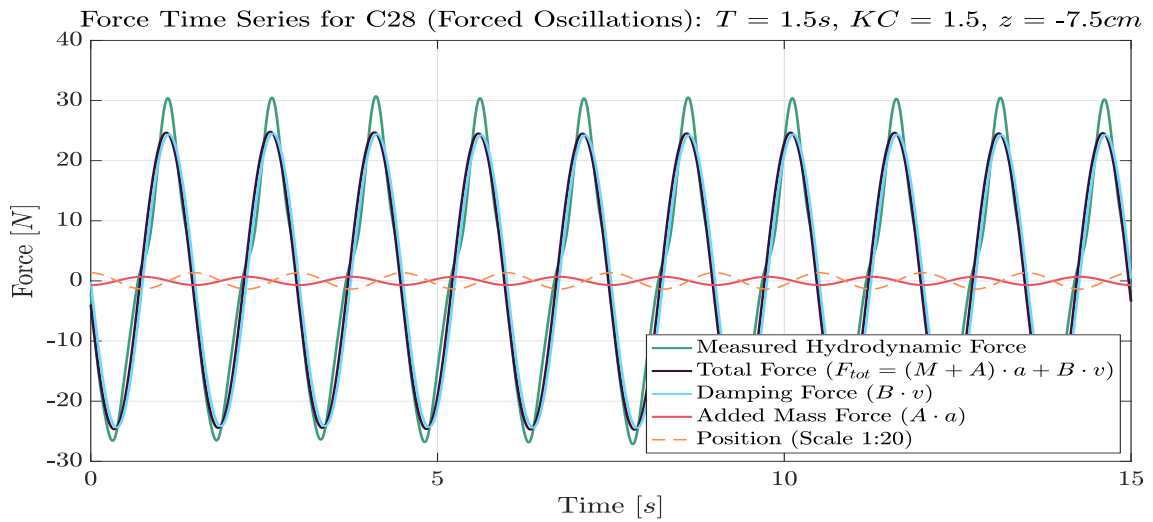
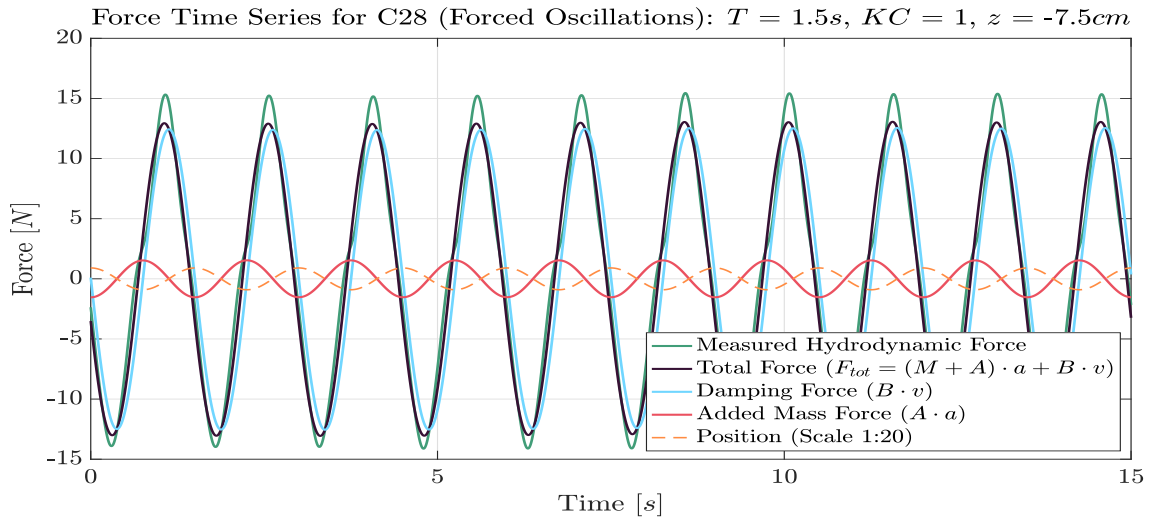
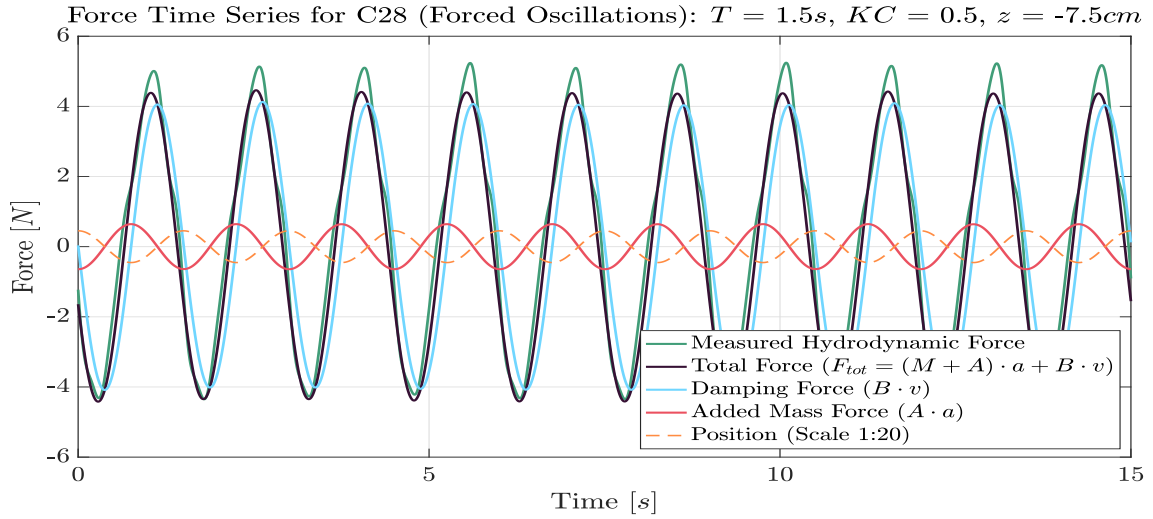
B.2 Force Time Series for C28

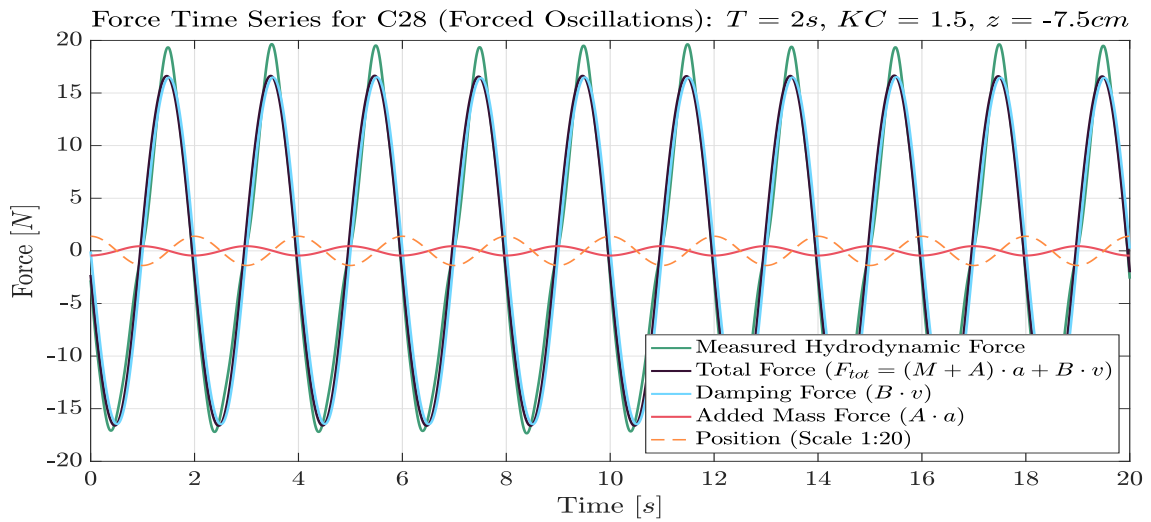
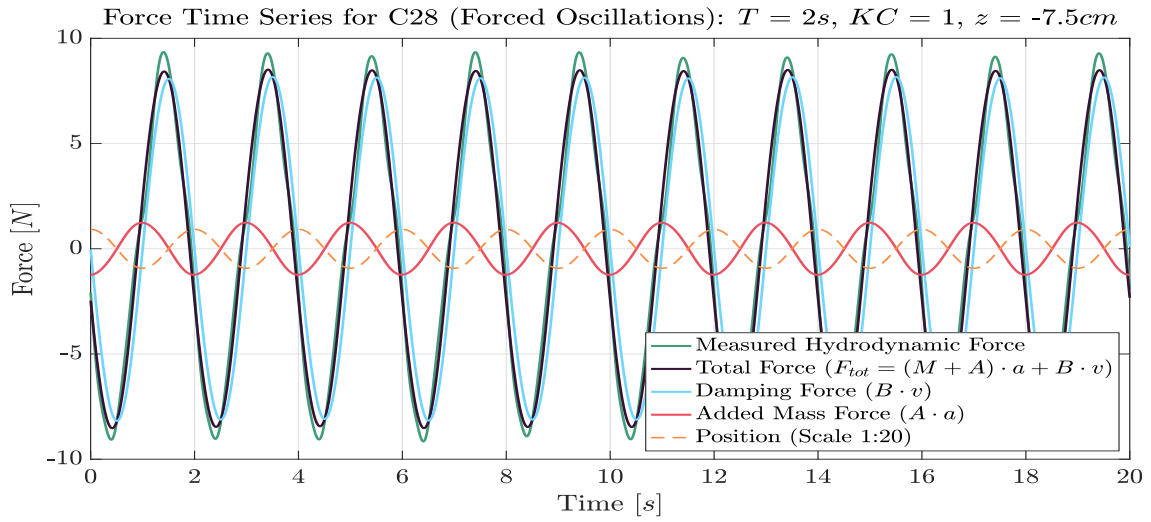
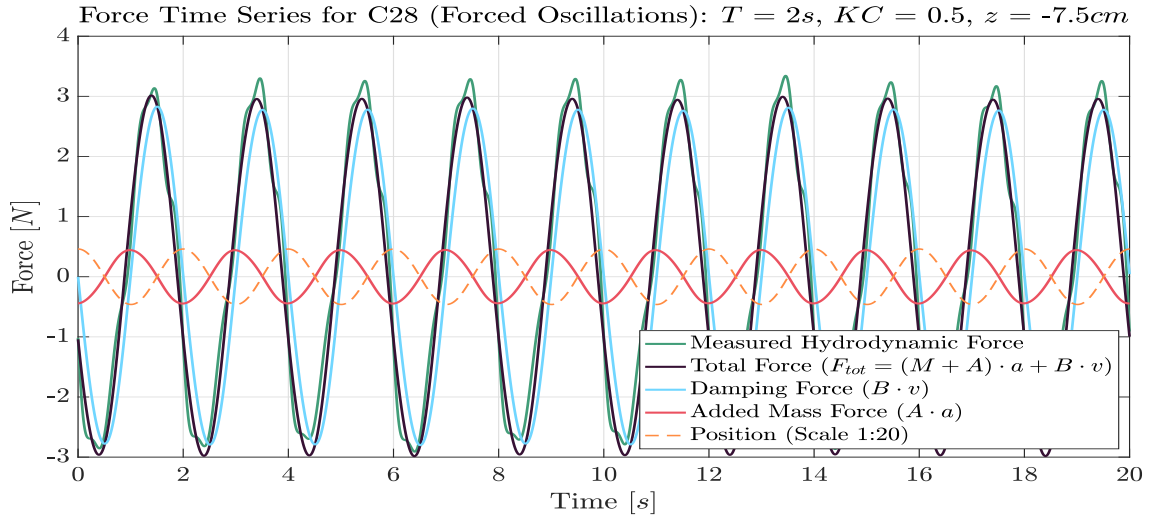


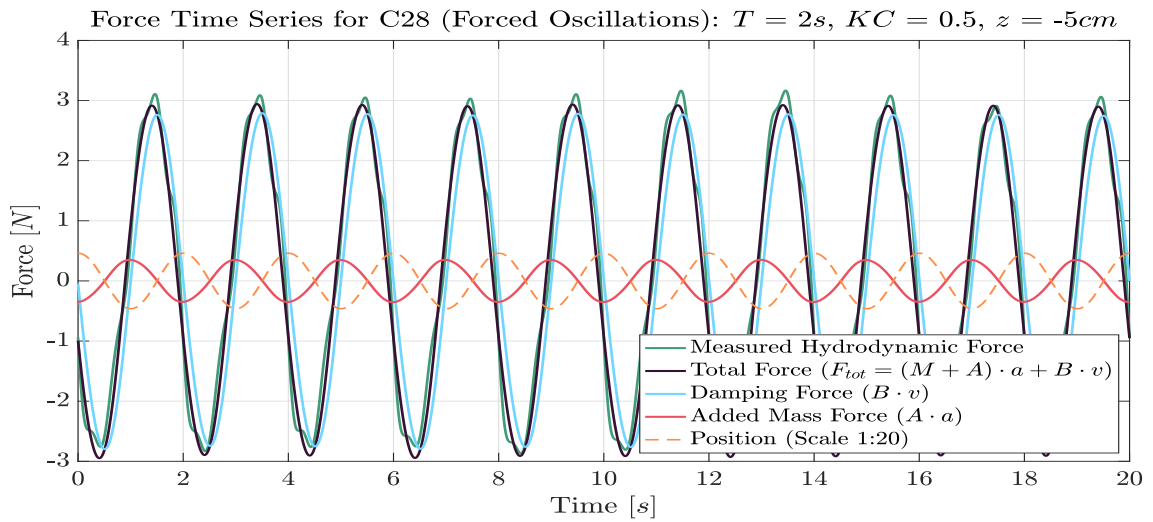
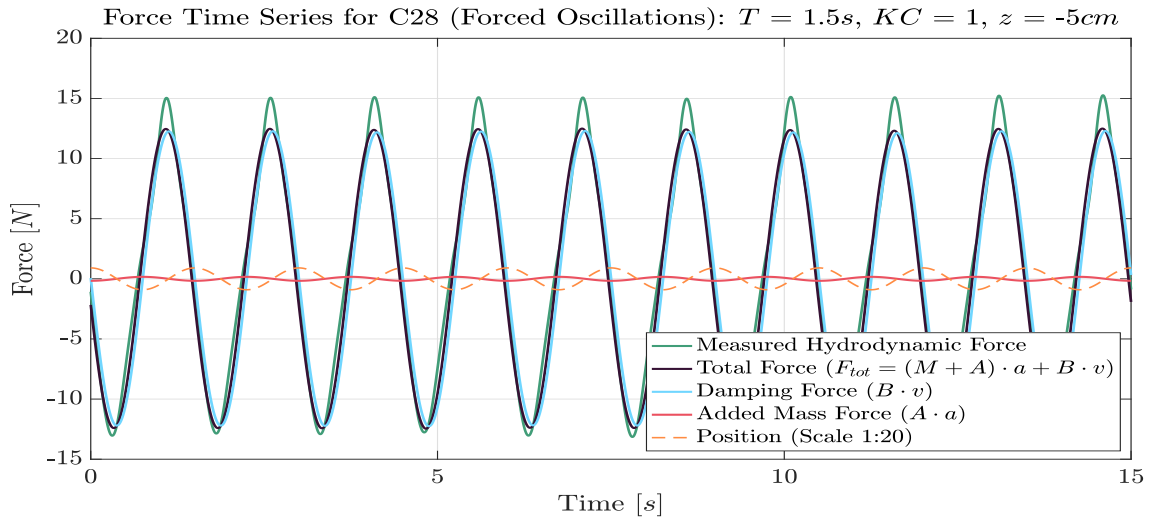
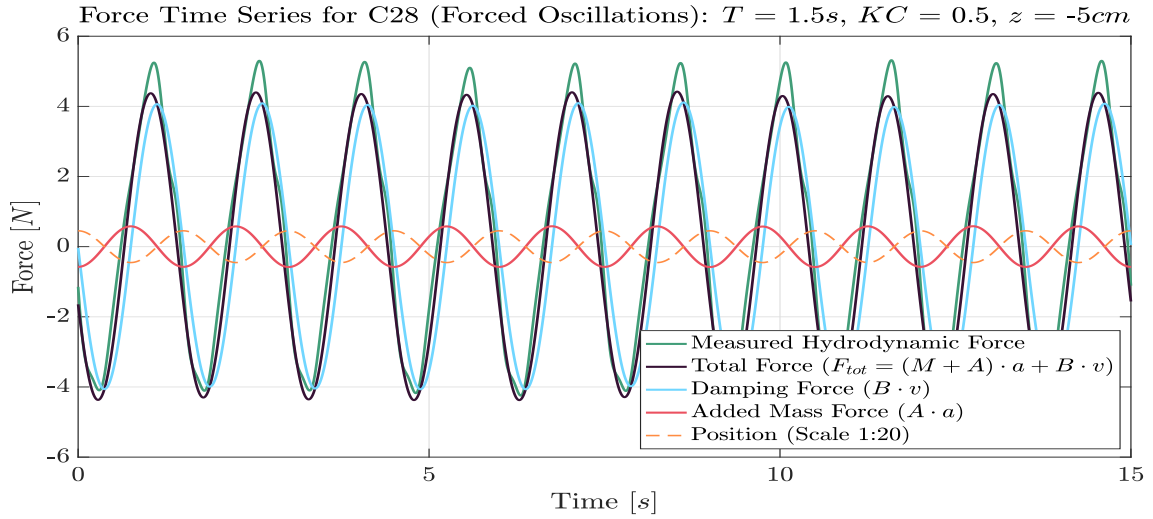


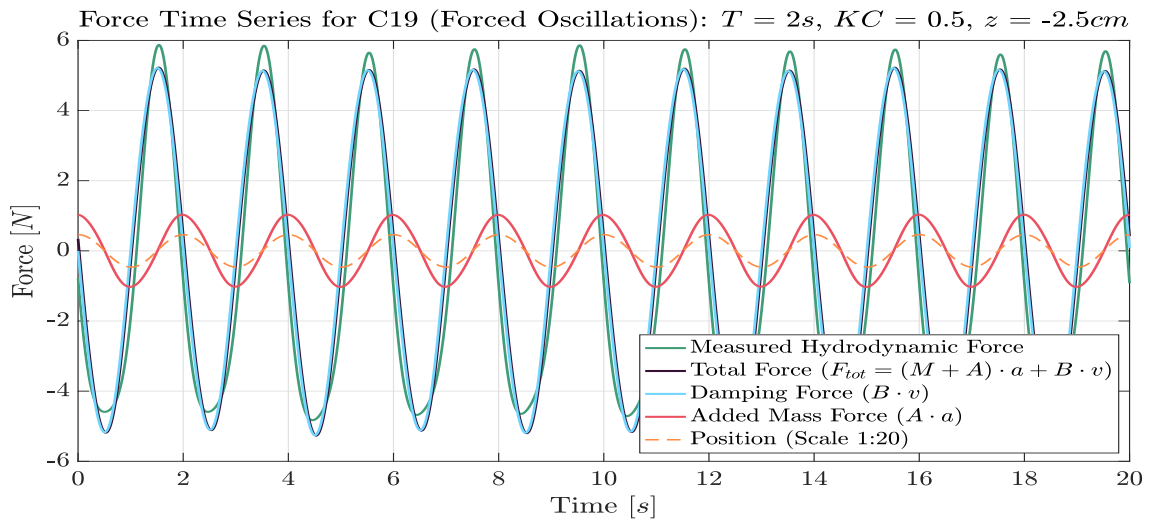
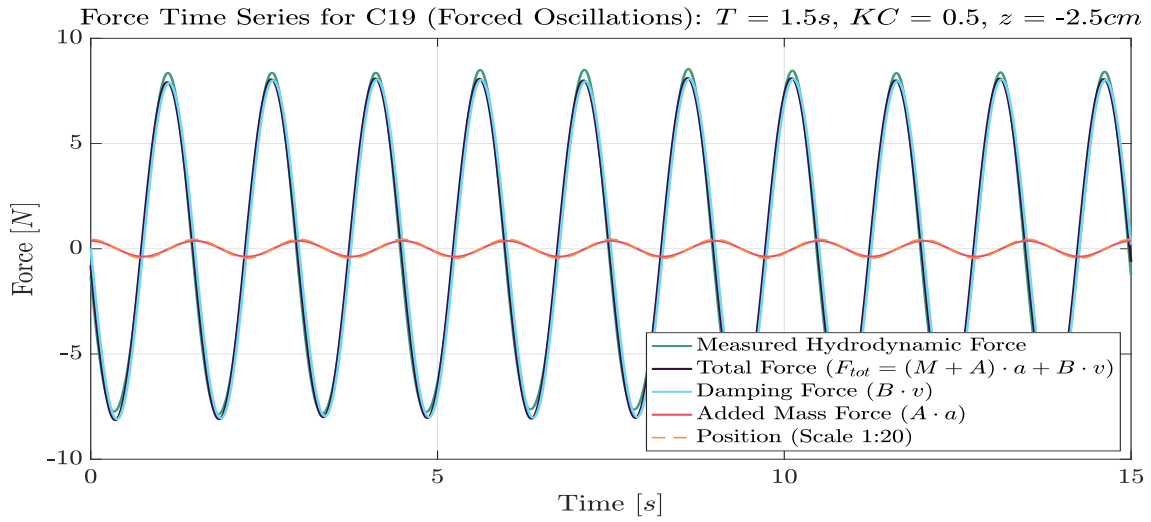
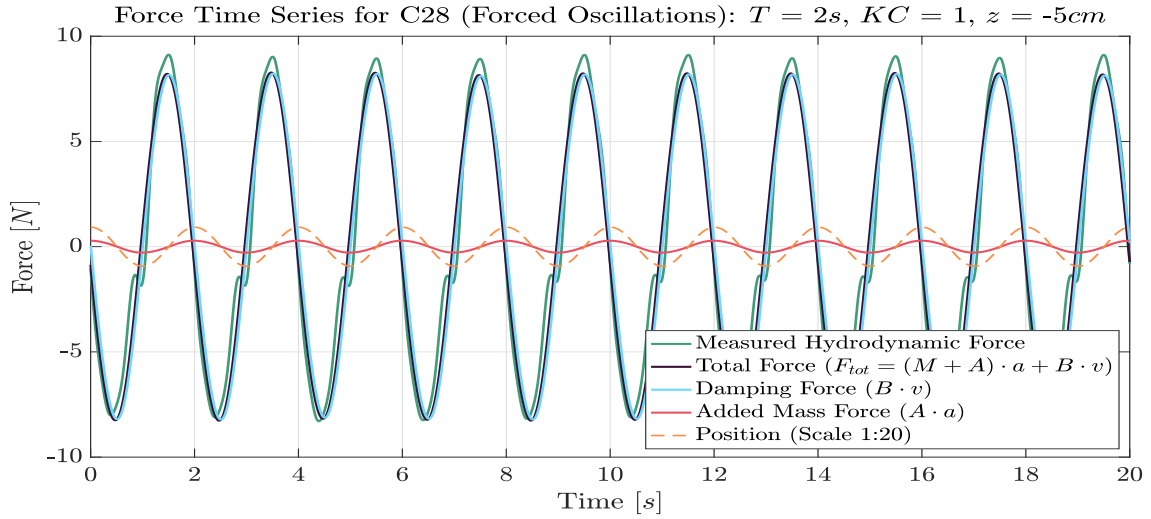






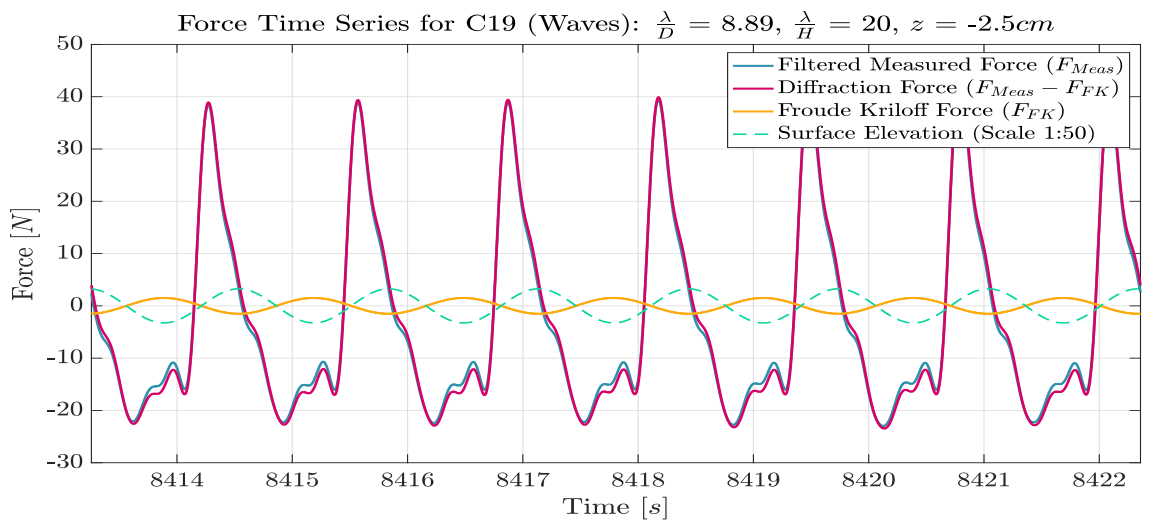
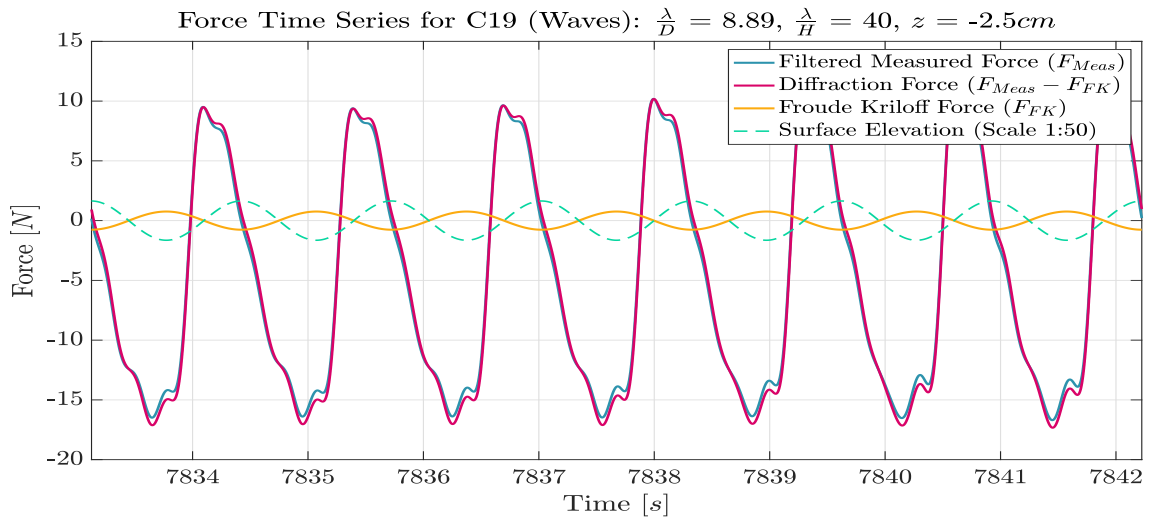
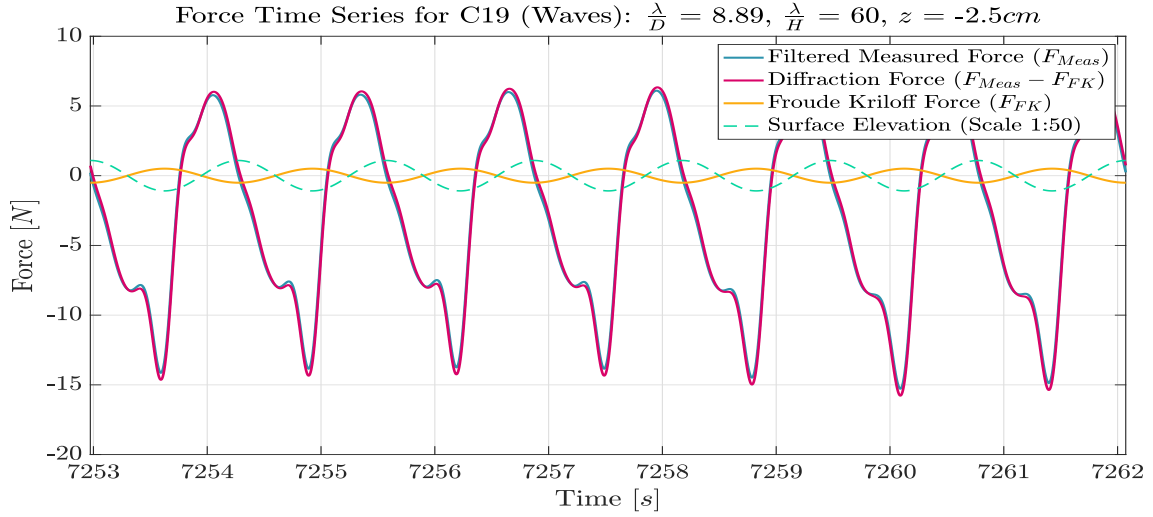


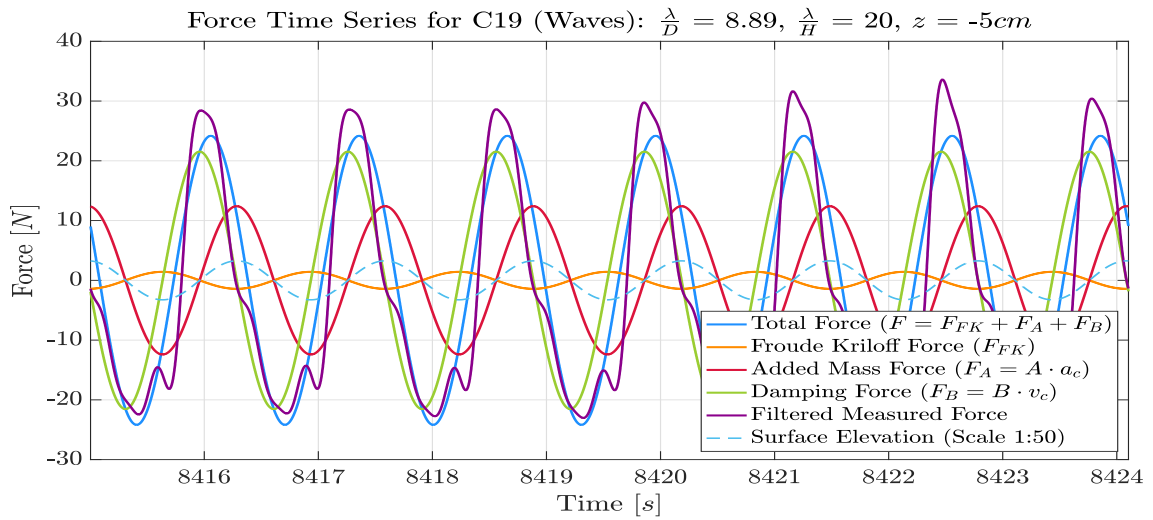
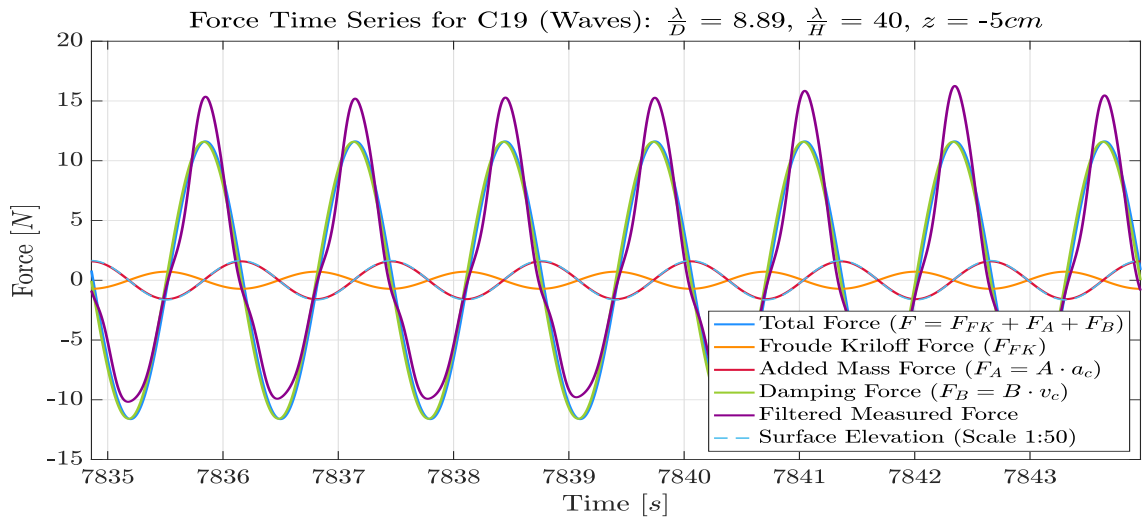
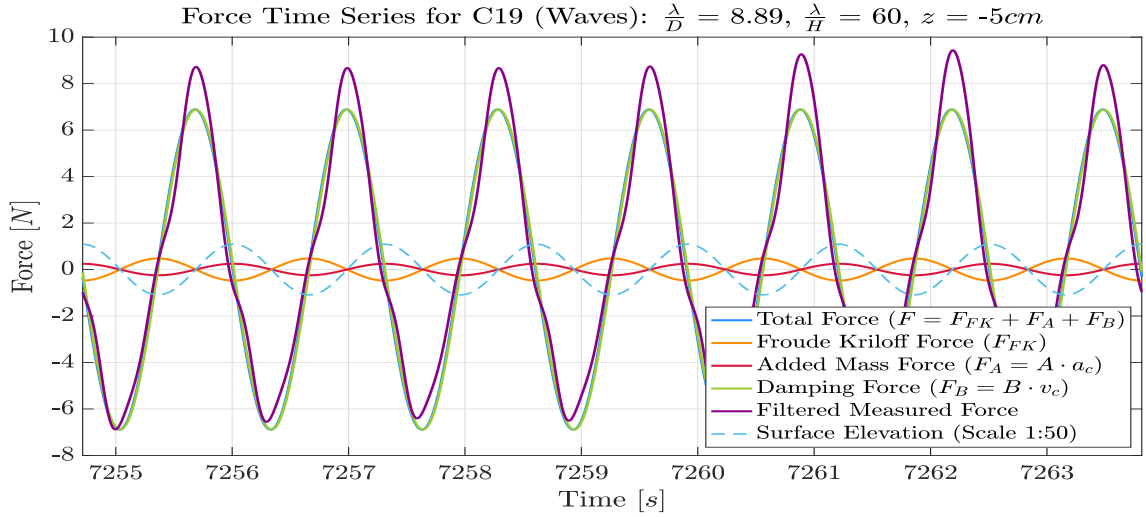


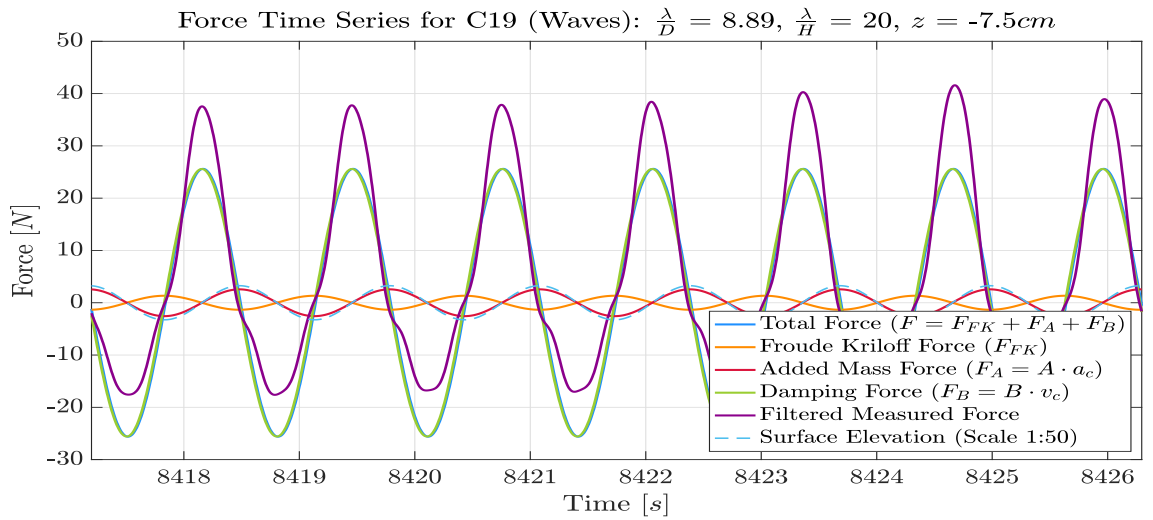
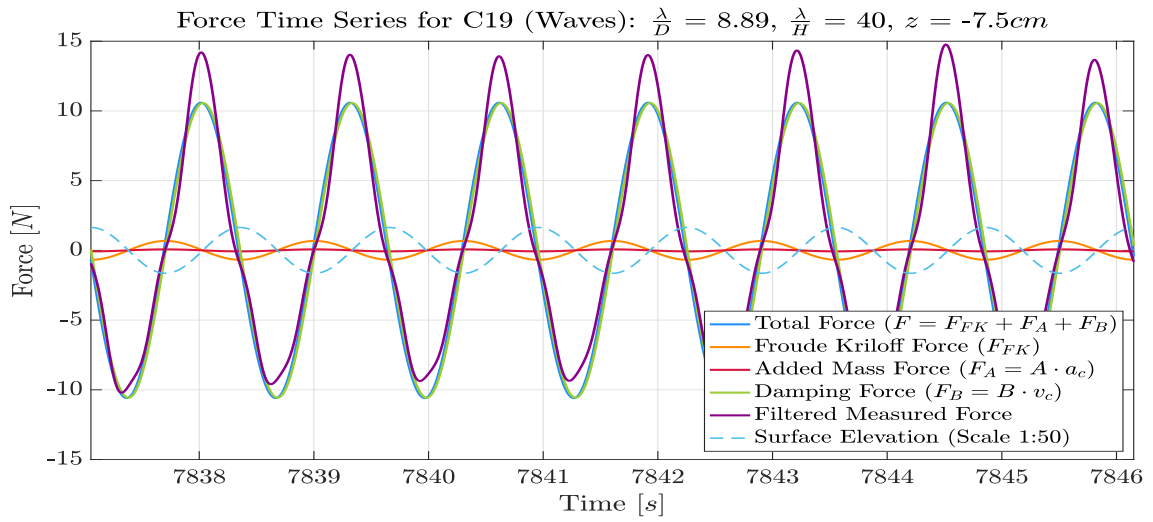
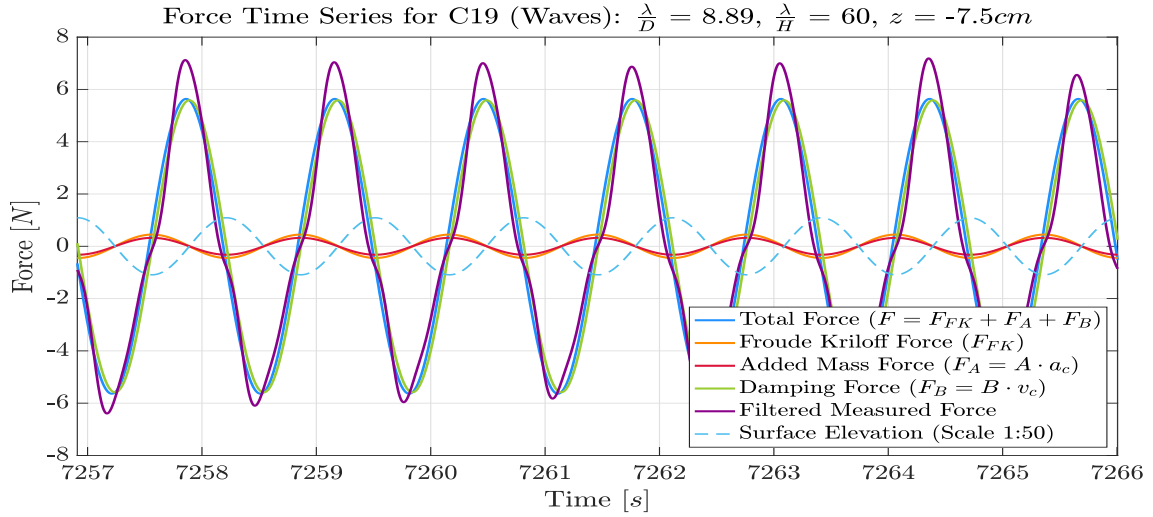


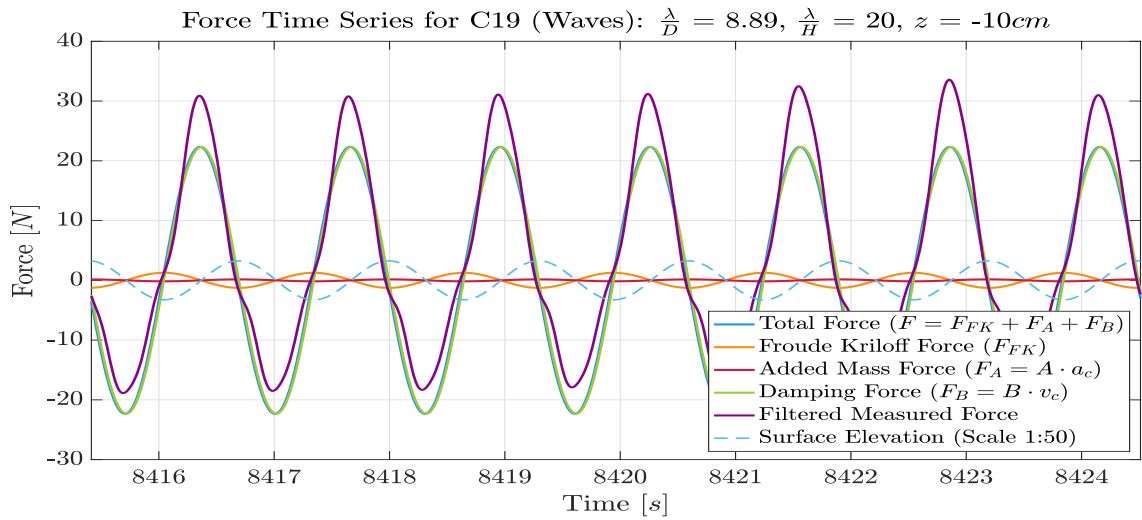
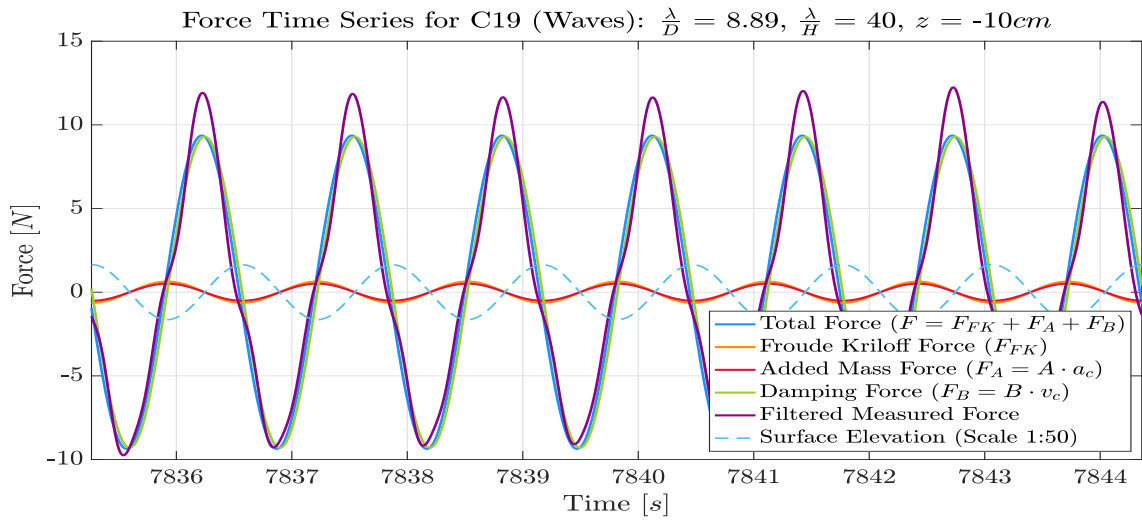
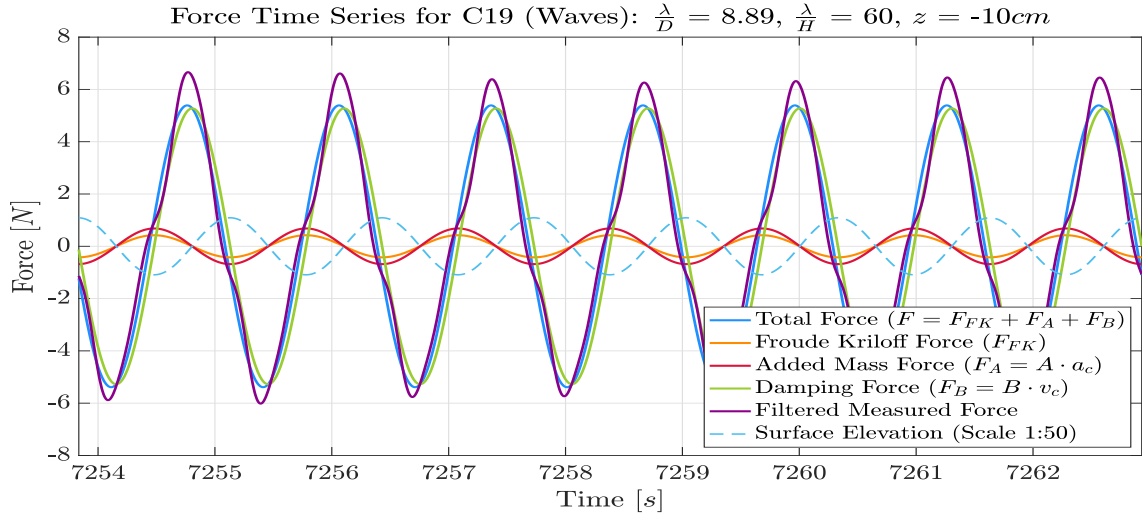
C Wave Tests

C.1 Force Time Series for C19









C.2 Force Time Series for C28

